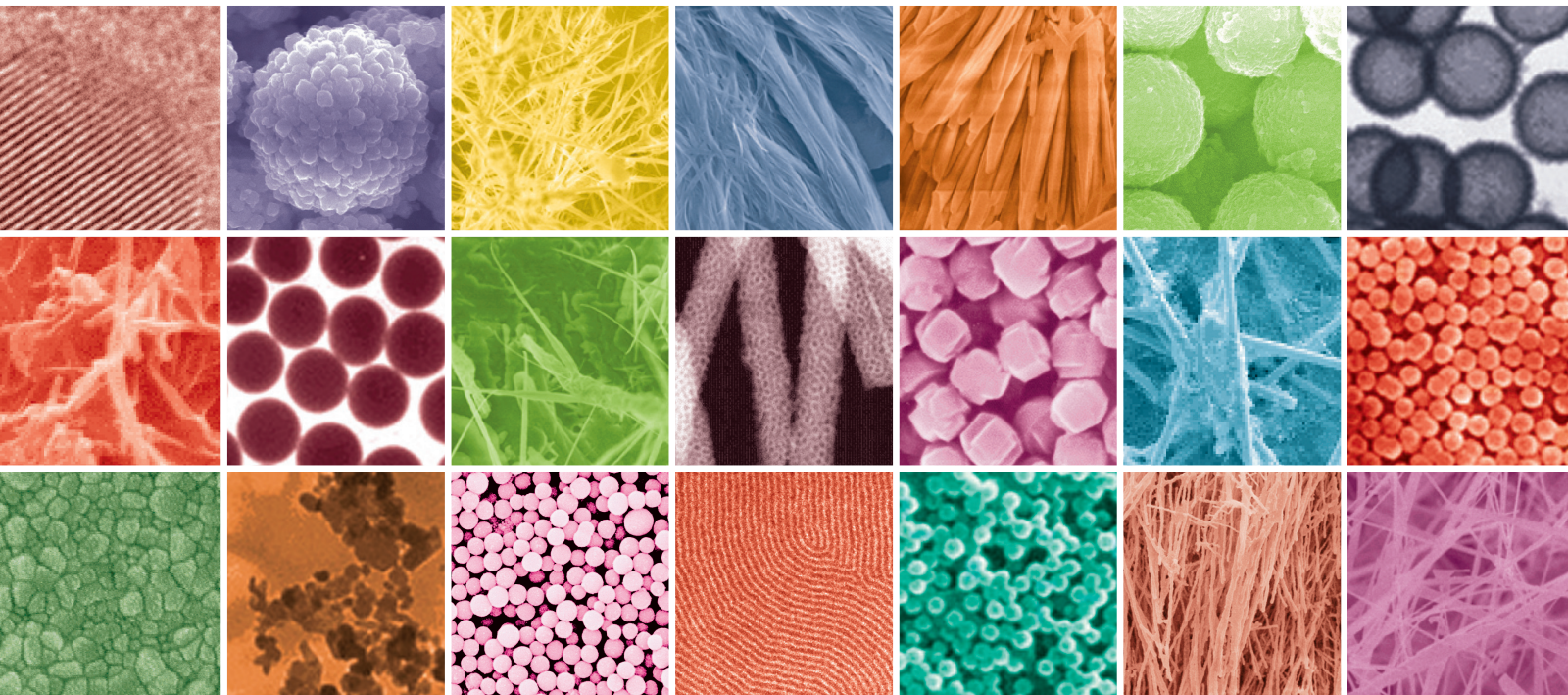


Polymer Nanocomposite Processing, Characterization and Applications 2011

Guest Editors: Gaurav Mago, Dilhan M. Kalyon, and Sadhan C. Jana





**Polymer Nanocomposite Processing,
Characterization and Applications 2011**

Journal of Nanomaterials

**Polymer Nanocomposite Processing,
Characterization and Applications 2011**

Guest Editors: Gaurav Mago, Dilhan M. Kalyon,
and Sadhan C. Jana



Copyright © 2011 Hindawi Publishing Corporation. All rights reserved.

This is a special issue published in "Journal of Nanomaterials." All articles are open access articles distributed under the Creative Commons Attribution License, which permits unrestricted use, distribution, and reproduction in any medium, provided the original work is properly cited.

Editorial Board

Katerina Aifantis, Greece
Nageh K. Allam, USA
Margarida Amaral, Portugal
Xuedong Bai, China
Enrico Bergamaschi, Italy
Theodorian Borca-Tasciuc, USA
C. Jeffrey Brinker, USA
Christian Brosseau, France
Xuebo Cao, China
Sang-Hee Cho, Republic of Korea
Shafiul Chowdhury, USA
Cui ChunXiang, China
Miguel A. Correa-Duarte, Spain
Shadi A. Dayeh, USA
Ali Eftekhari, USA
Claude Estournes, France
Alan Fuchs, USA
Lian Gao, China
Russell E. Gorga, USA
Hongchen Chen Gu, China
Mustafa O. Guler, Turkey
John Zhanhu Guo, USA
Smrati Gupta, Germany
Michael Harris, USA
Zhongkui Hong, USA
Michael Z. Hu, USA
David Hui, USA
Y.-K. Jeong, Republic of Korea
Sheng-Rui Jian, Taiwan
Wanqin Jin, China
Rakesh K. Joshi, India
Zhenhui Kang, China

Fathallah Karimzadeh, Iran
Do Kyung Kim, Republic of Korea
Kin Tak Lau, Australia
Burtrand Lee, USA
Benxia Li, China
Jun Li, Singapore
Shijun Liao, China
Gong Ru Lin, Taiwan
J.-Y. Liu, USA
Jun Liu, USA
Tianxi Liu, China
Songwei Lu, USA
Daniel Lu, China
Jue Lu, USA
Ed Ma, USA
Gaurav Mago, USA
Sanjay R. Mathur, Germany
Nobuhiro Matsushita, Japan
A. McCormick, USA
Vikas Mittal, UAE
Weihai Ni, Germany
Sherine Obare, USA
Edward Andrew Payzant, USA
Kui-Qing Peng, China
Anukorn Phuruangrat, Thailand
Ugur Serincan, Turkey
Huaiyu Shao, Japan
Donglu Shi, USA
Suprakas Sinha Ray, South Africa
Vladimir Sivakov, Germany
Marinella Striccoli, Italy
Bohua Sun, South Africa

Saikat Talapatra, USA
Nairong Tao, China
Titipun Thongtem, Thailand
Somchai Thongtem, Thailand
Valeri P. Tolstoy, Russia
Tsun-Yen Tsai, Taiwan
Takuya Tsuzuki, Australia
Raquel Verdejo, Spain
Mat U. Wahit, Malaysia
Shiren Wang, USA
Yong Wang, USA
Cheng Wang, China
Zhenbo Wang, China
Jinquan Wei, China
Ching Ping Wong, USA
Xingcai Wu, China
Guodong Xia, Hong Kong
Zhi Li Xiao, USA
Ping Xiao, UK
Shuangxi Xing, China
Yangchuan Xing, USA
N. Xu, China
Doron Yadlovker, Israel
Ying-Kui Yang, China
Khaled Youssef, USA
Kui Yu, Canada
Haibo Zeng, China
Tianyou Zhai, Japan
Renyun Zhang, Sweden
Yanbao Zhao, China
Lianxi Zheng, Singapore
Chunyi Zhi, Japan

Contents

Polymer Nanocomposite Processing, Characterization and Applications 2011, Gaurav Mago, Dilhan M. Kalyon, and Sadhan C. Jana
Volume 2011, Article ID 917474, 1 page

Preparation, Characterization, and Properties of Polyurethane-Grafted Multiwalled Carbon Nanotubes and Derived Polyurethane Nanocomposites, Tzong-Liu Wang, Chin-Chung Yu, Chien-Hsin Yang, Yeong-Tarnng Shieh, Yu-Zen Tsai, and Na-Fu Wang
Volume 2011, Article ID 814903, 9 pages

A Comparative Study of Dispersion Techniques for Nanocomposite Made with Nanoclays and an Unsaturated Polyester Resin, Farida Bensadoun, Nadir Kchit, Catherine Billotte, François Trochu, and Edu Ruiz
Volume 2011, Article ID 406087, 12 pages

Thermal Behavior with Mechanical Property of Fluorinated Silane Functionalized Superhydrophobic Pullulan/Poly(vinyl alcohol) Blends by Electrospinning Method, Mohammad Rezaul Karim and Md. Shahidul Islam
Volume 2011, Article ID 979458, 7 pages

New Resistive Switching and Self-Regulating Heating in Foliated Graphite/Nickel Polyvinyl Chloride Nanocomposites, Omar A. Al-Hartomy, Falleh Al-Salamy, A. A. Al-Ghamdi, Attieh A. Al-Ghamdi, A. M. Abdel Daiem, and Farid El-Tantawy
Volume 2011, Article ID 694879, 10 pages

Influence of Silanization Treatment on Thermomechanical Properties of Multiwalled Carbon Nanotubes: Poly(methylmethacrylate) Nanocomposites, Carlos Velasco-Santos, Ana Laura Martinez-Hernandez, Witold Brostow, and Victor M. Castaño
Volume 2011, Article ID 928659, 9 pages

Nanofibrous Resonant Membrane for Acoustic Applications, K. Kalinová
Volume 2011, Article ID 265720, 6 pages

Electrical Properties of Zn-Phthalocyanine and Poly (3-hexylthiophene) Doped Nematic Liquid Crystal, Y. Karakuş, M. Okutan, A. Kösemen, S. E. San, Z. Alpaslan, and A. Demir
Volume 2011, Article ID 729085, 5 pages

Editorial

Polymer Nanocomposite Processing, Characterization and Applications 2011

Gaurav Mago,¹ Dilhan M. Kalyon,² and Sadhan C. Jana³

¹ Department of Mechanical Engineering, Stevens Institute of Technology, Hoboken, NJ 07030, USA

² Highly Filled Materials Institute and Department of Chemical Engineering and Materials Science, Stevens Institute of Technology, Hoboken, NJ 07030, USA

³ Department of Polymer Engineering, The University of Akron, 250 South Forge Street, Akron, OH 44325, USA

Correspondence should be addressed to Gaurav Mago, gauravmago2001@gmail.com

Received 14 December 2011; Accepted 14 December 2011

Copyright © 2011 Gaurav Mago et al. This is an open access article distributed under the Creative Commons Attribution License, which permits unrestricted use, distribution, and reproduction in any medium, provided the original work is properly cited.

There is a growing interest in the incorporation of nanoparticles into polymers to improve various functional properties (such as mechanical, thermal, optical, magnetic, and electrical properties). However, the ultimate properties of nanocomposites are affected by a large number of factors including the microstructural distributions that are generated during nanocomposite processing. While significant work has been done on preparation and properties of polymer nanocomposites, the interrelationship between processing, morphology, and functional properties of nanocomposites is complex and needs further elucidation. Furthermore, the effective utilization of nanoparticles in polymers depends strongly on the ability to disperse the nanoparticles uniformly throughout the polymeric matrices especially without reducing their aspect ratios. An understanding of the relationship between processing, morphology, and functional properties of nanocomposites will be very helpful in optimizing the overall properties of nanocomposites as well as improving the models for predicting the properties of nanocomposite systems. Such knowledge will facilitate the generation and optimization of polymeric nanocomposites with better tailored ultimate properties.

Considering the challenges in the area of development of adequate methods of processing for nanocomposites, we invited research articles to this special issue with a special focus on the interrelationships between polymer nanocomposite processing, characterization, and novel applications. This special issue with a total of seven papers covers a wide range of areas related to covalent functionalization of carbon nanotubes (CNTs) with polyurethane segments to improve

the dispersion and mechanical properties; silanization of CNTs to improve interaction at the interface to allow better load transfer between matrix and nanoparticles; rheological characterization of nanoclay dispersions in nanocomposites prepared via different processing methods such as sonication, manual mixing, or high shear mixing; electrospinning to produce nanofibrous resonant membranes for acoustic applications; superhydrophobic membranes prepared via electrospinning from fluorinated silane-functionalized pullulan/poly(vinyl alcohol) blends; electrical properties of doped nematic liquid crystals; and finally, the preparation of polymer nanocomposites with graphite and nickel nanoparticles for potential applications in positive temperature coefficient of resistance devices, self-regulating heater, and temperature sensors.

It is hoped that this special issue will help readers with a wide range of backgrounds to understand the impact of various processing methods as well as nanoparticles on the nanocomposite properties and applications.

Acknowledgments

The editors would like to acknowledge the invited and contributing authors, reviewers, and staff members of Hindawi Publisher.

Gaurav Mago
Dilhan M. Kalyon
Sadhan C. Jana

Research Article

Preparation, Characterization, and Properties of Polyurethane-Grafted Multiwalled Carbon Nanotubes and Derived Polyurethane Nanocomposites

Tzong-Liu Wang,¹ Chin-Chung Yu,² Chien-Hsin Yang,¹ Yeong-Tarng Shieh,¹ Yu-Zen Tsai,³ and Na-Fu Wang³

¹Department of Chemical and Materials Engineering, National University of Kaohsiung, Kaohsiung 811, Taiwan

²Department of Applied Physics, National University of Kaohsiung, Kaohsiung 811, Taiwan

³Department of Electronics, Cheng Shiu University, Kaohsiung County 833, Taiwan

Correspondence should be addressed to Tzong-Liu Wang, tlwang@nuk.edu.tw

Received 15 July 2011; Accepted 3 October 2011

Academic Editor: Gaurav Mago

Copyright © 2011 Tzong-Liu Wang et al. This is an open access article distributed under the Creative Commons Attribution License, which permits unrestricted use, distribution, and reproduction in any medium, provided the original work is properly cited.

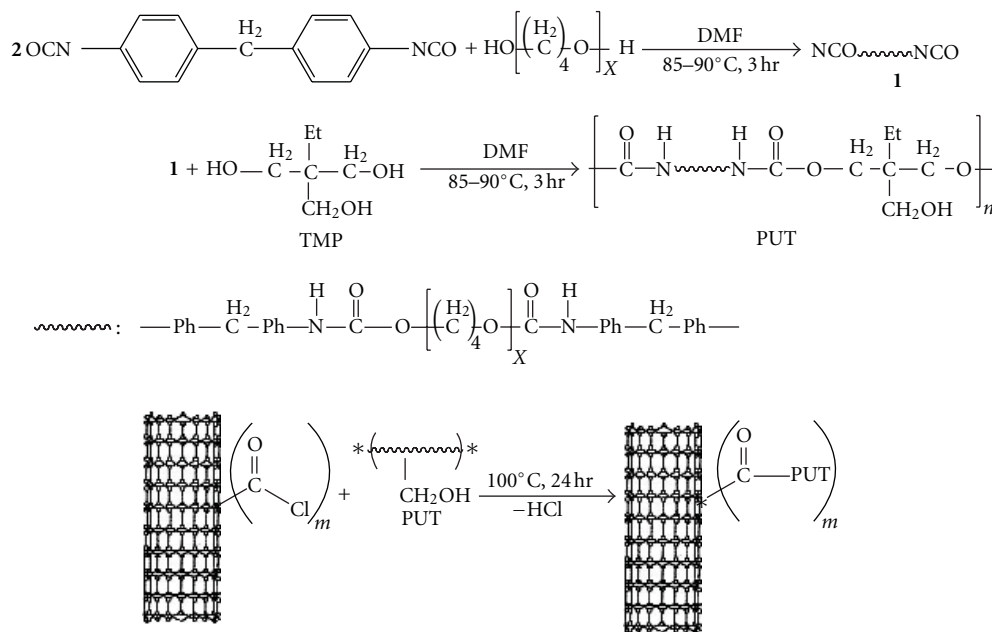
We incorporated hydroxyl groups into the polyurethane backbone and then used the “grafting to” approach to functionalize the multiwalled carbon nanotubes (MWNTs) via the esterification reaction between MWNTs and segmented polyurethanes (PUs). X-ray photoelectron spectroscopy (XPS) spectra showed that the sidewalls of MWNTs had been functionalized with acid treatment, and the amount of COOH increased with increasing acid treatment time. FTIR spectra further confirmed that PU was covalently attached to the sidewalls of MWNTs. The functionalized acid amount and the grafted PU amount were determined by thermogravimetric analyses (TGAs). Comparative studies based on SEM images of the PU-functionalized and chemically defunctionalized MWNT samples also revealed the covalent coating character. Dynamic mechanical analysis (DMA) of nanocomposite films prepared from PU and PU-functionalized MWNTs showed enhanced mechanical properties and increased soft segment T_g . Tensile properties indicated that PU-functionalized MWNTs were effective reinforcing fillers for the polyurethane matrix.

1. Introduction

In recent decades, polymer-carbon nanotube composite materials have attracted much attention for their potential applications in unique lightweight materials with distinctly superior mechanical, thermal, and electronic properties [1–4]. This can be attributed to the fascinating electronic, thermal, and mechanical properties of carbon nanotubes (CNTs) [5, 6]. With extremely high mechanical strength and chemical stability, CNTs represent attractive possibilities for developing ultrastrong composite materials [7, 8]. The effective utilization of CNTs in nanocomposite applications depends strongly on the ability to disperse the CNTs homogeneously throughout a matrix without destroying the integrity of the CNTs. The CNTs can offer a kind of nanosize reinforcement with a light weight, a hollow-core immerse aspect ratio, and an exceptionally high axial strength. Hence, significant

efforts have been made in the fabrication of these nanocomposites by dispersing either single-walled (SWNT) or multiple-walled (MWNT) carbon nanotubes into various polymer matrices.

However, the manipulation and processing of CNTs have been limited by their insolubility in most common solvents [9]. By functionalization or modification of nanosurfaces of CNTs, it has unlocked a new era in the development and applications of CNTs containing hybrid nanomaterials [10–12]. This can be generally fulfilled by the “grafting to” [13–16] and “grafting from” [17–20] approaches. Some experimental studies on CNT-reinforced polymer composites have been reported for various kinds of organic polymers, including polyethylene [21, 22] polypropylene [23], poly(methyl methacrylate) [24, 25], polystyrene [26], pitch [27], and epoxy [28, 29], with enhanced mechanical and electrical properties. More recently, polyurea-functionalized CNTs have



SCHEME 1: Synthetic route for the functionalization of MWNTs with segmented polyurethanes (PUT).

also been prepared via an in situ polycondensation approach [30]. In a similar manner, polyurethane-functionalized SWNTs have also been prepared through a two-step reaction [31]. However, Gao's and Xia's approaches could not be used in the preparation of segmented polyurethane elastomers functionalized carbon nanotubes, because polyurethane elastomers must be prepared through a prepolymer technique. In addition, although Kwon and Kim reported dispersion of CNTs in a waterborne polyurethane matrix [32, 33], the dispersion of carbon nanotubes in the polyurethane elastomer matrix was only through a noncovalent solution blending.

Elastomeric thermoplastic block copolymers are typically microphase-separation materials containing two types of segments in their molecular architecture. It was expected CNTs functionalized with polyurethane elastomers (i.e., segmented copolyurethanes or polyurethane block copolymers) via a covalent bonding would be more compatible with polyurethane elastomer matrices and hence could reinforce polyurethane elastomers. Since polyurethane block copolymers are a class of high-performance materials for versatile end use, nanocomposites prepared from polyurethane elastomers reinforced with CNTs may extend its application in various fields.

In a previous report, we have presented a methodology to bind as-prepared segmented polyurethanes to CNTs via the "grafting to" approach [34]. In this work, we incorporated hydroxyl groups into the polyurethane backbone and then used the "grafting to" approach to functionalize the MWNTs via the esterification reaction between MWNTs and PU. The segmented polyurethanes with hydroxyl groups pendant on the chain extender were synthesized by the conventional prepolymer technique. The functionalized CNTs and MWNT-PU nanohybrids have been characterized to confirm the covalent linkage. In addition, results from the fabrication

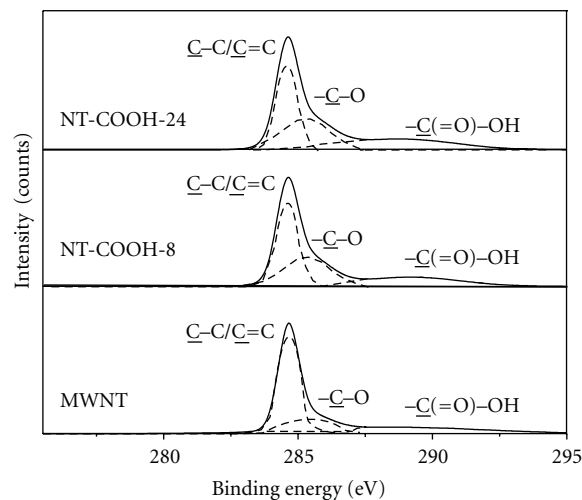


FIGURE 1: High-resolution XPS spectra of crude MWNTs and acid-treated MWNTs with different treatment times.

and characterization of the polyurethane-carbon nanotube nanocomposite films are presented and discussed.

2. Experimental

2.1. Materials. The MWNTs used in this work were purchased from Desunnano Co., Ltd.; the purity is higher than 95%. Thionyl chloride (SOCl₂) was obtained from Aldrich and used as received. 4,4'-Methylenebis(phenyl isocyanate) (MDI, Aldrich), methyl isobutyl ketone (MIBK, Hayashi Chemicals), *N,N*-dimethylformamide (DMF, Tokyo Chemicals), ethyl acetate (EA, Tokyo Chemicals), and dimethyl sulfoxide (DMSO, Nacalai Tesque, Inc.) were distilled under

reduced pressure. 1,1,1-Tris(hydroxymethyl)propane (TMP, Fluka) and tetrahydrofuran (THF, Tokyo Chemicals) were used as received. Poly(tetramethylene ether glycol) (PTMG, $\overline{M}_n = 1000$) was degassed *in vacuo* at 55°C and 600 Pa (4.5 mmHg) for 3 h to remove any absorbed water. Nitric acid (EP grade), and sulfuric acid (EP grade) were purchased from Nihon Shiyaku Industries, Ltd. and used as received.

2.2. Synthesis of the Segmented Polyurethane Elastomer (PUT). The preparation method of the segmented polyurethane elastomer carrying a pendant hydroxyl group in the chain extender has been described in our previous article [34]. GPC (DMF): $\overline{M}_n = 31,300$ g/mol, $\overline{M}_w = 51,000$ g/mol, and PDI = 1.63. The reaction is given in Scheme 1. For convenience, this polymer is designated as PUT.

2.3. Acid Treatment and Acylation of MWNTs. The detail procedures have been published previously [34]. The samples (MWNT-COOH) obtained for acid treatment of 8 and 24 h were designated as NT-COOH-8 and NT-COOH-24, respectively. After acylation, the samples (MWNT-COCl) were washed with purified EA three times and ready for esterification with PUT.

2.4. Esterification of Acylated MWNTs with PUT. 0.2 g of as-prepared MWNT-COCl was immediately reacted with 1.0 g of PUT at 100°C for 24 h, obtaining PUT-grafted MWNTs after repeated centrifugation at 7500 rpm, washing, and vacuum drying. The products (MWNT-PUT) prepared from acylation of NT-COOH-8 and NT-COOH-24 were designated as NT-PUT-8 and NT-PUT-24, respectively.

2.5. Preparation of Nanocomposite Films. In a typical experiment, the matrix PUT (4 g) was dissolved in DMF (16 mL) to form a homogeneous solution. To the solution was added dropwise a DMF solution of PUT-functionalized carbon nanotubes (NT-PUT-8) under constant stirring. The resulting solution was cast onto a glass substrate and dried at 50°C for 48 h. In this study, three different compositions, that is, 1 wt%, 5 wt%, and 10 wt% of NT-PUT-8 based on the original amount of PUT (4 g) were prepared for comparison. The composite films were designated as PUT/NT-PUT-8-1, PUT/NT-PUT-8-5, and PUT/NT-PUT-8-10, respectively.

2.6. Characterization. Infrared spectra of samples were obtained using a Bio-Rad FTS 165 Fourier transform infrared spectrometer. The spectra were obtained over the frequency range of 4000 to 400 cm^{-1} at a resolution of 4 cm^{-1} .

XPS surface analysis was carried out using a VG Instruments X-ray photoelectron spectrometer. Mg-K α radiation was used as the X-ray source and the photoelectron peaks (in the wide-scan spectra) from the samples were numerically fitted using Lorentzian curves with an integral background subtraction and analyzed at an angle of 45° to the surface. The adventitious C(1s) signal at 284.6 eV was used to calibrate the charge-shifted energy scale.

Thermogravimetric analysis (TGA) experiments were carried out on samples placed in a platinum sample pan

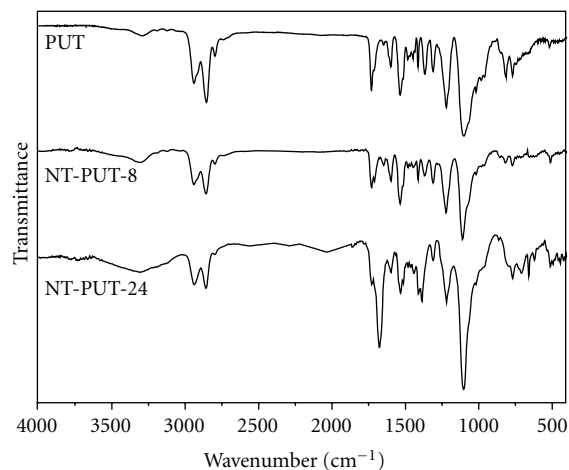


FIGURE 2: FTIR spectra of PUT, NT-PUT-8, and NT-PUT-24.

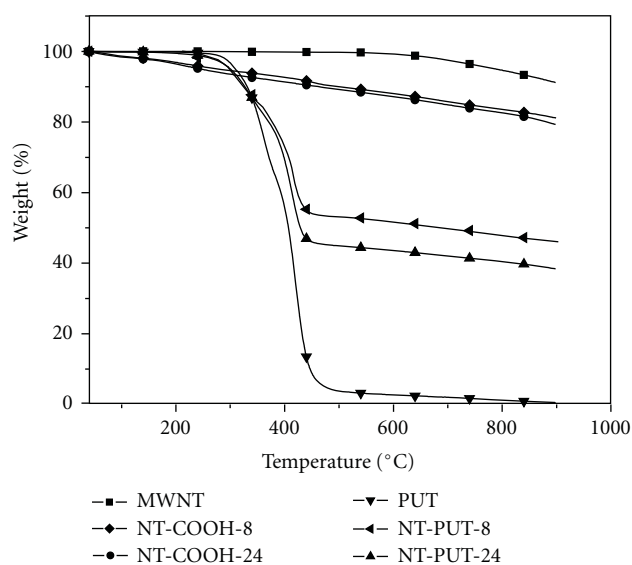


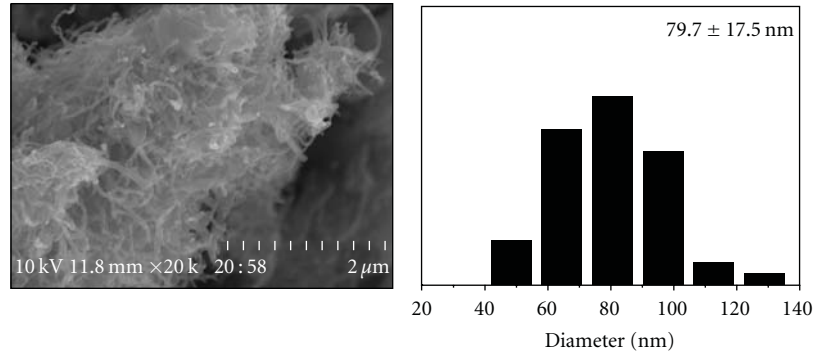
FIGURE 3: TGA weight loss curves of crude MWNTs, acid-treated MWNTs, and PUT-functionalized MWNTs under a nitrogen atmosphere.

using a TA Instruments SDT-2960 analyzer. Products ranging from 4 to 5 mg were loaded into the platinum pan and sealed in the sample chamber. The samples were heated from 50°C to 900°C under a nitrogen atmosphere at a heating rate of 10°C/min.

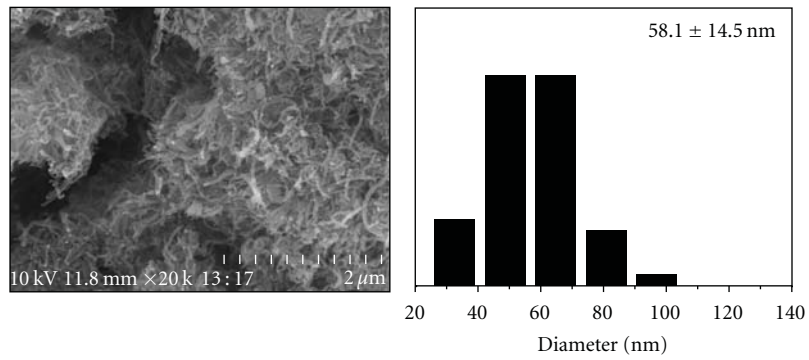
Scanning electron microscopy (SEM) images were recorded using a Hitachi S-4800 field-emission microscope, and the samples were precoated with a homogeneous gold layer by sputtering technology.

Dynamic mechanical analysis (DMA) was performed on a Perkin Elmer DMA7e unit with an operating temperature range of -100~50°C. The heating rate was set at 5°C/min. The sample size was approximately 5.5 × 1.5 × 0.5 mm³.

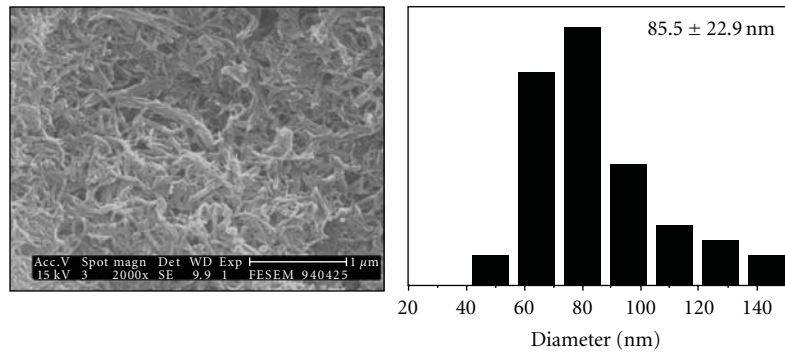
Stress-strain data of nanocomposite films were obtained using a Universal Testing Machine (Shimadzu AGS-500A Series) with a 10 kg load cell and film grips. The crosshead



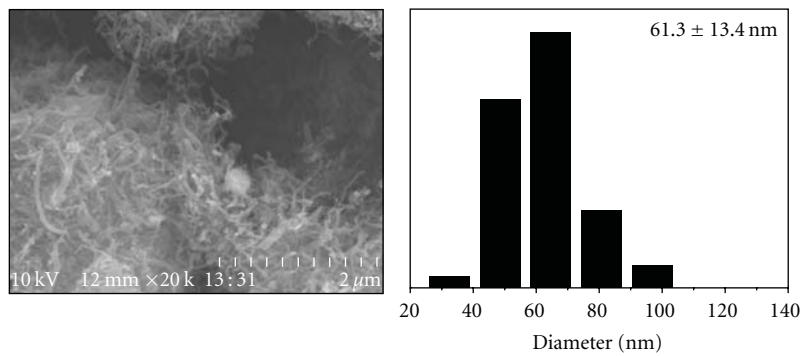
(a)



(b)



(c)



(d)

FIGURE 4: SEM micrographs of PUT-functionalized and chemically defunctionalized MWNT samples. (a) NT-PUT-8. (b) NT-PUT-8 defunctionalized at 900°C for 2 h. (c) NT-PUT-24. (d) NT-PUT-24 defunctionalized at 900°C for 2 h.

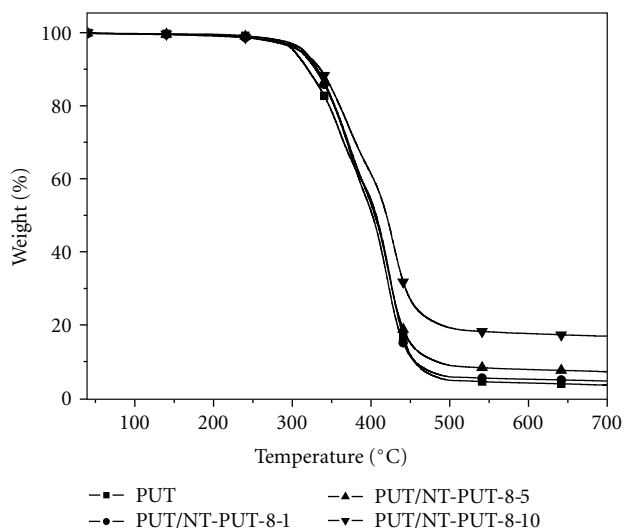


FIGURE 5: TGA weight loss curves of PUT and PUT/NT-PUT-8 nanocomposites under a nitrogen atmosphere.

speed was 20 mm/min. Measurements were made at room temperature using a $1.2 \times 0.4 \text{ cm}^2$ dumbbell sample.

3. Results and Discussion

3.1. X-Ray Photoelectron Spectroscopy (XPS) Analysis of Acid-Treated MWNTs. In our previous article, Raman spectroscopy has showed that the suitable time of acid treatment was ca. 8 h [34]. Therefore, our polymeric carbon nanocomposites discussed here and after were all prepared from NT-PUT-8 in view of processing and application.

In the present study, electron spectroscopy for chemical analysis (i.e., XPS) was further used to provide qualitative and quantitative information about the elemental composition of acid-treated MWNTs [35, 36]. In the high-resolution spectra of C(1s), as shown in Figure 1, it is evident that the C(1s) core level spectra of acid-treated MWNTs consist of three well-resolved peaks after curve-fitting. The major peak, referenced to 284.6 eV (C–C or C=C), is ascribed as unsubstituted aromatic carbon in carbon nanotubes. The peak shifted approximately 0.7 eV (i.e., at 285.3 eV) toward the higher binding energy side of the main peak corresponds to the carbon singly bound to oxygen (C–O). This is probably due to the residual oxygen after the purification step of pristine MWNTs or ether-type oxygen (–C–O–) of COOH. The small peak, present at 288.8 eV, can be attributed to the carbon double-bonded (C=O) to oxygen in the carboxylic acid groups. The quantitative results of XPS are listed in Table 1. The higher surface oxygen content for the carboxylic acid functionalized MWNTs, NT-COOH-8, and NT-COOH-24, in comparison with that of the pristine materials, is evidence of COOH groups on the MWNT surface.

3.2. Synthesis and Characterization of MWNT-Polyurethane Nanohybrids. Through the “grafting to” approach, the MWNTs were functionalized by grafting polyurethane to the

TABLE 1: (1) XPS peak position (in eV) and (2) percentage (in atom-%) from high-resolution C(1s) spectra of crude MWNTs and acid-treated MWNTs.

Sample		C–C/C=C	C–O	C(=O)–OH
MWNT	(1)	284.6 eV	285.4 eV	288.6 eV
	(2)	76.65%	16.55%	6.80%
NT-COOH-8	(1)	284.6 eV	285.3 eV	289.1 eV
	(2)	42.57%	33.44%	23.99%
NT-COOH-24	(1)	284.6 eV	285.3 eV	288.7 eV
	(2)	39.74%	34.05%	26.21%

sidewalls of MWNTs (Scheme 1). The chemical structure of the resulting MWNT-polyurethane nanohybrids is also illustrated in Scheme 1. It is noteworthy that the adsorbed polyurethane can be efficiently removed from the products by filtration and washing as mentioned in Section 2. From IR measurements for the upper layer of DMF solution, collected by centrifuging (1 h at a rate of 7500 rpm) of MWNT-PUT samples from the solution it is shown that no polyurethane signals appeared in the spectrum. This indicates that the adsorbed polymer quantity is negligible. Therefore, the “grafting to” approach presented here promised the grafting of polyurethanes onto CNT surfaces with some extent of control.

The molecular composition of the resulting MWNT-polyurethane nanohybrids was confirmed by FTIR measurements. The IR spectra of NT-PUT-8 and NT-PUT-24 are shown in Figure 2. For both samples, the characteristic absorption peaks of polyurethane such as –CH₂–, NHCOO–, and C–O–C, and clearly appear at 2930/2853, 1730, 1100 cm^{–1}, respectively. The benzene-ring C=C absorption peak from MDI is at ca. 1600 cm^{–1}, while the peaks at 1530 cm^{–1} and 1220 cm^{–1} correspond to C–N of urethane groups. This spectrum clearly shows that PUT has been grafted to MWNTs successfully.

In general, polymer-functionalized CNTs would show much higher solubility or better dispersibility as compared with pristine nanotubes. Herein, as polyurethane is polar, our resulting samples of MWNT-polyurethane are readily dispersed in polar organic solvents such as DMSO, DMF, 1-methyl-2-pyrrolidinone (NMP), and *N,N*-dimethyl acetamide (DMAc). The clear, gray solutions from the soluble samples are stable, without any precipitations over time.

3.3. Thermal Analysis of the Resulting MWNT-Polyurethane Nanohybrids. In order to obtain the grafted amount of polyurethane on MWNTs, thermal analyses of MWNT-PUT prepared from MWNTs with different times of acid treatment (8 h and 24 h) were carried out. The thermal stability for crude MWNTs and functionalized MWNTs in nitrogen is illustrated in Figure 3. As seen in the figure, the TGA curves display a two-step degradation mechanism for PUT, NT-PUT-8, and NT-PUT-24, which is quite different with the one-step degradation mechanism of MWNT and acid-treated MWNTs (MWNT-COOH, i.e., NT-COOH-8 and NT-COOH-24). It is obvious that PUT has been grafted

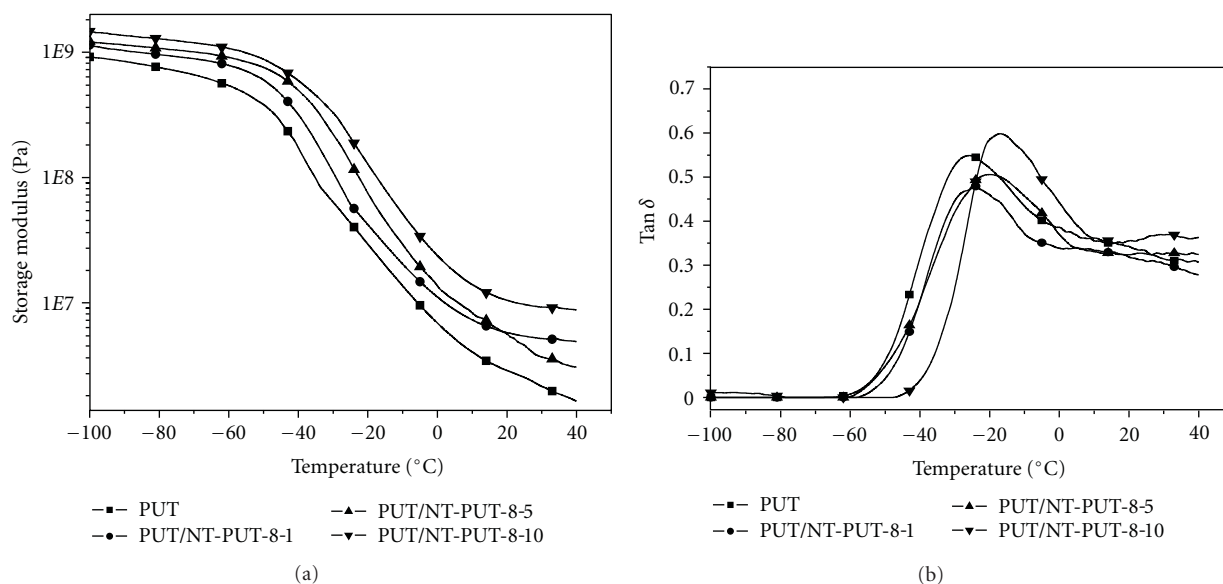


FIGURE 6: Temperature dependence of (a) storage modulus (E'); (b) loss tangent ($\tan \delta$) for PUT and PUT/NT-PUT-8 composite films.

onto the sidewalls of MWNTs. In the MWNT-COOH case, there is a continuous but not very obvious decrease in weight, which is typical for acid functionalized MWNTs. In comparison with the curves of MWNTs and acid-treated MWNTs, the rapid degradation stage in NT-PUT-8 and NT-PUT-24 may arise due to the decomposition of grafted PUT. As compared to crude MWNTs, the functionalized acid amount could be calculated by the subtraction of char yields of acid-treated MWNTs from pristine MWNT. Thus, the functionalized acid amounts for NT-COOH-8 and NT-COOH-24 are 10.0 and 12.2%, respectively. It is evident that the increased acid amount after acid treatment for 8 h is not much, demonstrating that longer acid-treated time may be not necessary. Therefore, to save the processing time for the application, our nanocomposites were only prepared from NT-PUT-8 nanohybrid. In addition, the grafted amounts of PUT were also obtained. According to the TGA traces, the PUT contents in the NT-PUT-8 and NT-PUT-24 samples are approximately 35.6% and 42.2%, respectively. It was found that the longer acid treatment time results in a higher grafted amount of PUT. This further confirms the successful functionalization of MWNTs.

3.4. Morphology of the MWNT-Polyurethane Nanohybrids.

The fine nanostructures of the as-prepared MWNT-polyurethane nanohybrids were investigated by SEM. As shown in Figures 4(a) and 4(c), MWNTs were coated by a layer of polymer chains. From the SEM images of the PUT-grafted MWNT samples, we can clearly discern that the higher the quantity of the grafted polymer, the thicker the polymer shells. The calculated diameters for NT-PUT-8 and NT-PUT-24 are ca. 79.7 and 85.5 nm, respectively. After heat treatment of NT-PUT-8 and NT-PUT-24 at 900°C for 2 h, the defunctionalized tube surfaces are relatively smooth and clean (Figures 4(b) and 4(d)), obviously different from those of the polyurethane-functionalized MWNTs. The tube

diameters are ca. 58.1 and 61.3 nm, respectively, being close to the diameter of pristine MWNTs.

3.5. Preparation and Thermal Analysis of Polyurethane Nanocomposites.

In this research, MWNTs were functionalized with PUT in order to be more compatible with the polymer matrix, PUT, of the nanocomposites. Due to the urethane groups of PUT, there are strong intermolecular interactions arising from the hydrogen bondings between PUT and MWNT-PUT nanohybrids, resulting in high compatibility between both components. The common solubility of the PUT-functionalized carbon nanotubes and the matrix PUT also makes the solution casting easier. The compatibility of the PUT-functionalized carbon nanotubes with polyurethane and the dispersion of the nanotubes in polyurethane matrix were evaluated via the fabrication of nanocomposite thin films. The PUT-functionalized carbon nanotubes used in this study are NT-PUT-8 as mentioned previously. In a typical experiment, a calculated amount of NT-PUT-8 (w/w) based on PUT matrix was dissolved in DMF and added to a PUT solution. For comparison, 1, 5, and 10 wt% of NT-PUT-8 based on 100 wt% of PUT were used as the reinforcing fillers. The nanocomposites prepared from PUT reinforced with the aforementioned amounts of NT-PUT-8 were designated as PUT/NT-PUT-8-1, PUT/NT-PUT-8-5, and PUT/NT-PUT-8-10, respectively. The resulting composite solution was allowed to settle overnight and then centrifuged to remove any residual insoluble species, followed by being concentrated to attain the desired viscosity. The viscous but transparent solution was used for the casting of a thin film. The polyurethane-MWNT composite thin film thus obtained is transparent with a high optical quality. The successful fabrication of optically high-quality nanocomposite thin films reflects the excellent compatibility of the PUT-functionalized carbon nanotubes with polyurethane. It also serves as initial evidence for the notion

TABLE 2: Composition and physical properties of PUT and PUT/NT-PUT-8 composite films.

Specimens	Composition (wt%) PUT/NT-PUT-8	T_g ($^{\circ}\text{C}$) (soft segment)	Storage modulus at -40°C (GPa)	Tensile strength (KPa)	Elongation at break (%)
PUT	100/0	-26	0.918	180	195
PUT/NT-PUT-8-1	100/1	-24	1.14	286	192
PUT/NT-PUT-8-5	100/5	-19	1.22	344	173
PUT/NT-PUT-8-10	100/10	-17	1.47	675	116

that functionalized carbon nanotubes can be dispersed homogeneously into polymeric matrices. According to TGA results shown in Figure 5, it is obvious that the thermal stability of nanocomposites increases with increasing amounts of PUT-functionalized carbon nanotubes. As a result, the degradation temperature (ca. 335°C) of 10% weight loss for PUT/NT-PUT-8-10 composite is ca. 16°C higher than that of neat PUT. In addition, compared to the char yield (ca. 3.5%) of neat PUT, the higher char yield (ca. 16.9%) for this composite demonstrates that the effect of enhanced thermal stability due to the PUT-functionalized MWNTs may occur.

3.6. Mechanical Properties of Polyurethane Nanocomposites.

Dynamic mechanical analysis (DMA) is most useful for studying the viscoelastic behavior of polymers. The mechanical properties and stiffness of the polyurethane nanocomposites were then analyzed with DMA. In the polyurethane composite, PUT-functionalized MWNTs serve as the reinforcement and segmented PUT acts as the matrix. Increasing the amount of NT-PUT-8 in the composite increased the storage modulus due to stronger intermolecular interactions between MWNT-PUT nanohybrid and PUT. The soft segment T_g s of the three composite films were also obtained from loss tangent of DMA. As shown in Figure 6, the dynamic storage modulus (E') and loss tangent ($\tan \delta$) of the PUT/NT-PUT-8 nanocomposite films show enhanced mechanical properties and increased soft segment T_g . The results of soft segment T_g of the three composites are listed in Table 2. The enhanced E' s of PUT/NT-PUT-8 nanocomposites are induced from the stiffening effect of the CNTs. E' of the PUT/NT-PUT-8 nanocomposite films prepared in this study increases with increasing NT-PUT-8 content, which is due to the stiffening effect of the NT-PUT-8. In comparison with the E' values of PUT, the E' s of the three nanocomposites are significantly improved, indicating a strong adhesion between the reinforcement and the matrix. For the convenience of comparison, data of E' at -40°C are also shown in Table 2. Moreover, with increasing NT-PUT-8 content, the glass-transition temperature of the soft segments of the PUT/NT-PUT-8 nanocomposite films shifts from -26 to -17°C . The increase of soft segment T_g is attributed to the constraint of polyurethane chains by carbon nanotubes. This means that NT-PUT-8 nanohybrids are compatible with the amorphous regions of the soft segments in PUT matrix.

Figure 7 shows the stress-strain curves of the PUT film and PUT/NT-PUT-8 nanocomposite films. The results of tensile strength and elongation at break of the PUT/NT-

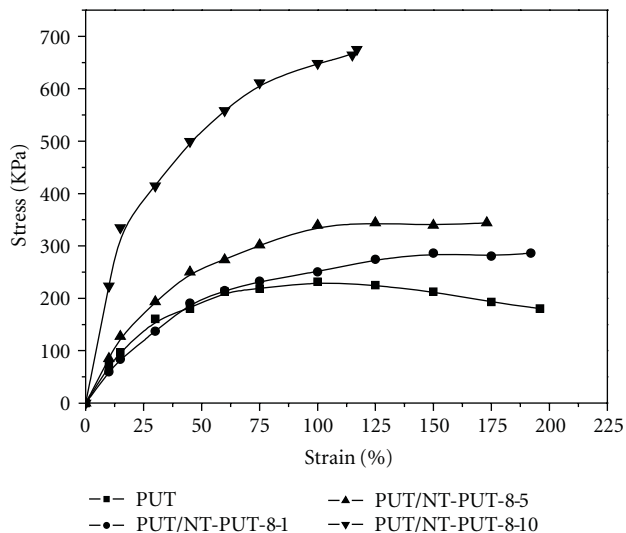


FIGURE 7: Stress-strain curves for PUT and PUT/NT-PUT-8 composite films.

PUT-8 nanocomposite films are also summarized in Table 2. The tensile strengths of the nanocomposite films are enhanced with 1 wt% to 10 wt% loading of NT-PUT-8 compared to the corresponding value of the original PUT film. As the NT-PUT-8 content increased from 1 wt% to 10 wt%, the tensile strength of the PUT/NT-PUT-8 nanocomposite films increases from 286 to 675 KPa, corresponding to an increasing ratio of 59 to 275%; however, the elongation at break (% of strain) decreased from 192 to 116%. The increase of tensile strength in the PUT/NT-PUT-8 nanocomposites is due to the reinforcing effect of NT-PUT-8 in the PUT matrix.

4. Conclusions

MWNTs were covalently functionalized with segmented polyurethanes using the "grafting to" technique. The segmented polyurethane (PUT) with hydroxyl groups pendant on the polymer backbone was synthesized by the conventional pre-polymer technique. The functionalized MWNT-COCl was then reacted with polyurethane to prepare the MWNT-polyurethane nanohybrids. By XPS analysis, the presence of C(=O) (1s) for acid-treated MWNTs indicated the successful oxidation of MWNTs. From the characteristic peaks of PUT shown in IR spectra, PUT has been grafted to the surfaces of MWNTs successfully. TGA results indicated that

acid treatment time for 8 h might be enough. SEM investigations gave direct evidence of the nanostructures of the MWNT-PUT hybrids. The MWNT-PUT nanohybrids were well dispersed in the same solvents for neat PU, thus allowing the intimate mixing of the functionalized nanotubes with the matrix polymer for the preparation of nanocomposites. Dynamic mechanical analysis showed the storage modulus and the soft segment T_g of the nanocomposites increased with increasing NT-PUT-8 content. The tensile strengths of the nanocomposite films with different weight ratio loading of NT-PUT-8 were enhanced by about 59 to 275%, compared to the corresponding value of the original PUT film.

References

- [1] A. L. Martínez-Hernández, C. Velasco-Santos, and V. M. Castaño, "Carbon nanotubes composites: processing, grafting and mechanical and thermal properties," *Current Nanoscience*, vol. 6, no. 1, pp. 12–39, 2010.
- [2] T. Kashiwagi, E. Grulke, J. Hilding et al., "Thermal and flammability properties of polypropylene/carbon nanotube nanocomposites," *Polymer*, vol. 45, no. 12, pp. 4227–4239, 2004.
- [3] W. Bauhofer and J. Z. Kovacs, "A review and analysis of electrical percolation in carbon nanotube polymer composites," *Composites Science and Technology*, vol. 69, no. 10, pp. 1486–1498, 2009.
- [4] B. Fan, X. Mei, K. Sun, and J. Ouyang, "Conducting polymer/carbon nanotube composite as counter electrode of dye-sensitized solar cells," *Applied Physics Letters*, vol. 93, no. 14, Article ID 143103, 2008.
- [5] M. S. Dresselhaus, G. Dresselhaus, and P. C. Eklund, *Science of Fullerenes and Carbon Nanotubes*, Academic Press, New York, NY, USA, 1996.
- [6] R. Saito, M. S. Dresselhaus, and G. Dresselhaus, *Physical Properties of Carbon Nanotubes*, Imperial College Press, London, UK, 1998.
- [7] P. M. Ajayan, L. S. Schadler, C. Giannaris, and A. Rubio, "Single-walled carbon nanotube-polymer composites: strength and weakness," *Advanced Materials*, vol. 12, no. 10, pp. 750–753, 2000.
- [8] B. Ni and S. B. Sinnott, "Chemical functionalization of carbon nanotubes through energetic radical collisions," *Physical Review B*, vol. 61, no. 24, pp. R16343–R16346, 2000.
- [9] J. Chen, M. A. Hamon, H. Hu et al., "Solution properties of single-walled carbon nanotubes," *Science*, vol. 282, no. 5386, pp. 95–98, 1998.
- [10] R. H. Baughman, A. A. Zakhidov, and W. A. De Heer, "Carbon nanotubes—the route toward applications," *Science*, vol. 297, no. 5582, pp. 787–792, 2002.
- [11] X. Chen and S. P. Armes, "Surface polymerization of hydrophilic methacrylates from ultrafine silica sols in protic media at ambient temperature: a novel approach to surface functionalization using a polyelectrolytic macroinitiator," *Advanced Materials*, vol. 15, no. 18, pp. 1558–1562, 2003.
- [12] A. Hirsch, "Functionalization of single-walled carbon nanotubes," *Angewandte Chemie International Edition*, vol. 41, no. 11, pp. 1853–1859, 2002.
- [13] Y. P. Sun, K. Fu, Y. Lin, and W. Huang, "Functionalized carbon nanotubes: properties and applications," *Accounts of Chemical Research*, vol. 35, no. 12, pp. 1096–1104, 2002.
- [14] R. Czerw, Z. Guo, P. M. Ajayan, Y. P. Sun, and D. L. Carroll, "Organization of polymers onto carbon nanotubes: a route to nanoscale assembly," *Nano Letters*, vol. 1, no. 8, pp. 423–427, 2001.
- [15] S. Qin, D. Qin, W. T. Ford, D. E. Resasco, and J. E. Herrera, "Functionalization of single-walled carbon nanotubes with polystyrene via grafting to and grafting from methods," *Macromolecules*, vol. 37, no. 3, pp. 752–757, 2004.
- [16] Y. Lin, B. Zhou, K. A. S. Fernando, P. Liu, L. F. Allard, and Y. P. Sun, "Polymeric carbon nanocomposites from carbon nanotubes functionalized with matrix polymer," *Macromolecules*, vol. 36, no. 19, pp. 7199–7204, 2003.
- [17] M. S. P. Shaffer and K. Kozioł, "Polystyrene grafted multi-walled carbon nanotubes," *Chemical Communications*, no. 18, pp. 2074–2075, 2002.
- [18] W. Wu, S. Zhang, Y. Li et al., "PVK-modified single-walled carbon nanotubes with effective photoinduced electron transfer," *Macromolecules*, vol. 36, no. 17, pp. 6286–6288, 2003.
- [19] H. Kong, C. Gao, and D. Yan, "Controlled functionalization of multiwalled carbon nanotubes by in situ atom transfer radical polymerization," *Journal of the American Chemical Society*, vol. 126, no. 2, pp. 412–413, 2004.
- [20] I. C. Liu, H. M. Huang, C. Y. Chang, H. C. Tsai, C. H. Hsu, and R. C. C. Tsiang, "Preparing a styrenic polymer composite containing well-dispersed carbon nanotubes: anionic polymerization of a nanotube-bound p-methylstyrene," *Macromolecules*, vol. 37, no. 2, pp. 283–287, 2004.
- [21] S. L. Ruan, P. Gao, X. G. Yang, and T. X. Yu, "Toughening high performance ultrahigh molecular weight polyethylene using multiwalled carbon nanotubes," *Polymer*, vol. 44, no. 19, pp. 5643–5654, 2003.
- [22] W. Tang, M. H. Santare, and S. G. Advani, "Melt processing and mechanical property characterization of multi-walled carbon nanotube/high density polyethylene (MWNT/HDPE) composite films," *Carbon*, vol. 41, no. 14, pp. 2779–2785, 2003.
- [23] S. A. Gordeyev, F. J. MacEdo, J. A. Ferreira, F. W. J. Van Hattum, and C. A. Bernardo, "Transport properties of polymer-vapour grown carbon fibre composites," *Physica B*, vol. 279, no. 1–3, pp. 33–36, 2000.
- [24] Z. Jia, Z. Wang, C. Xu et al., "Study on poly(methyl methacrylate)/carbon nanotube composites," *Materials Science and Engineering A*, vol. 271, no. 1–2, pp. 395–400, 1999.
- [25] Z. Jin, K. P. Pramoda, G. Xu, and S. H. Goh, "Dynamic mechanical behavior of melt-processed multi-walled carbon nanotube/poly(methyl methacrylate) composites," *Chemical Physics Letters*, vol. 337, no. 1–3, pp. 43–47, 2001.
- [26] D. Qian, E. C. Dickey, R. Andrews, and T. Rantell, "Load transfer and deformation mechanisms in carbon nanotube-polystyrene composites," *Applied Physics Letters*, vol. 76, no. 20, pp. 2868–2870, 2000.
- [27] R. Andrews, D. Jacques, A. M. Rao et al., "Nanotube composite carbon fibers," *Applied Physics Letters*, vol. 75, no. 9, pp. 1329–1331, 1999.
- [28] L. S. Schadler, S. C. Giannaris, and P. M. Ajayan, "Load transfer in carbon nanotube epoxy composites," *Applied Physics Letters*, vol. 73, no. 26, pp. 3842–3844, 1998.
- [29] J. M. Park, D. S. Kim, J. R. Lee, and T. W. Kim, "Nondestructive damage sensitivity and reinforcing effect of carbon nanotube/epoxy composites using electro-micromechanical technique," *Materials Science and Engineering C*, vol. 23, no. 6–8, pp. 971–975, 2003.
- [30] C. Gao, Y. Z. Jin, H. Kong et al., "Polyurea-functionalized multiwalled carbon nanotubes: synthesis, morphology, and Raman spectroscopy," *Journal of Physical Chemistry B*, vol. 109, no. 24, pp. 11925–11932, 2005.

- [31] H. Xia and M. Song, "Preparation and characterisation of polyurethane grafted single-walled carbon nanotubes and derived polyurethane nanocomposites," *Journal of Materials Chemistry*, vol. 16, no. 19, pp. 1843–1851, 2006.
- [32] J. Kwon and H. Kim, "Comparison of the properties of waterborne polyurethane/multiwalled carbon nanotube and acid-treated multiwalled carbon nanotube composites prepared by in situ polymerization," *Journal of Polymer Science Part A*, vol. 43, no. 17, pp. 3973–3985, 2005.
- [33] J. Kwon and H. Kim, "Preparation and properties of acid-treated multiwalled carbon nanotube/waterborne polyurethane nanocomposites," *Journal of Applied Polymer Science*, vol. 96, no. 2, pp. 595–604, 2005.
- [34] T. L. Wang and C. G. Tseng, "Polymeric carbon nanocomposites from multiwalled carbon nanotubes functionalized with segmented polyurethane," *Journal of Applied Polymer Science*, vol. 105, no. 3, pp. 1642–1650, 2007.
- [35] D. A. Skoog and F. J. Holler, *Principles of Instrumental Analysis*, Saunders, Philadelphia, Pa, USA, 5th edition, 1992.
- [36] E. Y. Kim, J. S. Kong, S. K. An, and H. D. Kim, "Surface modification of polymers and improvement of the adhesion between evaporated copper metal film and a polymer. I. Chemical modification of PET," *Journal of Adhesion Science and Technology*, vol. 14, no. 9, pp. 1119–1130, 2000.

Research Article

A Comparative Study of Dispersion Techniques for Nanocomposite Made with Nanoclays and an Unsaturated Polyester Resin

Farida Bensadoun, Nadir Kchit, Catherine Billotte, François Trochu, and Edu Ruiz

*Chair on Composites of High Performance (CCHP), Research Centre on Plastics and Composites (CREPEC),
Department of Mechanical Engineering, École Polytechnique de Montréal, P.O. Box 6079, Station Centre-Ville,
Montreal, QC, Canada H3C 3A7*

Correspondence should be addressed to Edu Ruiz, edu.ruiz@polymtl.ca

Received 12 April 2011; Revised 19 July 2011; Accepted 23 August 2011

Academic Editor: Gaurav Mago

Copyright © 2011 Farida Bensadoun et al. This is an open access article distributed under the Creative Commons Attribution License, which permits unrestricted use, distribution, and reproduction in any medium, provided the original work is properly cited.

Over the last few years, polymer/clay nanocomposites have been an area of intensive research due to their capacity to improve the properties of the polymer resin. These nanocharged polymers exhibit a complex rheological behavior due to their dispersed structure in the matrix. Thus, to gain fundamental understanding of nanocomposite dispersion, characterization of their internal structure and their rheological behavior is crucial. Such understanding is also key to determine the manufacturing conditions to produce these nanomaterials by liquid composite molding (LCM) process. This paper investigates the mix of nanoclays particles in an unsaturated polyester resin using three different dispersion techniques: manual mixing, sonication, and high shear mixing (HSM). This paper shows that the mixing method has a significant effect on the sample morphology. Rheology, scanning electron microscopy (SEM), and differential scanning calorimetry (DSC) characterization techniques were used to analyze the blends morphology and evaluate the nanoclays stacks/polymer matrix interaction. Several phenomena, such as shear thinning and premature polymer gelification, were notably observed.

1. Introduction

Recent advances in the composite materials field are related to the addition of nanoparticles such as carbon nanotubes or nanoclays to improve thermal, mechanical, or electrical properties. Nanoparticle additives, like nanoclays, are widely used in various industries such as cable coatings, adhesives, inks, pharmaceuticals and automotives [1, 2]. One of the most common nanoclay forms is MMT layered silicate with a particle thickness of 1 nm and 70 to 100 nm crosswise silica platelets [3]. The choice of montmorillonite nanoparticles in previous researches is mainly due to the fact that they are commonly available in nature and inexpensive. A minimal content of such additives between 1 to 6% wt can improve the properties of the polymer matrix by increasing flexural modulus by up to 31% and lowering the coefficient of linear thermal expansion by 66% [1, 4, 5]. However, the incorporation of nanoparticles into the liquid matrix is

still a challenge, because it requires proper dispersion and exfoliation. Nanoclays are widely used in thermoplastic matrices, but only few studies report to their addition in polyester thermoset resins. This explains the lack of results on the thermal and mechanical properties and especially on the rheology of the mix.

Rheology is a widely used evaluation method for detecting the presence of interconnected structures. This technique seems to be relevant for the study of the dispersion state which defines the nanostructure of the mixture between the conventional, the intercalated, or exfoliated nanocomposite as illustrated in Figure 1. However, in practice, the final mixture would probably be a combination of these three morphologies, where the best-case scenario is the fully exfoliated structure [1, 6]. Due to the high aspect ratio of the platelets, a small percentage of nanoclay particles properly dispersed in the matrix can generate a very large surface

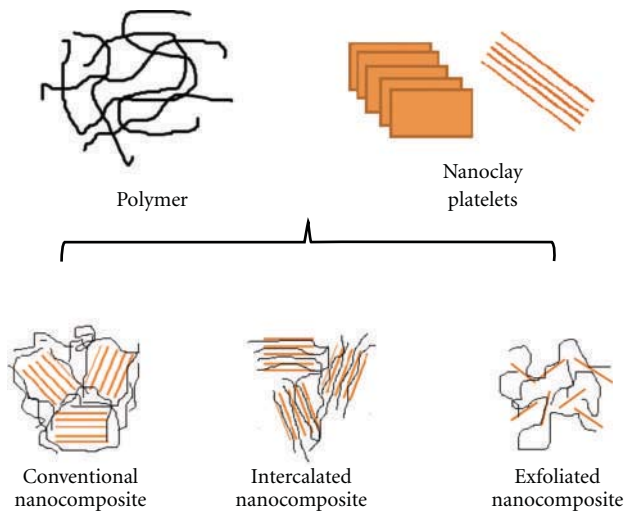


FIGURE 1: States of dispersion of nanoclay platelets.

area for polymer/filler interactions [1, 6]. Many factors can influence the dispersion and exfoliation of the nanoparticles in the polymer. The final properties of the nanostructure will mainly depend on the choice of the mixing technique and the resulted degree of exfoliation of the nanoclay platelets [7, 8]. Techniques such as in situ polymerization, solution mixing, or sonication are widely used to disperse nanoparticles in a liquid. The latter technique in particular seems to be relatively effective to obtain an exfoliated structure [1, 9, 10]. The changes of morphology of the mix are associated to the dispersion of the nanoparticles in the liquid matrix. When using a Newtonian polymer, the morphology change is detectable with rheology analyzes by the apparition of a shear-thinning behaviour [1, 7, 11, 12]. This non-Newtonian behaviour can be attributed to various factors such as the change in the nanoparticles volume fraction, shape, and size or size distribution [6, 12]. This decrease of viscosity is due to the reorientation of the layered silicate (MMT) in the direction of flow in response to the external applied shear [8, 13, 14]. The degree of the shear-thinning can then be used as an indicator of the exfoliation state of the nanoclays inside the polymer matrix; a steeper slope can be associated to an exfoliated mixture [7, 8]. When the shear stress is released after testing, a restructuration to the original disorganized structure of the nanoclay is initiated. The viscosity of the blend gradually go back to its original steady-state value [13].

The presence of layered silicates in nonaqueous polymers changes the viscoelastic behavior of the unfilled matrix from liquid-like ($G' \propto \omega^2$) to solid-like ($G' \propto \omega^0$) because of the formation of a three-dimensional percolating network of exfoliated or intercalated stacks [15]. This gel-like behavior is a direct consequence of the highly anisotropic nature of the nanoclays which prevents their free rotation and the dissipation of stress [16]. This superstructure formation will directly affect the polymerization reaction [14, 17, 18]. The presence of this gel-like structure limits the cross-linking altering the curing reaction because of the reduction of

the molecular mobility and thus free volume [19]. This limitation is not attributed to the resin nature itself which generally follows the rule of mixtures, but to the presence of nanoclays leading to a more complex chemical behavior [20]. According to Gholizadeh et al. [21], the addition of nanoclay decreases the free volume. On the other hand, Yu et al. [22] observed an increase in free volume after the addition of bentonite clay attributed to the cyanate ester polymer/nanoparticles interaction. The effect of the nanoplatelets on the free volume depends on the clay/polymer interactions, and this type of characterization seems to give contradicting results. These interactions can be affected by the interfacial region, the interstitial cavities of agglomerates, the chain segments mobility of the polymer, or the cross-linking density [23]. The composition of the polymer matrix and the nanoclay surface treatment will also influence the curing reaction [20, 24].

From the manufacturing point of view, the gel time is a critical parameter for proper composites molding [25, 26]. It was observed in the past that the level of exfoliation of nanoclay platelets has an important impact on resin cure causing premature cross-linking [17]. Goertzen et al. [27] did a rheokinetic study on fumed silicate nanocharged cyanate ester resin at various volume fraction up to 3.4%. They have observed a reduction in gel time by 9% during isothermal cure at 130°C because of the nanoparticles. In similar way, the addition of nanoclay to an epoxy/diamine resin was found to enhance the curing reaction [28]. Generally speaking, the organoclays tend to facilitate the homopolymerisation reaction because of the catalytic action of the octadecylammonium ions of the clays [24, 28, 29].

Other techniques, such as electron microscopy and XRD, are also widely used to characterize the dispersion state of the nanoparticles in the polymer matrix. Due to its high resolution, TEM is suitable only at nanoscale which is not necessarily representative of the entire composite sample at the macroscale. Moreover, sample preparation for TEM analysis is quite complex and time consuming, and results are not guaranteed regarding the cost of such characterization. On the other hand, SEM allows observations of the nanocomposites internal structure at larger scales than TEM. The micro-scale could reveal the size and distribution of agglomerates in a more representative sample [30]. Combined to rheology characterization, SEM microscopy is a good indicator of the dispersion of nanoparticles in the resin and may also confirm the level of exfoliation.

This present study focuses on the mixing techniques and the understanding of the dispersion of nanoclays in unsaturated polyester resin. The main challenge is to achieve exfoliation of large stacks of clay nano-platelets into single layers keeping in mind the manufacturing process limitations. A previous study [31] already identifies the main process parameters to consider for proper injection of a nanoclay reinforced resin and impregnation of natural fibers by LCM. This work has also shown improved mechanical and flammability properties of nanoclay reinforced UP. Three dispersion methods were investigated on this study: manual mixing, sonication, and high shear mixing will be investigated. The dispersion state of nanoparticles in the

TABLE 1: Properties of the nanoclay platelets used in this work.

Type	D-spacing	Density	Surface treatment
Cloisite 30B	18.5 Å	1.98 g/mL	Alkyl quaternary ammonium bentonite

matrix will be evaluated using both rheology and SEM analyses. The catalytic effect of the nanoclays will also be investigated by gel time measurements and cure kinetics study using rheology and M-DSC techniques. The main objective of this research is to identify the most efficient dispersion technique and its impact on rheological and cure kinetics on nanocharged UP matrix keeping in consideration future manufacturing possibilities.

2. Experimental

2.1. Material. In this work, an unsaturated polyester petroleum-based resin (UP) R937-DPE24 from AOC was used, which has an average viscosity of 0.1804 Pa.s at 23°C. The resin was prepromoted with cobalt ethylhexanoate and initiated using 1.5 phr of methyl ethyl ketone peroxide (MEKP 925) from Norox. The resin was reinforced using 3% wt of Cloisite 30B nanoclay from Southern Clay Products. These nanoparticles are organically modified layered magnesium aluminum silicates and their properties are summarized in Table 1.

2.2. Nanoclay Dispersion. A good dispersion is a key challenge to achieve the best possible combination of matrix-nanoparticles. For that reason, a new dispersion technique using high shear mixer was investigated in this work and compared to sonication and manual mixing. The choice of the 3% wt Cloisite 30B was notably based on previous researches [31, 32] showing that these type of nanoparticles are easier to disperse due to their chemistry providing general improvement on the matrix properties. Furthermore this type of nanoclay was investigated in an earlier study focusing on composites manufacturing [31], and the mass fraction of 3% wt was considered adequate for RTM processing.

The sonication and manual preparations are detailed in a previous study [31]. In these techniques, the nanoclays were incorporated and predispersed in styrene first. The resin was then added to the mix and the styrene in excess was evaporated using high-speed mechanical stirring. The amount of each component was weight controlled. Since the HSM is performed in a sealed chamber, the nanoclays were directly incorporated into the resin. The gap in the geometry interaction chamber has been fixed between 50 and 100 microns, and the resin was circulated inside the chamber at high pressure. The size of particles agglomerates was significantly reduced with this mixing technique resulting in a well-dispersed and homogeneous blend. Figure 2 summarizes the blend preparation procedures with the different approaches. The letter A refers to sonication technique whereas the letters B to high shear mixing. Pure and nanocharged resins were mixed by three methods in order to take into account the possible effect of the mixing technique on the resin itself. The

temperature and pressure were maintained at 23°C and 1 atm for (A0) and (A1) blends to limit the possible formation of microgels or styrene evaporation.

2.3. Rheology and Electron Microscopy. Rheology experiments were conducted using a combined motor and transducer (CMT) rheometer MCR501 from Anton-Paar. Both steady shear and small amplitude oscillatory shear (SAOS) measurements were carried out using two types of geometries: parallel plates of 25 cm diameter with a constant gap of 1 mm for high-viscosity blends and concentric cylinders for low-viscosity blends. All experiments were conducted at 23°C and before measurement the sample was left in the geometry for stabilization for 20 minutes. Plastic paraffin films (parafilm) were placed above the mixtures to limit styrene evaporation during the stabilisation stage. This film limits the air contact of the liquid resin and styrene evaporation can be neglected. The steady shear measurements were performed using a shear rate varying from 0.1 to 1000 s⁻¹.

For steady shear viscosity, the non-Newtonian viscosity η is defined as follows [19, 33]:

$$\eta(\dot{\gamma}) = \frac{-\tau_{21}}{\dot{\gamma}}, \quad (1)$$

where τ_{21} is the shear stress, and $\dot{\gamma}$ the shear rate applied. The SAOS experiments were carried out under strain amplitudes of 1%, inside the linear viscoelasticity (LVE) domain. Frequency sweep test measurements were performed at frequencies varying from 0.1 to 100 Hz. A strain wave was imposed to the sample and the SAOS shear stress response $\tau_{21}(t)$ defined as follows [19, 33]:

$$-\tau_{21}(t) = (\tau_0 \cos(\delta)) \sin(\omega t) + (\tau_0 \sin(\delta)) \cos(\omega t), \quad (2)$$

where τ_0 is the stress amplitude, ω the angular frequency, and δ the phase difference between the strain wave and the stress response. For elastic solids, the shear stress is directly proportional to the strain imposed as defined by Hooke's law:

$$\tau_{21} = -G \cdot \gamma_{21} = -G \cdot \gamma_0, \quad (3)$$

where $\gamma_0 = \dot{\gamma}_0/\omega$ is the strain amplitude and G the elastic modulus. Equations (2) and (3) can be combined to obtain the SAOS material function:

$$-\frac{\tau_{21}}{\gamma_0} = G' \sin(\omega \cdot t) + G'' \cos(\omega \cdot t), \quad \tan(\delta) = \frac{G''}{G'}, \quad (4)$$

where G' is the storage modulus and G'' the loss modulus, related, respectively, to the energy stored (elastic contribution) and dissipated (viscous contribution). The ratio between modulus is defined as the damping factor $\tan \delta$. The complex viscosity $\eta^*(\omega)$ is finally defined as

$$\eta^*(\omega) = \frac{-\tau_{21}(t)}{\dot{\gamma}_{21}(t)}, \quad (5)$$

where $\dot{\gamma}_{21}(t)$ is the SAOS strain rate.

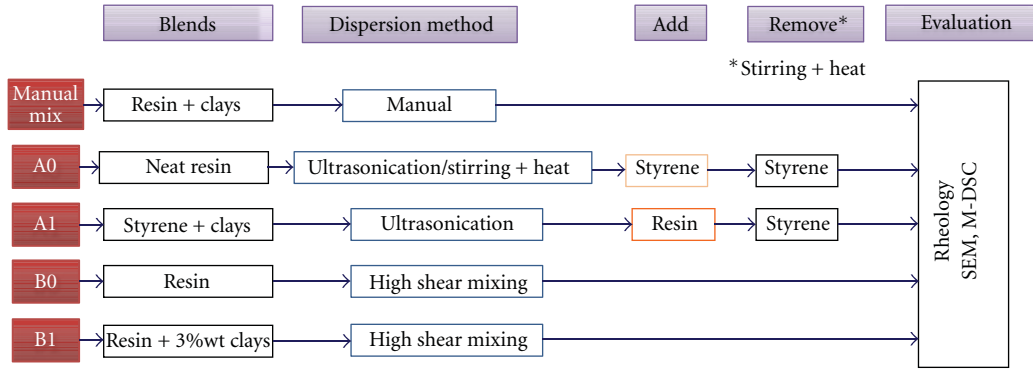


FIGURE 2: Mixing techniques used for nanoclay dispersion in the resin matrix: manual mixing, sonication (a), and high shear mixing (b).

In order to quality the size of the agglomerates and thus, evaluate the quality of the nanoreinforced blends, scanning electron microscopy (SEM) technique is used. A field emission gun scanning electron microscope (FEG-SEM-4700) from Hitachi is used at an operation voltage of 2 kV. FEG-SEM was used to investigate the distribution of clay in the Epoxy matrix. The smooth and flat surface of specimens were prepared using Ultracut FC microtome (*Leica*) with a diamond knife and then coated with platinum. This device cuts thin slices of nanocomposite to the desired thickness and the observed area is around 100 μm .

2.4. Calorimetry. The addition of nanoclay particles in the UP resin can cause premature cross-linking of the matrix which could be the source of composite part failure and restrict the manufacturing capabilities. Consequently, it is important to understand the effects of nanoclays on the resin cure kinetic. In order to see the possible catalytic effect of nanoparticles, calorimetry experiments were performed on blends A and B and on the resin alone. First, the samples were isothermally maintained at 70°C for different periods of time up to 24 hours in order to study the effect of the storage conditions on the nanocharged mixtures. Afterwards, the MEKP catalyst was added to the blend and samples were cured on the DSC at a dynamic ramp of 10°C/min from room temperature to 250°C. The instrument used on this study is a modulated differential scanning calorimeter (M-DSC) Q1000 from TA Instrument. This instrument has the great advantage of being able to separate the heat flow related to the cure kinetic from the changes in thermodynamic heat capacity. The instantaneous heat generated during the polymerization reaction can be expressed as follows [26, 34]:

$$\frac{dH}{dt} = \Delta H_R \frac{d\alpha}{dt}, \quad (6)$$

where ΔH_R is the total heat of reaction measured by M-DSC and $d\alpha/dt$ the reaction rate. If the diffusion of chemical species is neglected, the reaction rate is assumed to be a unique function of the degree of conversion α and temperature T and this expression takes the form of

$$\frac{d\alpha}{dt} = f(T, \alpha), \quad \alpha = \int_0^t \frac{d\alpha}{dt} \cdot dt \quad (7)$$

and the total heat of reaction corresponds to the area under the nonreversing heat flux curve measured by M-DSC [26, 34].

3. Results and Analyses

3.1. Rheology Analyses. In this work, the quality of the dispersion of nanoclays in the liquid resin was evaluated from rheology tests knowing that a high initial viscosity and strong shear thinning behavior are often associated to a high level of exfoliation of the nanoclay platelets [1, 6]. This rheological behavior illustrates the ability of the nanoclays to “interact” with the polymer matrix and is intimately related to the clay type, its surface treatment, and affinity with the polymeric matrix [6, 32].

Figure 3 illustrates the viscosity change with shear rate for eight samples dispersed by three different mixing techniques. As shown, the resin viscosity increases after the addition of the nanoparticles with the three mixing techniques studied in this work. The initial viscosity can rise over 3 decades. The mixing techniques does not influence the pure resin viscosity as illustrated by the A0 and B0 curves showing the same Newtonian behavior with a viscosity around 0.20 Pa.s, close to the manufacturer data of 0.1804 Pa.s. For the manually mixed blend, the size of particles is probably still quite large due to high probability of aggregates. The sonication mix (A1) results in a slight non-Newtonian shear thinning behavior with an increase of the initial viscosity to 0.80 Pa.s. This can be attributed to a better dispersion and possible intercalation of the nanoclay platelets. On the other hand, the high shear mixing (B1) blends show a strong shear thinning behavior with an initial viscosity varying from 70 to 250 Pa.s. The initial viscosity increases with the number of passes in the high shear chamber. However, at higher shear rates (20 s^{-1} and over), the viscosity of the nanoreinforced resin is below 10 Pa.s. This value has been previously estimated as the processability limit to manufacture composite parts by RTM [31]. In the case of the high shear mixing blends, the number of passes will have an important influence on the initial viscosity of the nanocharged resin. After two passes, the nanoclays platelets seem to reach their maximum possible exfoliated state, the interactions between the platelets are

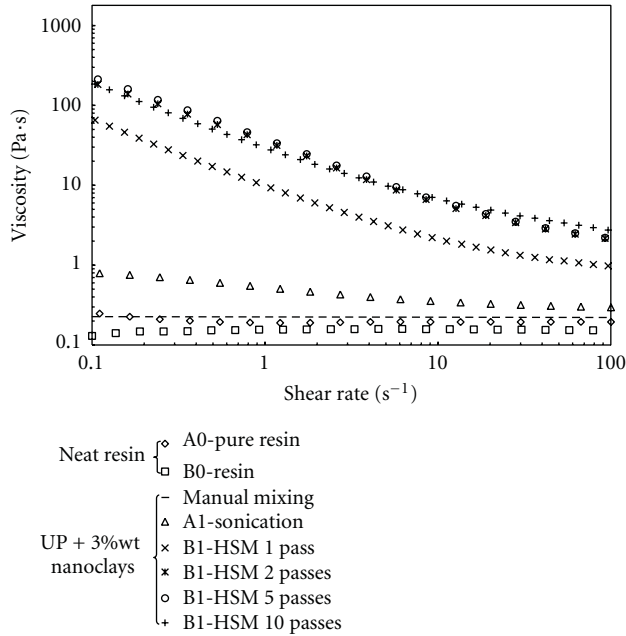


FIGURE 3: Shear viscosity of pure resin and nanocharged resin with 3% wt C30B using different mixing methods.

maximized, and there is no more space for further stacks exfoliation. From these results, it can be concluded that the (B1) high shear mixing technique is more suitable to obtain a potentially exfoliated structure.

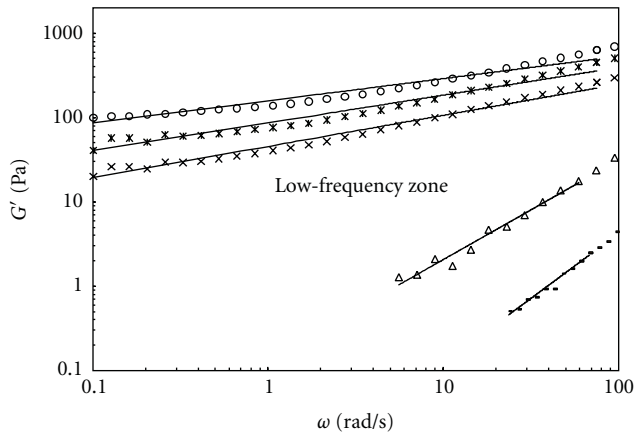
The non-Newtonian behavior of the shear viscosity curves of blends A and B can be attributed to the creation of hydrogen bonds to the oxygen groups on the surface of the C30B clay platelets and the polar groups of the polymer backbone [27]. A steeper decrease of the viscosity slope, observed for the HSM blends, is a sign of an enhanced shear-thinning behavior. According to these results, the dispersion state is probably exfoliated. This behavior may also be due to a loss in local entropy enhancing the movement of the polymer chains in flow direction [8].

Figures 4(a) and 4(b) illustrate the variations in storage moduli G' and damping factor $\tan \delta$ with frequency for the three mixing techniques evaluated on this work. The mixing method has a major impact on the storage modulus, as shown in Figure 4(a) by the differences in G' between the manual, sonication (A1), and high shear mixing (B1). The storage modulus of the manual and (A1) blends show an almost second-order dependency with frequency ($G' \propto \omega^2$), with slopes of 1.541 and 1.131, respectively. This is a typical behaviour of liquid-like blends and can be attributed to a probably intercalated morphology of the nanoclays. As for the high shear mixed blends (B1), G' is quasi-independent of the frequency indicating an almost gel-like structure ($G' \propto \omega^0$) with slopes varying from 0.368 to 0.263 for 1 to 5 passes [3]. This behaviour induces one to believe the formation of a 3D polymer/nanoclays network [6]. Furthermore, the increase of G' with the number of passes in the HSM is a direct consequence of the enhancement of the dispersion of nanoclays which could lead to an exfoliated state. It has

to be noted that no accurate values of G' were detected for frequencies below 0.1 rad/s due to the precision of the rheometer. In Figure 4(b), small variations of $\tan \delta$ for the HSM mixtures at low frequency are observed, which confirms the gel-like structure of these blends. However, these are considered to be weak gels, because the ratio between the dissipative (G'') and elastic energy (G') is low, between 0.1 and 0.7. So the viscous nature still dominates the elastic behaviour in opposite to a strong gel ($\tan \delta$ below 10^{-2}) [35]. At almost $\omega = 10$ rad/s, the $\tan \delta$ value reaches a maximum for the (A1) and manual blends (peak of the bell shape). This marks a transition to a more dissipative behaviour, meaning a transition from a gel-like state to a liquid-like state. This behaviour can be related to the alignment of the platelets in the flow direction. For the (B1) blends, a slight increase of $\tan \delta$ and G' at 10 rad/s can be observed, indicating the beginning of a morphological change. At higher frequencies ($\omega > 62.8$ rad/s), G' seems to tend to the same value for all systems. It was finally found that at high frequencies, the G' response is dominated by the matrix since the values of all mixtures trend to 1000 Pa at 628 rad/s [3].

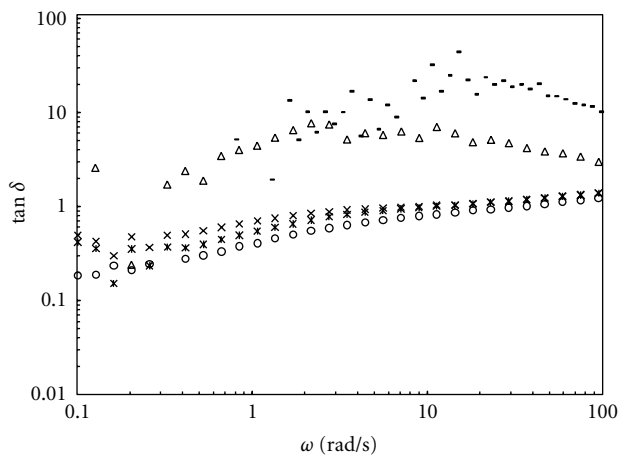
To validate the rheology results showing the differences in dispersion of the nano-platelets, visual observation was performed using SEM and micrographs of the blends as illustrated in Figure 5. Note that the unidirectional etchings on the micrographs are due to the blade of the diamond knife during sample preparation. The manual mixing (Figure 5(a)) shows important agglomerations in the order of 10 microns whereas they are diminishing around 3 microns for sonication (Figure 5(b)). Finally, the high shear mixing seems to be a relevant technique for nano-dispersion showing agglomerates smaller than 1 micron (Figure 5(c)). Figure 6 presents the initial storage modulus as function of the size of the agglomerates obtained after the dispersion by manual mixing, (A1), and (B1) techniques. The first method shows a high level of aggregation compared to the (B1) 5 passes blend which probably has a fully exfoliated morphology. As illustrated by the G' data, there is an increase in elasticity of more than two decades between (A1) and (B1) blends. This is attributed to an important change in the internal structure of the nanoclay platelets and also confirming the gel-like 3D network structure.

3.2. RTM Shear Simulation and Process Limitations. In order to simulate an RTM injection and relate it to the reorganization of the nanoclays with the resin flow, a rheology cycle was imposed to the most viscous (B1) blend that underwent 10 passes through the HSM system. The choice of this particular blend was based on the fact that it is the one showing the most important morphological changes. The imposed shear cycle combines shear and rest periods as illustrated in Figure 7. This simulation is carried out by varying the shear rate three times. At the initial state (quasistatic), the shear rate is kept constant at 0.1 (1/s). The initial shear rate was chosen in order to reproduce the initial static state of the resin before injection. This step is followed by a sudden increase of the shear rate to 1000 s^{-1} representing the resin injection into the mold cavity taking less than 25 seconds.



- Manual mixing, $G' = 0.003\omega^{1.541}$
- △ A1-sonication, $G' = 0.159\omega^{1.131}$
- × B1-HSM 1 pass, $G' = 45.42\omega^{0.368}$
- × B1-HSM 2 passes, $G' = 86.55\omega^{0.327}$
- B1-HSM 5 passes, $G' = 157.7\omega^{0.263}$

(a)



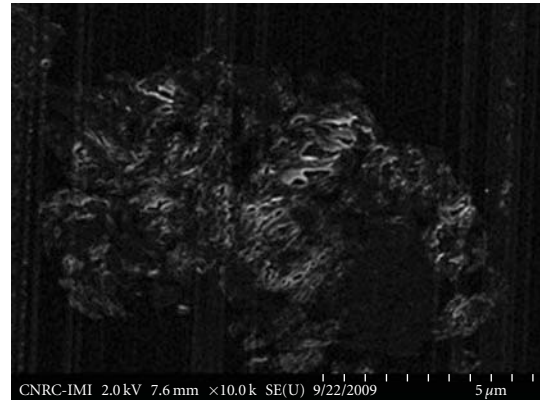
- Manual mixing
- △ A1-sonication
- × B1-HSM 1 pass
- × B1-HSM 2 passes
- B1-HSM 5 passes

(b)

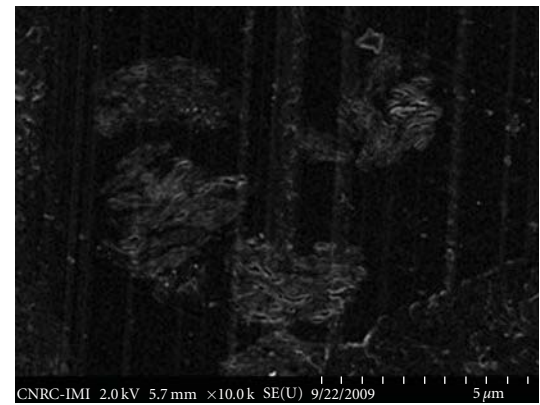
FIGURE 4: Internal structure behavior of UP resin with 3% wt C30B nanoclays for various mixing methods (a) storage modulus of (b) $\tan \delta$.

After this period, the resin is maintained on a static state (i.e., 0.1 (1/s)) for 25 minutes. During this quasistate period at constant shear rate, the resin viscosity increase from 1.8 Pa.s to 200 Pa.s. This increment is assumed to be linked to the nanoclays reorganization, since the shear rate is constant and no chemical reaction takes places (no hardener was added to the resin).

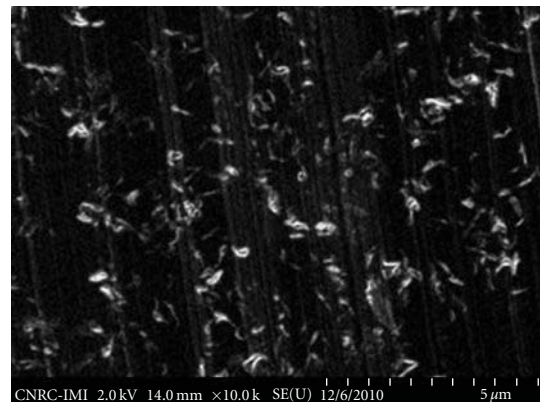
At the very beginning of the cycle, the nanocharged resin is at rest and the initial exfoliated structure of the platelets randomly disorganized. This leads to a very high viscosity of 250 Pa.s on the first two minutes. When the resin is injected at a shear rate of 1000 s^{-1} , the viscosity decreases abruptly



(a)



(b)



(c)

FIGURE 5: SEM micrograph of nanocharged resin with 3% wt C30B using different dispersion methods: (a) manual mixing, (b) A1-sonication, and (c) B1-HSM.

to 1.8 Pa.s and the original nano-structure is destroyed. The particles at this point are oriented in the fluid flow direction. After the filling is completed, at around 3 minutes, the shear is released and the viscosity gradually increases until it reaches its initial value after 10 minutes. There is a restructuration of the nanoparticles in the blend which disorganized themselves to their original exfoliated structure after this period. This rheology simulation gives precious

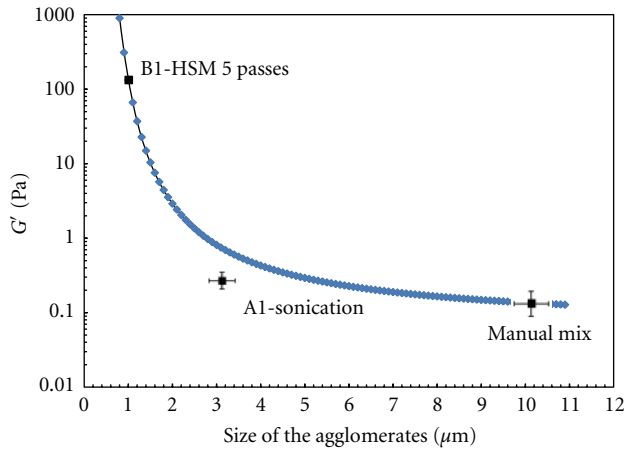


FIGURE 6: Variation of the storage modulus according to the mixing technique.

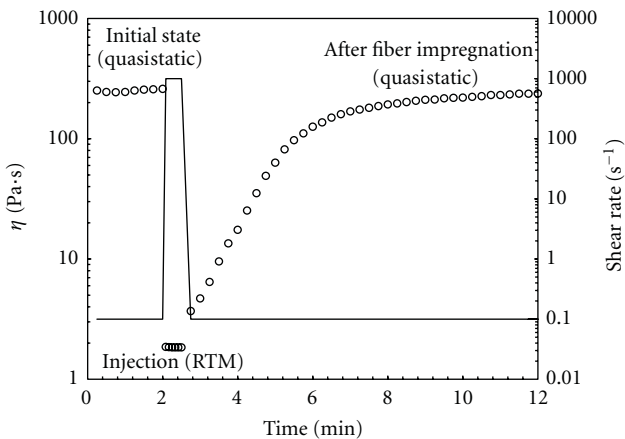


FIGURE 7: RTM injection simulation on the rheometer (B1-HSM 10 passes).

indication about the time necessary for the exfoliated nanoblend to reach a viscosity small enough for injection in addition to its ability to recover rapidly to its original probable exfoliated state which is of interest for the improvement of the properties of the final part.

The gel point is another important feature of the nanocharged mixtures and it is defined as the required time for the covalent bound of the monomer to connect across the network to form the infinite network [15]. At that time, the polymer viscosity tends to infinity. Numerous techniques [19, 34, 36] can be used to determine the gel point, such as the crossing point between the baseline and the tangent drawn from the turning point of G' curve, the cross-over of the modulus G' and G'' , or when the $\tan \delta$ becomes invariant with frequency. The chosen criteria will depend on the system being studied as well as the stoichiometry of the different components. One of the techniques selected in this study was successfully used for epoxy prepregs, consisting in determining the gel time at the maximum of the $\tan \delta$ [36]. It was decided for the gel point study to focus only on the low-frequency range in order to be representative of the

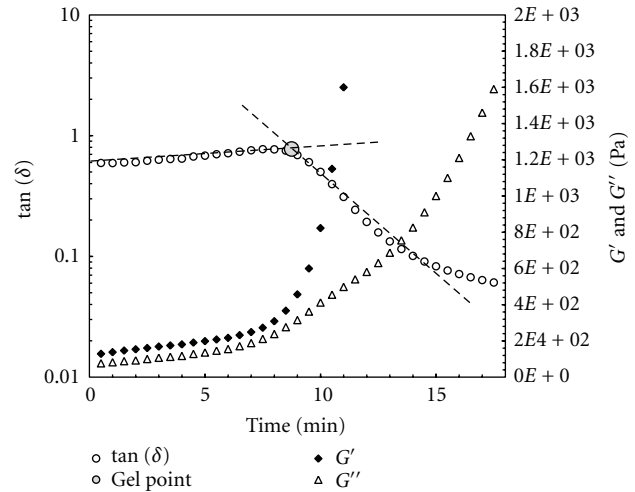


FIGURE 8: Storage and loss moduli and $\tan \delta$ during the cure of B1-HSM 5 passes blend at 23°C.

actual manufacturing process. To obtain consistent results, the frequency of all experiments was set to 1 Hz in the linear viscoelastic region. Experiments were then conducted in time sweep mode as shown in Figures 8 and 9.

Figure 8 illustrates the evolution of G' , G'' , and $\tan \delta$ during the cure of the B1-HSM 5 passes blend at 23°C. It can be seen that G' is always higher than G'' because of the gel-like structure of the blend. As a consequence, no crossover is observed between G' and G'' . At around 9 minutes from the beginning of cure, there is a sudden increase of the storage modulus to infinity which indicates an important change in the polymer structure. At this point, the $\tan \delta$ curve reaches a maximum close to 1. This is an indication of the gel formation which denotes the beginning of the cross-linking of the polymer. The calculation of the gel time with this method was carried out on the resin/nanoparticles blends mixed with different techniques as illustrated in Figure 9(a) at the same temperature and frequency. As shown, the blends mixed with a high shear mixer result in the lowest gel times, between 3 and 15 minutes. Moreover, it is observed that the gel time decreases proportionally with the number of passes in the mixer for the HSM technique. As of the hand mixed and sonicated samples, their gel point is slightly inferior to the pure resin due to the supposed catalytic effect of the nanoclays. Since the nanoclays are not well dispersed with this techniques compared to HSM mixtures, the catalytic effect is limited.

The gelification point is often defined as the time at which the G' exceeds G'' (i.e., $\tan \delta = 1$), but this point corresponds to a high resin viscosity. In LCM process analysis, the processing gel time may be defined as the point at which the resin viscosity curve has a slope of 10% [26]. This criterion results in a viscosity increase between 2 to 5 times from the initial value. At this point the resin will not flow under normal injection pressures [26]. Figure 9(b) illustrates the evolution of the complex viscosity with time during cure. This processing gel time calculated from complex viscosity is in good agreement with the data obtained from

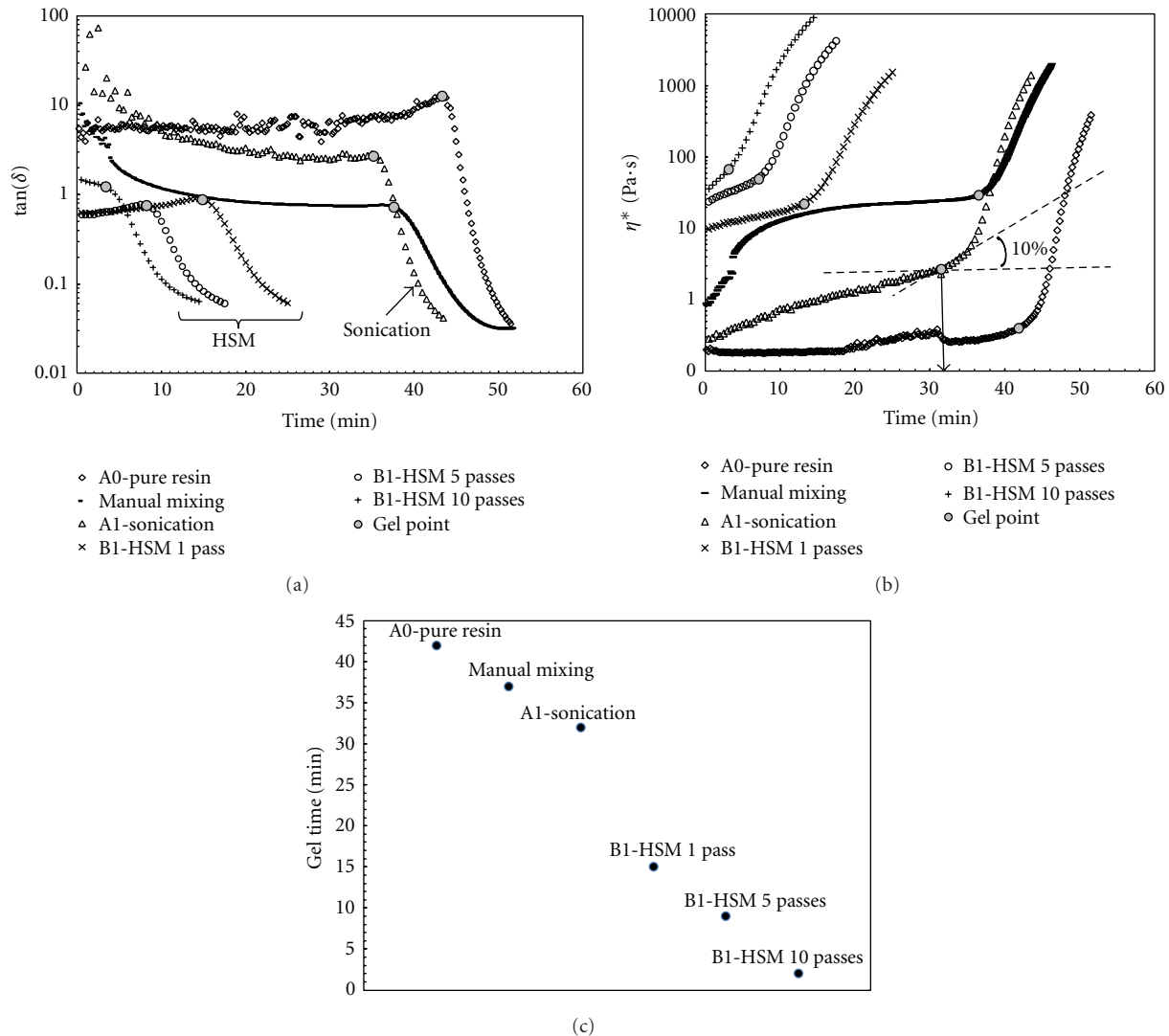


FIGURE 9: Gel time at 23°C UP resin with 3% wt of C30B mixed with various dispersion techniques: (a) method of maximum $\tan \delta$, (b) 10% slope of η^* , and (c) gel point tendency obtained with the maximum $\tan \delta$.

the maximum of $\tan \delta$. The catalytic effect of the nanoclay tends to decrease the gel time due to the increased interactions between nanoclay platelets and the polymer resin. Table 2 resumes the gelification time for each system according to the mixing method. Figure 9(c) summarizes the gelification times calculated from the maximum of $\tan \delta$ according to the mixing method. The gelification time has been reduced in 17 minutes between (A1) and (B1) blends. This is mainly due to an enhanced dispersion state and probable exfoliation, which results in a greater surface for interaction between the polymer matrix and the clays. This interfacial region acts as a catalyst and accelerates the curing reaction.

3.3. Catalytic Effect of the Nanoclays. As illustrated by the gel time results, the addition of nanoclays has a nonnegligible impact on the polymerization process. In order to better understand this catalytic effect on the cross-linking reaction of the UP resin, samples of the different blends were

isothermally maintained at 70°C for various dwell times. The catalyst was then added to the blend and the heat of reaction was analyzed with an M-DSC using a constant heating rate process. The residual heat of reaction was compared to the total heat of reaction generated during the cure of the pure resin. In addition, the samples exposed at 70°C were compared to the samples stored at -18°C, so-called control samples. Neat resin samples were exposed to the same isothermal condition to take into account the styrene evaporation which has an influence on the released heat of reaction. For that reason, a correction of the total heat is made for all stored samples. The nonreleased heat due the evaporation of styrene for the pure resin sample, $\Delta H_{\text{pure resin}}$, during storage at 70°C was calculated as follows:

$$\Delta H_{\text{pure resin}} = H_{\text{pure resin at } -18^\circ\text{C}} - H_{\text{pure resin at } 70^\circ\text{C}}. \quad (8)$$

The evaporation of the cross-linking agent (styrene) during storage lowers the total heat of reaction of the resin a quantity

TABLE 2: Gel time results using two different calculation methods.

			Maximum tan δ (min) Figure 9(a)	10% slope (min) Figure 9(b)
Pure resin			44	42
Manual mixing			38	37
A1-sonication			36	32
3% cloisite 30B	B1 HSM	1 pass	15	14
		5 passes	9	8
		10 passes	3	3

TABLE 3: Storage temperature influence on nanocharged resin using HSM and sonication dispersion techniques.

Isothermal temperature (°C)	Dwell time (h)	Pure resin		Sonication A1		HSM B1-5 passes	
		H_{res} (J/g)	ΔH_{res} (J/g)	H_{res} (J/g)	α_{nano}^1 (%)	H_{res} (J/g)	α_{nano}^1 (%)
-18	24	279.8	—	259.7	6.5	273.1	4.4
	1					224.6	18.4
70	1.5					214.2	21.5
	2					166.7	38.5
	6	260.1	19.7	214.7	14.4		
70	12	243.6	36.2	206.9	15.1		
70	24	239.3	40.5	197.1	17.6		

¹ Calculation based on H_{res} of the corresponding pure resin storage

equals to $\Delta H_{pure\ resin}$. As shown in Table 3, exposing the pure resin at 70°C, for long periods, results in a decrement of the heat of reaction of 9.5% and 14.5% after 6 and 24 hours, respectively. Therefore, for the nanocomposite samples maintained at 70°C, the total heat of reaction has to be compared to the one of the pure resin under similar thermal treatment ($H_{pure\ resin}$ at 70°C). Thus, the degree of cure associated to the catalytic effect of the nanoclays α_{nano} was calculated based on the total heat of reaction generated during cure of the nanocomposites and the one of the pure resin:

$$\alpha_{nano} = 1 - \left(\frac{H_{blend}}{H_{pure\ resin}} \right), \quad (9)$$

where, H_{blend} is the heat of reaction of the nanocharged blend and $H_{pure\ resin}$ the heat of reaction for the pure resin, both at 70°C and at the same dwell time. Figure 10 shows the results of two MDSC tests of the sonicated blend (A1) maintained at -18°C and 70°C during 24 hours. It can be seen that the residual heat of reaction after thermal exposure has decreased by 10% at -18°C and by 17.6% at 70°C. This clearly indicates the influence of the nanoclays on the cure reaction of the unsaturated polyester resin. Table 3 presents the resulting degree of cure α_{nano} after exposing the nanocomposites at these temperatures.

As for the HSM blend (B1), this catalytic effect of nanoclays is very important. The degree of cure α_{nano} reaches 18% after 1 h of exposition and 38.5% after 2 h at 70°C. After this point, the resin gels and it is no longer possible

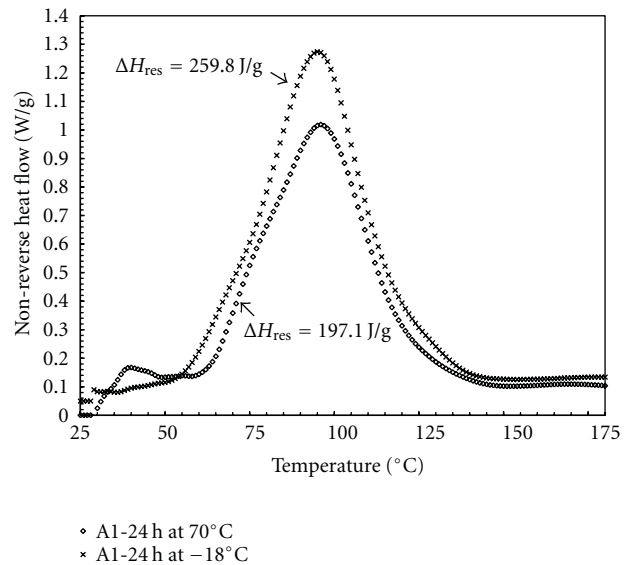


FIGURE 10: Heat of reaction of the sonicated 3% wt C30B nanocharged resin exposed at 70°C and maintained at -18°C in freezer (control) for 24 h. Catalyst added to the mix just before M-DSC analysis.

to be add the catalyst. The differences in cure reaction between the (A1) and (B1) blends can be attributed to an increased dispersion and possible exfoliation of the HSM blend. This catalytic effect of nanoclay platelets is probably

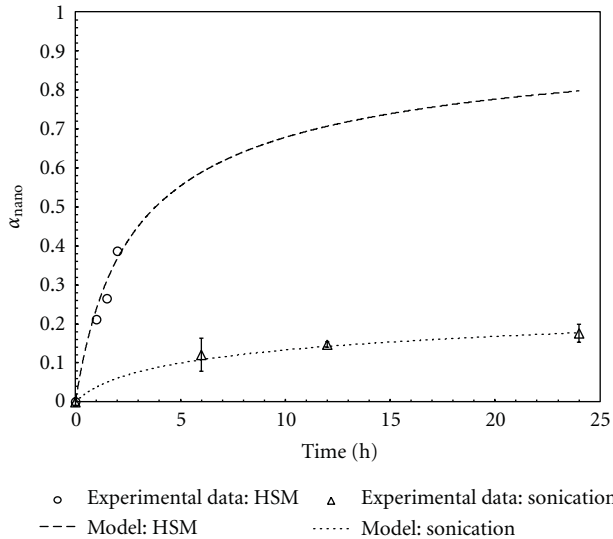


FIGURE 11: Modelling of conversion-time curves for sonicated and HSM blends. Experimental data comes from M-DSC analyses. Fitting curves are polynomial.

due to the existence of attractive forces between the clay and the polymer matrix. The cation-exchange capacity of the nanoclay influences the cure reaction. This acceleration is induced by the alkylammonium ions contained in the surface treatment of the nanocharges [20].

Figure 11 shows the results of the measured degree of cure α_{nano} for (A1) and (B1) blends as a function of exposition time at 70°C. A phenomenological autocatalytic model was used to model the cure reaction of both blends. The degree of cure was evaluated by an n th-order model as follows [26, 34]:

$$\frac{d\alpha}{dt} = K_A \cdot (1 - \alpha)^n, \quad (10)$$

where α is the degree of polymerization, n the reaction order, and K_A the rate constant given by an Arrhenius temperature dependence defined as

$$K_A = K_0 \exp\left(\frac{-E_A}{R \cdot T}\right), \quad (11)$$

where K_0 is the Arrhenius constant, E_A is the activation energy, and R is the ideal gas constant. Equations (10) and (11) are widely used to model the cure of many polymer systems such as polyester and epoxies. This model is used on the assumption that only one kind of reaction may represent the whole cure process [34]. The parameters of the proposed cure kinetics model were obtained by fitting the experimental data extracted from M-DSC tests and presented in Table 3. The coefficients of the two models are shown in Table 4. As illustrated in Figure 11, there is a good agreement between the M-DSC experiments and the proposed models. This indicates that an autocatalytic reaction of the polymer can be started due to the presence of nanoclay particles. Moreover, these results demonstrate that the degree of exfoliation accelerates the autocatalytic cure

TABLE 4: K and m constants of the autocatalytic model for UP resin/nanoclay systems depending on the dispersion method.

$T = 70^\circ\text{C}$	Sonication model	HSM model
K_A (1/min)	0.000875	0.00575
n	16.5	2.7

reaction. It is then concluded that the exfoliation of MMT changes the cure rate of the UP resin tested on this work. Similar results were reported in the past for epoxy resins [37]. This could also indicate that the interfacial region between the clay and the polymer may dominate the properties of the blend.

4. Conclusion

The scope of this work was to study the nanoclays dispersion in an UP resin and by means of three different mixing techniques. Rheology tests based on shear and SAOS experiments revealed the differences between the manual mixing, sonication, and high shear mixing techniques. Notably, the shear thinning behavior is a result of the morphological change of the blend due to the rearrangement of the silicate nanoclays. Furthermore the intercalated and exfoliated structure has shown a gel-like structure of high shear mixed blends. This is, however, a weak gel since $\tan \delta$ is in the order of 10^{-1} . This gel-like structure is a direct consequence of the interaction between the polymer and the nano-platelets leading to the creation of a 3D network in the liquid.

The high shear mixing has the highest elastic modulus (100 Pa) and initial viscosity (up to 250 Pa.s compared to other mixing techniques). However, the viscosity decreases at high shear rate due to the reorientation of the nanoclays. The viscosity reaches 2 Pa.s at high shear which makes it possible to process the blend by RTM. The dispersion was also verified by SEM microscopy showing agglomerates of 10 microns for the manual mixing and less than 1 micron for the high shear technique. The nanoclays seem also to have a catalyst effect on the resin system, showing a reduction of the gel time due to their exfoliation state. The neat resin showed a gel time of 45 minutes whereas the 10 passes HSM blend jellified at around 3 minutes. This phenomenon has to be taken into account for proper composites molding. The DSC study confirms the catalytic effect of the nanoclays showing a degree of cure of 38.5% for the high shear mix after 2 hours of exposition at a 70°C.

This study illustrates how well-dispersed nanoclays in UP resin bring many interesting structural changes in the polymer matrix. This work also shows that processing may be achievable since the time to orient the nanoparticles in the direction of fluid flow is within seconds and the restructuring to their initial random disorganized structure takes few minutes. Future work will focus on the use of HSM technique for manufacturing biocomposite parts improved by nanoclay reinforcing of the bioresin.

Abbreviations

FEG:	Field emission gun (scanning electron microscope)
G' :	Elastic modulus
G'' :	Loss modulus
HSM:	High shear mixing
LCM:	Liquid composite molding
LVE:	Linear viscoelastic
M-DSC:	Modulated differential scanning calorimetry
MMT:	Montmorillonite
phr:	Parts per hundred
RTM:	Resin transfer molding
SCRIMP:	Seeman composite resin infusion molding process
SEM:	Scanning electron microscopy
TEM:	Transmission electronic microscopy
UP:	Unsaturated polyester resin
VARI:	Vacuum assisted resin infusion
% wt:	Weight percentage
XRD:	X-Ray diffraction
ω :	Frequency (rad/s)
$\tan \delta$:	Damping factor.

Acknowledgments

The authors acknowledge the support provided by the Chair of High Performance Composite (CCHP) and the Center for Applied Research on Polymers and Composites (CREPEC). The financial contribution of the Natural Sciences and Engineering Research Council of Canada (NSERC) is also greatly appreciated.

References

- [1] I. Ortega, *Fabrication et caractérisation de nanocomposites a matrice epoxy*, M.S. dissertation, Ecole Polytechnique, Montreal, Canada, 2008.
- [2] S. Abend and G. Lagaly, "Sol-gel transitions of sodium montmorillonite dispersions," *Applied Clay Science*, vol. 16, no. 3-4, pp. 201-227, 2000.
- [3] S. S. Ray and M. Okamoto, "Polymer/layered silicate nanocomposites: a review from preparation to processing," *Progress in Polymer Science*, vol. 28, no. 11, pp. 1539-1641, 2003.
- [4] Y. Rao and T. N. Blanton, "Polymer nanocomposites with a low thermal expansion coefficient," *Macromolecules*, vol. 41, no. 3, pp. 935-941, 2008.
- [5] D. Dean, A. M. Obore, S. Richmond, and E. Nyairo, "Multiscale fiber-reinforced nanocomposites: synthesis, processing and properties," *Composites Science and Technology*, vol. 66, no. 13, pp. 2135-2142, 2006.
- [6] S. S. Ray, "Rheology of polymer/layered silicate nanocomposites," *Journal of Industrial and Engineering Chemistry*, vol. 12, no. 6, pp. 811-842, 2006.
- [7] S. Zainuddin, M. V. Hosur, Y. Zhou, A. Kumar, and S. Jeevani, "Durability study of neat/nanophased GFRP composites subjected to different environmental conditioning," *Materials Science and Engineering A*, vol. 527, no. 13-14, pp. 3091-3099, 2010.
- [8] A. Lele, M. Mackley, G. Galgali, and C. Ramesh, "In situ rheo-x-ray investigation of flow-induced orientation in layered silicate-syndiotactic polypropylene nanocomposite melt," *Journal of Rheology*, vol. 46, no. 5, pp. 1091-1110, 2002.
- [9] C.-K. Lam, K.-T. Lau, H.-Y. Cheung, and H.-Y. Ling, "Effect of ultrasound sonication in nanoclay clusters of nanoclay/epoxy composites," *Materials Letters*, vol. 59, no. 11, pp. 1369-1372, 2005.
- [10] S. Lakshminarayanan, B. Lin, G. A. Gelves, and U. Sundararaj, "Effect of clay surfactant type and clay content on the rheology and morphology of uncured Fluoroelastomer/clay nanocomposites prepared by melt-mixing," *Journal of Applied Polymer Science*, vol. 112, no. 6, pp. 3597-3604, 2009.
- [11] Y. Zhong and S.-Q. Wang, "Exfoliation and yield behavior in nanodispersions of organically modified montmorillonite clay," *Journal of Rheology*, vol. 47, no. 2, pp. 483-495, 2003.
- [12] I. Ortega, C. Billotte, and E. Ruiz, "Thermo-mechanical and rheological characterization of various epoxy-based nanocomposites for high performance composites," in *Proceedings of the 4th International Symposium on Polymer Nanocomposites Science and Technology*, Quebec, Canada, 2007.
- [13] J. Ren, B. F. Casanueva, C. A. Mitchell, and R. Krishnamoorti, "Disorientation kinetics of aligned polymer layered silicate nanocomposites," *Macromolecules*, vol. 36, no. 11, pp. 4188-4194, 2003.
- [14] R. Krishnamoorti, J. Ren, and A. S. Silva, "Shear response of layered silicate nanocomposites," *Journal of Chemical Physics*, vol. 114, no. 11, pp. 4968-4973, 2001.
- [15] C. Mobuchon, P. J. Carreau, and M.-C. Heuzey, "Structural analysis of non-aqueous layered silicate suspensions subjected to shear flow," *Journal of Rheology*, vol. 53, no. 5, pp. 1025-1048, 2009.
- [16] R. Prasad, V. Pasanovic-Zujo, R. K. Gupta, F. Cser, and S. N. Bhattacharya, "Morphology of EVA based nanocomposites under shear and extensional flow," *Polymer Engineering & Science*, vol. 44, no. 7, pp. 1220-1230, 2004.
- [17] J. Ren, A. S. Silva, and R. Krishnamoorti, "Linear viscoelasticity of disordered polystyrene-polyisoprene block copolymer based layered-silicate nanocomposites," *Macromolecules*, vol. 33, no. 10, pp. 3739-3746, 2000.
- [18] R. Krishnamoorti and K. Yurekli, "Rheology of polymer layered silicate nanocomposites," *Current Opinion in Colloid and Interface Science*, vol. 6, no. 5-6, pp. 464-470, 2001.
- [19] E. Ruiz and C. Billotte, "Predicting the cure of thermosetting polymers: the isoconversion map," *Polymer Composites*, vol. 30, no. 10, pp. 1450-1457, 2009.
- [20] O. Becker, Y.-B. Cheng, R. J. Varley, and G. P. Simon, "Layered silicate nanocomposites based on various high-functionality epoxy resins: the influence of cure temperature on morphology, mechanical properties, and free volume," *Macromolecules*, vol. 36, no. 5, pp. 1616-1625, 2003.
- [21] B. Gholizadeh, A. Arefazar, and J. Barzin, "Polycarbonate/polyamide 6/nanoclay ternary nanocomposite membranes: preparation, characterisation, and gas separation properties," *Polymers and Polymer Composites*, vol. 17, no. 3, pp. 181-187, 2009.
- [22] D. H. Yu, B. Wang, Y. Feng, and Z. P. Fang, "Investigation of free volume, interfacial, and toughening behavior for cyanate ester/bentonite nanocomposites by positron annihilation," *Journal of Applied Polymer Science*, vol. 102, no. 2, pp. 1509-1515, 2006.
- [23] G. Choudalakis, A. D. Gotsis, H. Schut, and S. J. Picken, "The free volume in acrylic resin/laponite nanocomposite coatings," *European Polymer Journal*, vol. 47, no. 3, pp. 264-272, 2011.
- [24] F. Roman, S. Montserrat, and J. M. Hutchinson, "On the effect of montmorillonite in the curing reaction of epoxy

- nanocomposites,” *Journal of Thermal Analysis and Calorimetry*, vol. 87, no. 1, pp. 113–118, 2007.
- [25] E. Ruiz and F. Trochu, “Multi-criteria thermal optimization in liquid composite molding to reduce processing stresses and cycle time,” *Composites Part A*, vol. 37, no. 6, pp. 913–924, 2006.
- [26] E. Ruiz, F. Waffo, J. Owens, C. Billotte, and F. Trochu, “Modeling of resin cure kinetics for molding cycle optimization,” in *Proceedings of the International Conference in Flow Processes in Composite Materials (FPCM '06)*, Ecole des Mines de Douai, Douai, France, 2006.
- [27] W. K. Goertzen, X. Sheng, M. Akinc, and M. R. Kessler, “Rheology and curing kinetics of fumed silica/cyanate ester nanocomposites,” *Polymer Engineering & Science*, vol. 48, no. 5, pp. 875–883, 2008.
- [28] K. C. Cole, J. J. Hechler, and D. Noel, “A new approach to modeling the cure kinetics of epoxy amine thermosetting resins. 2. Application to a typical system based on bis[4-(diglycidylamino)phenyl]methane and bis(4-aminophenyl)sulfone,” *Macromolecules*, vol. 24, no. 11, pp. 3098–3110, 1991.
- [29] T. Lan, P. D. Kaviratna, and T. J. Pinnavaia, “Epoxy self-polymerization in smectite clays,” *Journal of Physics and Chemistry of Solids*, vol. 57, no. 6–8, pp. 1005–1010, 1996.
- [30] L. Botta, R. Scaffaro, F. P. L. A. Mantia, and N. T. Dintcheva, “Effect of different matrices and nanofillers on the rheological behavior of polymer-clay nanocomposites,” *Journal of Polymer Science, Part B*, vol. 48, no. 3, pp. 344–355, 2010.
- [31] F. Bensadoun, N. Kchit, C. Billotte, S. Bickerton, F. Trochu, and E. Ruiz, “A study of nanoclay reinforcement of bio-composites made by liquid composite molding,” *International Journal of Polymer Science*, vol. 2011, Article ID 964193, 10 pages, 2011.
- [32] C. H. Dan, M. H. Lee, Y. D. Kim, B. H. Min, and J. H. Kim, “Effect of clay modifiers on the morphology and physical properties of thermoplastic polyurethane/clay nanocomposites,” *Polymer*, vol. 47, no. 19, pp. 6718–6730, 2006.
- [33] F. A. Morrison, *Understanding Rheology*, Oxford University Press, New York, NY, USA, 2001.
- [34] E. Ruiz and F. Trochu, “Thermomechanical properties during cure of glass-polyester RTM composites: elastic and viscoelastic modeling,” *Journal of Composite Materials*, vol. 39, no. 10, pp. 881–916, 2005.
- [35] M. Hamdine, M.-C. Heuzey, and A. Bégin, “Effect of organic and inorganic acids on concentrated chitosan solutions and gels,” *International Journal of Biological Macromolecules*, vol. 37, no. 3, pp. 134–142, 2005.
- [36] M. Hayaty, M. H. Beheshty, and M. Esfandeh, “A new approach for determination of gel time of a glass/epoxy prepreg,” *Journal of Applied Polymer Science*, vol. 120, no. 3, pp. 1483–1489, 2011.
- [37] W.-B. Xu, S.-P. Bao, S.-J. Shen, G.-P. Hang, and P.-S. He, “Curing kinetics of epoxy resin-imidazole-organic montmorillonite nanocomposites determined by differential scanning calorimetry,” *Journal of Applied Polymer Science*, vol. 88, no. 13, pp. 2932–2941, 2003.

Research Article

Thermal Behavior with Mechanical Property of Fluorinated Silane Functionalized Superhydrophobic Pullulan/Poly(vinyl alcohol) Blends by Electrospinning Method

Mohammad Rezaul Karim¹ and Md. Shahidul Islam²

¹Center of Excellence for Research in Engineering Materials, College of Engineering, King Saud University, Riyadh 11421, Saudi Arabia

²Department of Applied Chemistry and Chemical Engineering, University of Dhaka, Dhaka 1000, Bangladesh

Correspondence should be addressed to Mohammad Rezaul Karim, mkarim@ksu.edu.sa

Received 14 June 2011; Accepted 19 August 2011

Academic Editor: Gaurav Mago

Copyright © 2011 M. R. Karim and Md. S. Islam. This is an open access article distributed under the Creative Commons Attribution License, which permits unrestricted use, distribution, and reproduction in any medium, provided the original work is properly cited.

Fluorinated silane functionalized superhydrophobic pullulan/poly(vinyl alcohol) (PULL/PVA) blend membrane with water contact angle larger than 150° has been prepared by the electrospinning method. The morphology, thermal stability, and mechanical property of the membranes are characterized using scanning electron microscopy (SEM), thermogravimetric analysis (TGA), and ZWICK materials testing machine, respectively. Interactions between PULL and PVA and PULL/PVA blends with perfluorooctyltriethoxysilane (PFOTES) of the membranes are analyzed using differential scanning calorimetry (DSC) and Fourier transform infrared (FTIR). Contact angles and water drops on the surface of the membrane are measured by video microscopy. The study shows that the addition of minor quantity of PVA with PULL results in improvement in thermal stability and mechanical property (tensile strength) of the PULL membranes.

1. Introduction

The wettability of a solid surface is an interesting property of a material and is described as the contact angle between a liquid and a solid surface. When the contact angle between water and a solid surface is larger than 150° , this solid surface is called a superhydrophobic surface [1]. Superhydrophobic surfaces are widely found in nature. For example, the surface of a lotus leaf is observed to be an array of nanoscale buds [2]. Water drops on the surface of the leaf tend to slide down, rendering its self-cleaning property. The surfaces which mimic “lotus effect” have triggered extensive interests for their potential applications involving water repellency, self-cleaning, and antifouling properties [3–6]. Generally, the hydrophobicity of surfaces depends on both their chemical composition and surface geometrical structure [7]. In terms of chemical composition, hydrophobicity can only be increased by introducing a component with low surface energy such as fluorinated methyl groups. However, this method to increase hydrophobicity is limited.

The maximum contact angle that can be reached by coating fluorinated methyl groups onto a flat solid surface is only 120° , which can be hardly called superhydrophobic [8]. Therefore, a hierarchical structure is introduced into the solid surface to achieve superhydrophobicity. A number of methods have been used to make a hierarchical superhydrophobic surface including phase separation [9], electrochemical deposition [10], chemical vapor deposition [11], crystallization control [12], photolithography [13], assembly [14], sol-gel methods [15], solution-immersion methods [16], and array of nanotubes/nanofibers [17, 18].

Electrospinning is a simple but versatile method to produce continuous fibers with diameters ranging from nanometer to submicron scale. Superhydrophobic surfaces can be obtained through this process by controlling the surface roughness under appropriate conditions [19, 20]. Superhydrophobic polystyrene nanofibers were electrospun by either using various solvents [8] or adding room temperature ionic liquid [21]. Cellulose triacetate fibrous mat [22] and poly(3-hydroxybutyrate-co-3-hydroxyvalerate) (PHBV)

fibrous surfaces [23] are fabricated using electrospun fibers followed with plasma treatment. Electrospun nanofibers from the blending solution of fully hydrolyzed medium molecular weight poly(vinyl alcohol) and high-molecular-weight poly(vinyl alcohol) with montmorillonite were fabricated [24].

Pullulan is a natural polymer with excellent biocompatibility. The use of natural polymer has created tremendous interest recently, for example, as proteins in biotechnological materials and biomedical applications [25]. However, only few reports are available in the literature regarding superhydrophobic PULL membrane prepared by electrospinning. Pullulan's solubility can be controlled or provided with reactive groups by chemical derivatization. Due to its excellent properties, pullulan is used as a low-calorie ingredient in foods, gelling agent, coating and packaging material for food and drugs, binder for fertilizers, and as an oxidation-prevention agent for tablets. Other applications include contact lenses manufacturing, biodegradable foil, plywood, water solubility enhancer, and for enhancing oil recovery [26–29].

Poly(vinyl alcohol) (PVA) is a semicrystalline hydrophilic polymer with good chemical and thermal stability. It is a highly biocompatible and nontoxic polymer and it can be processed easily; it also has high water permeability. PVA can form physical gels in various types of solvents which lead to the use of PVA in a wide range of applications in medical, cosmetic, food, pharmaceutical, and packaging industries [30–36].

Polymer blending constitutes a very useful method for the improvement or modification of the physicochemical properties of polymeric materials. An important property of a polymer blend is the miscibility of its components because it affects the mechanical properties, the morphology, and the permeability and degradation. Polymer blends are physical mixtures of structurally different polymers or copolymers that interact with secondary forces with no covalent bonding [37], such as hydrogen bonding, dipole-dipole forces, and charge-transfer complexes for homopolymer mixtures [38–40].

In our previous report, we prepared fluorinated silane functionalized pullulan superhydrophobic membrane using electrospinning technique [41]. In this study, fluorinated silane functionalized superhydrophobic PULL/PVA blend membranes are made to enhance the thermal stability and mechanical property (tensile strength) of PULL membranes by applying the same technique.

2. Experimental

2.1. Materials. Pullulan is a food grade preparation (PF-20 grade) from Hayashibara Biochemical Laboratories Inc. (Okayama, Japan), PVA with $P_n = 1,700$ (fully hydrolyzed, degree of saponification = 99.9%) was obtained from DC Chemical, Seoul, Republic of Korea and perfluorooctyltriethoxysilane (PFOTES) is purchased from Aldrich Chemical Company. Doubly distilled water is used as a solvent to prepare all solutions.

2.2. Preparation of PULL/PVA/PFOTES Blend Solutions. The PULL/PVA solutions (total polymer concentrations are 9 and 12 wt.%) with 80/20 mass ratio were prepared in doubly distilled water at 80°C temperature under magnetic stirring for 2–3 h. The PULL/PVA/PFOTES blend solutions were prepared by mixing of the PULL/PVA solutions with 1 wt.% of PFOTES with gently stirred for further 24 h. The formed solutions were then used for the preparation of membranes using electrospinning technique.

2.3. Membrane Preparation by Electrospinning. During electrospinning, each solution was continuously supplied using a syringe pump with a speed of 0.04 mL/h through a 25G needle producing a Taylor cone. A high power voltage (15 kV) was supplied to the solution with a tip-to-collector distance of 15 cm. Membranes were collected on electrically grounded aluminum foil placed at a vertical distance to the needle tip. Trace amount of PFOTES does not affect the electrospinnability of PULL/PVA blend solution.

2.4. Characterization of Membranes. The water contact angles of the membranes were measured using video microscopy. Using a microsyringe, 5 μ L deionized water was dropped perpendicularly to each surface of the membranes placed on a horizontal glass sheet. Then, the images of water drops on the surface of the membranes were observed using Scalar Video Loupe (VL-11s) and analyzed using the Sigma TV II program. Membranes were also characterized with FTIR (IFS 120HR, Bruker) and DSC (model Q-10) from TA instruments, USA. The morphology, thermal stability, and mechanical property (tensile strength) of membranes were observed with a field-emission scanning electron microscope (JEOL, model JSM-6380) after gold coating, TGA technique (model Q-50; TA Instruments, USA), and ZWICK Z005 (ZWICK materials testing machine, Germany), respectively.

3. Results and Discussion

3.1. DSC Data of Membranes. Figure 1 illustrates the DSC thermograms of pure PULL, PVA, and electrospun PULL/PVA blend membrane with 80/20 mass ratio at a total polymer concentration of 9 wt.%. A relatively large and sharp endothermic peak is observed at about 224°C (Figure 1(a)) and is assigned to the melting temperature of pure PVA, which has a number-average degree of polymerization of 1700, which agrees very well with reported data [42]. This peak is shifted to 206.50°C with the addition of 80 wt.% PULL (Figure 1(b)), and this shifts the melting temperature to lower value; this occurred because of the addition of PULL whose melting temperature changes from 95 to 84°C (Figure 1(b)). This is because the majority of the chains are in a noncrystalline state due to the rapid solidification process of stretched chains during electrospinning. Pure PULL shows a large thermogram peak of melting transition (T_m) at 95°C (Figure 1(c)).

The interactions between PULL/PVA blending and PFOTES of membranes are investigated by DSC. Figure 2 shows the DSC thermogram of PULL/PVA/PFOTES blend membrane with 1 wt.% of PFOTES contents and 80/20 mass

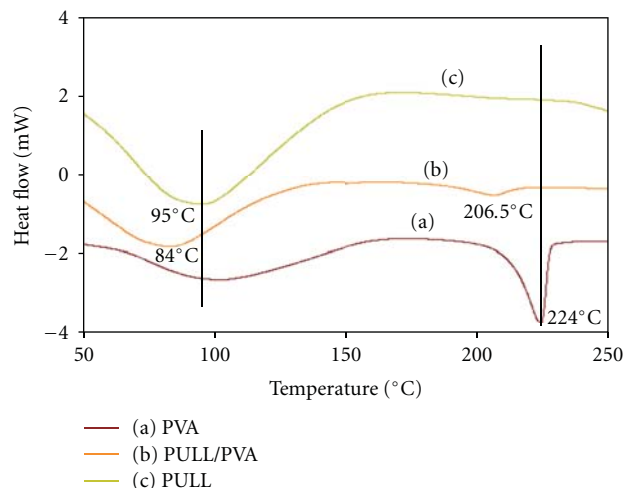


FIGURE 1: DSC data of (a) PVA, (b) PULL/PVA blend membrane using electrospinning method (Applied voltage = 15 kV, TCD = 15 cm, Blend ratio (PULL/PVA) = 80/20, and Total polymer concentration = 9 wt.%), and (c) PULL.

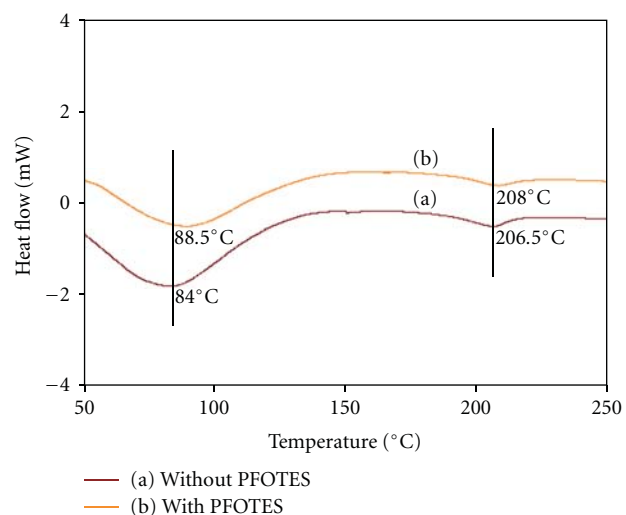


FIGURE 2: DSC data of PULL/PVA blend membranes (a) without PFOTES, and (b) with PFOTES using electrospinning method (Applied voltage = 15 kV, TCD = 15 cm, Blend ratio (PULL/PVA) = 80/20, and Total polymer concentration = 9 wt.%).

ratio of those two polymers at a total polymer concentration of 9 wt.%. Without PFOTES, PULL/PVA membrane shows two thermogram peaks of melting transitions (T_m) at 84°C, and 206.50°C (Figure 2(a)). These peaks are shifted to 88.5°C and 208°C with the addition of 1 wt.% PFOTES (Figure 2(b)). The DSC thermograms for the membranes show clearly the melting transitions of the PULL/PVA blend membrane, in which there are significant effects of the PFOTES content. The dramatic changes of T_m of the composite membranes can be attributed by the introduction of CF_3 groups into heteroatom (O atom) containing hydrophobic carbon ring of PULL and hydrophobic carbon chain of PVA.

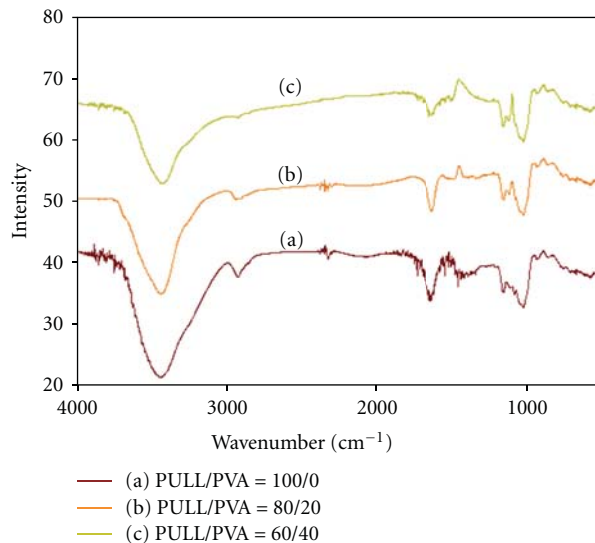


FIGURE 3: FTIR data of PULL/PVA blend membrane with various weight ratios of (a) 100/0, (b) 80/20, and (c) 60/40 using electrospinning method (Applied voltage = 15 kV, TCD = 15 cm, and Total polymer concentration = 9 wt.%).

3.2. FTIR Data of Membranes. FTIR spectra give information about the structure of blend membranes studied. In Figure 3, examples of spectra of pure PULL and PULL/PVA blend membranes at 500–4000 cm^{-1} range are shown. Pure PULL membrane exhibits identical bands as shown in Figure 3(a). Strong absorption in 850 cm^{-1} is characteristic of the α -glucopyranoside units. Absorption in 755 cm^{-1} indicates the presence of α -(1,4) glucosidic bonds, and spectra in 932 cm^{-1} proves the presence of α -(1,6) glucosidic bonds. Besides, in the areas for reference and evaluated samples the frequencies are analogous [43]. Bands at 2850–3000 cm^{-1} are due to stretching vibrations of CH and CH_2 groups and bands attribute to CH/CH_2 deformation vibrations are present at 1300–1500 cm^{-1} range. Also very intensive, broad hydroxyl band occurs at 3000–3600 cm^{-1} and accompanying C–O stretching exists at 1000–1260 cm^{-1} . With the addition of PVA, some absorption peaks of PULL become lower in intensity, whereas some absorption peaks at 1096 and 1447 cm^{-1} appear and the intensity of these peaks increases with augmenting the concentration of PVA (Figures 3(b) and 3(c)). This suggests that hydrogen bonds between hydroxyl groups in PULL and hydroxyl groups in PVA could possibly play a role in the shift of the peaks. Thus, the FTIR spectroscopy supports the interactions between PULL and PVA, which are suggested above. Moreover, the absorption peaks which appeared at 1145 cm^{-1} , 1235 cm^{-1} , and 1430 cm^{-1} are attributed to the vibrations of CF_2 and CF_3 groups in PFOTES and the absorption peaks at 700–800 cm^{-1} are due to the vibration of Si–O groups in the silanes (Figure 4(b)). Thus, the FTIR spectroscopy supplies also evidences of possible interactions between PULL/PVA blend and PFOTES, which are suggested by DSC.

3.3. TGA Data of Membranes. Thermal stability of PULL/PVA membranes is measured using TGA in nitrogen

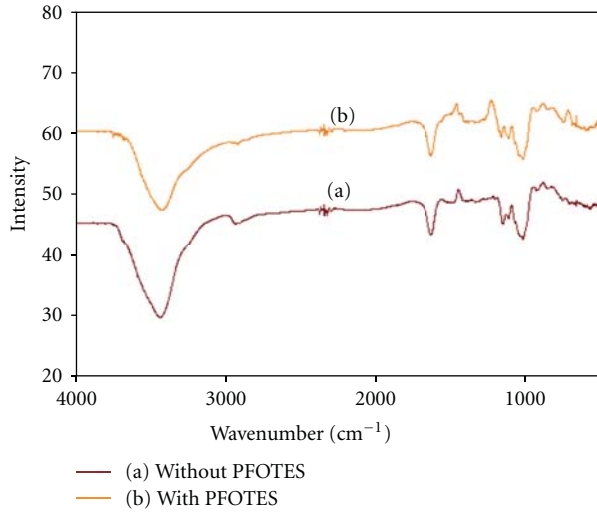


FIGURE 4: FTIR data of PULL/PVA blend membranes (a) without PFOTES, and (b) with PFOTES using electrospinning method (applied voltage = 15 kV, TCD = 15 cm, blend ratio (PULL/PVA) = 80/20, and total polymer concentration = 9 wt.%).

TABLE 1: Tensile strength of PULL/PVA blend membranes as a function of PVA contents using electrospinning method (applied voltage = 15 kV, TCD = 15 cm, and total polymer concentration = 9 wt.%).

PVA content (wt.%)	Tensile strength (MPa)
0	5.12 ± 0.25
5	5.27 ± 0.25
10	5.42 ± 0.25
15	5.54 ± 0.25
20	5.65 ± 0.25

atmosphere. Figure 5 shows TGA thermograms of different decomposition temperature with PULL/PVA mass ratios of 100/0, and 80/20. The below curve of the TGA data (Figure 5(a)) represents the pure PULL membrane and the upper curve (Figure 5(b)) is for 80/20 blend ratio of PULL/PVA. Clearly, it can be seen that higher thermal stability of the membranes could be with the addition of PVA in the PULL/PVA blend system.

3.4. Tensile Strength. Some of the fascination with the behavior of polymers comes from the large changes in the physical properties and the wide range of mechanical behaviours [44]. The tensile strength of the PULL/PVA blend membranes increases with augmenting the weight percentage of PVA, as shown in Table 1.

3.5. Water Contact Angles of Membranes. Membranes prepared by electrospinning method have much higher contact angle because of the high surface area of the formed fibers that ranges from nanometer to submicron scale. As shown in Figure 6(a), nanofibers electrospun using total polymer concentration 9 wt.% contain a large number of beads in nanometer size (500–1000 nm), whereas less number of beads containing nanofibers can be electrospun using total

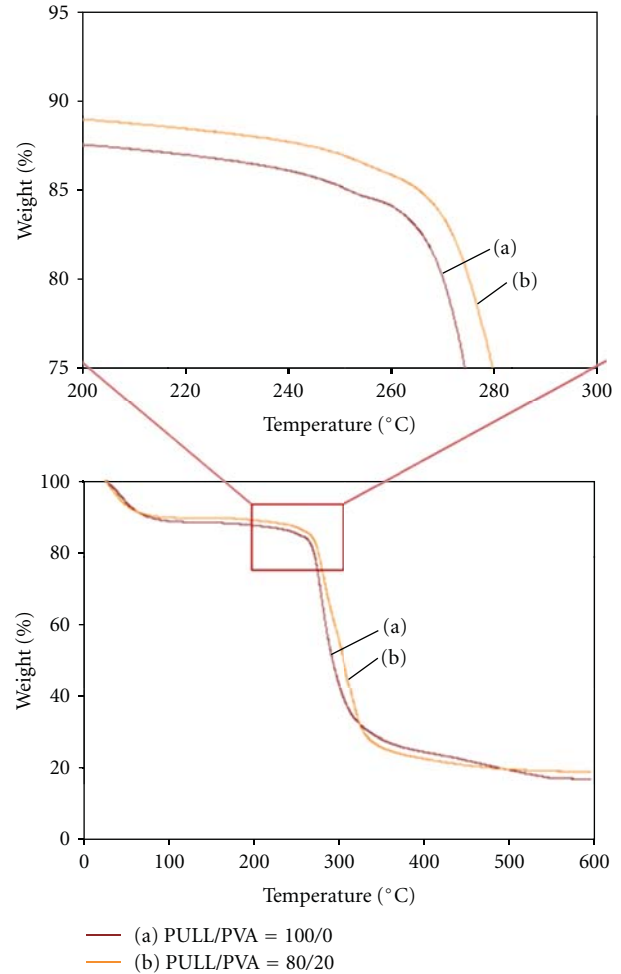


FIGURE 5: TGA data of PULL/PVA blend membrane with weight ratios of (a) 100/0 and (b) 80/20 using electrospinning method (applied voltage = 15 kV, TCD = 15 cm, and total polymer concentration = 9 wt.%).

polymer concentration of 12 wt.%, and 9 wt.% and 12 wt.% of total polymer concentrations coupled with PFOTES applying the same parameters as shown in Figures 6(b), 6(c), and 6(d), respectively. The obtained nanofibers are ranged from 200 to 800 nm. The reason for different bead contents in each concentration is that the Rayleigh forces, which assist in bead formation, are able to overcome the viscous forces to enable the formation of beads [45]. Moreover, strong interaction between PULL/PVA blends and PFOTES is attributed to the formation of less number of beads in the fibers. The interaction between PULL/PVA blends and PFOTES can be put forward as a cause to two factors.

First, the introduction of hydrophobic CF_3 groups on the heteroatom (O atom) containing hydrophobic carbon ring of PULL and hydrophobic carbon chain of PVA and the second factor is the interaction obtained from the formation of hydrogen bonding between polar hydrogen of $-\text{OH}$ group of PULL and PVA with O of PFOTES. Although contact angles of up to 147° (Figure 6(a)) and 142° (Figure 6(b)) can be reached by directly electrospinning of 9 wt.% and 12 wt.%

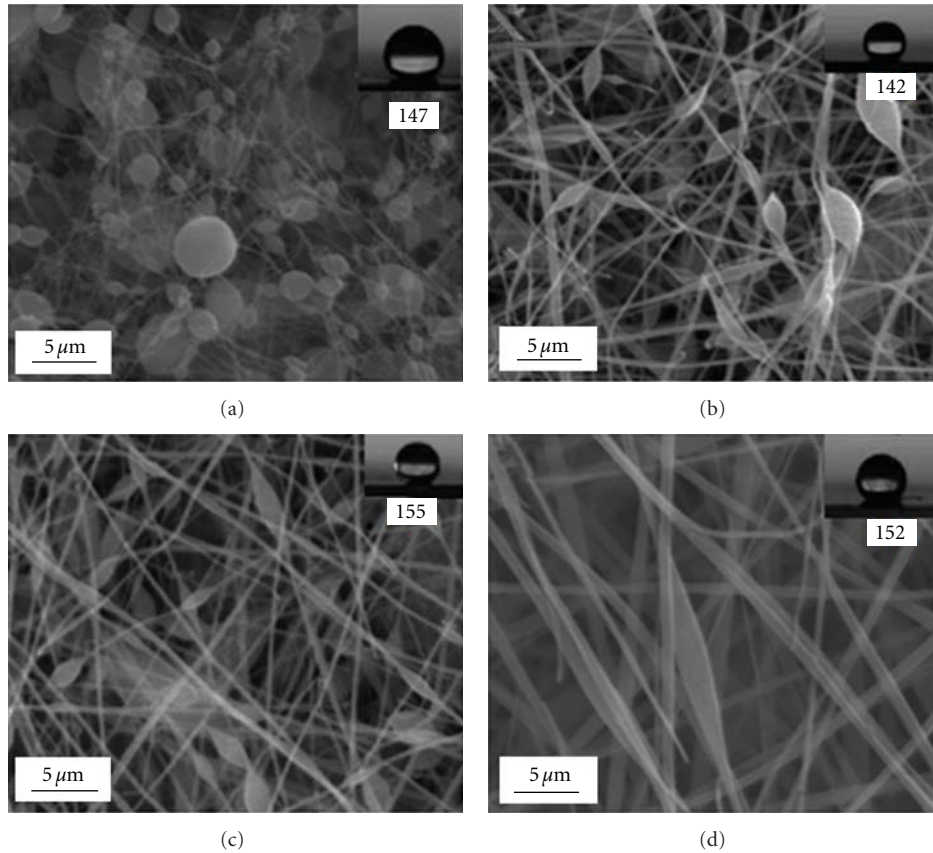


FIGURE 6: SEM images of membranes prepared from PULL/PVA blend solutions of total polymer concentrations of (a) 9 wt.%, (b) 12 wt.%, (c) 9 wt.% with PFOTES, (d) 12 wt.% with PFOTES using electrospinning method (applied voltage = 15 kV, TCD = 15 cm, blend ratio (PULL/PVA) = 80/20).

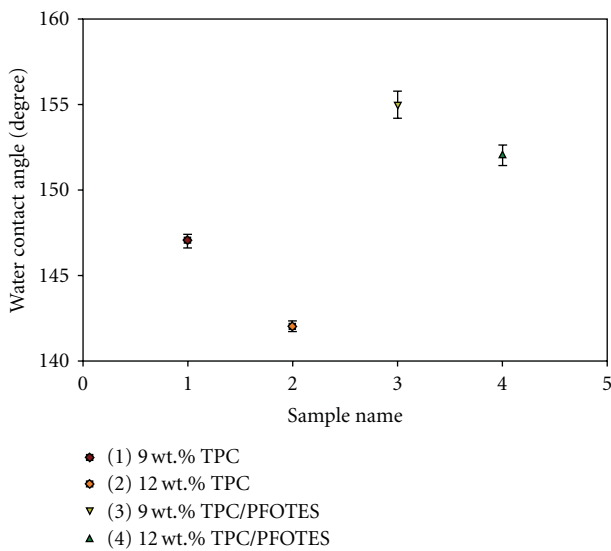


FIGURE 7: Variation of water contact angle with different compositions of PULL/PVA blend polymers of (1) 9 wt.% total polymer concentration (TPC), (2) 12 wt.% total polymer concentration (TPC), (3) 9 wt.% TPC with PFOTES, and (4) 12 wt.% TPC with PFOTES (blend ratio, PULL/PVA = 80/20).

TABLE 2: Water contact angles of the prepared membranes.

Samples	PULL/PVA blend ratio (by wt.%)	Water contact angles
9 wt.% TPC	80/20	147 ± 0.25
12 wt.% TPC		142 ± 0.15
9 wt.% TPC/PFOTES		155 ± 1.0
12 wt.% TPC/PFOTES		152 ± 0.5

TPC: total polymer concentration.

of total polymer concentration solutions, respectively, the membranes can not still be considered as superhydrophobic membranes. Therefore, 9 wt.% and 12 wt.% of total polymer concentration solutions coupled with PFOTES are used to successfully prepare superhydrophobic membranes with high-contact angles of 155° (Figure 6(c)) and 152° (Figure 6(d)), respectively. Water contact angles of all samples taken in this experiment are shown in Figure 7 (data are given in Table 2). Higher contact angle of 9 wt.% of total polymer concentration than that of 12 wt.% total polymer concentration can be explained on the basis of surface roughness like lotus leaf [2] due to the more bead formation in case of 9 wt.%.

4. Conclusions

Superhydrophobic PULL/PVA membranes are prepared by electrospinning from fluorinated silane functionalized PULL/PVA blends. It is observed that both of 9 wt.% and 12 wt.% of total polymer concentration membranes can only reach contact angles lower than 150° by electrospinning of PULL/PVA blends without using PFOTES. Superhydrophobic membranes with contact angles of up to 155° and 152° can be achieved by electrospinning of 9 wt.% and 12 wt.% of total polymer concentration solutions coupled with fluorinated silane, respectively. Moreover, thermal stability and mechanical property of the PULL membranes has been enhanced with the introduction of PVA.

Acknowledgment

This project was supported by King Saud University, Deanship of Scientific Research, College of Engineering Research Center.

References

- [1] X. Feng and L. Jiang, "Design and creation of superwetting/antiwetting surfaces," *Advanced Materials*, vol. 18, no. 23, pp. 3063–3078, 2006.
- [2] W. Barthlott and C. Neinhuis, "Purity of the sacred lotus, or escape from contamination in biological surfaces," *Planta*, vol. 202, no. 1, pp. 1–8, 1997.
- [3] L. Feng, S. Li, Y. Li et al., "Super-hydrophobic surfaces: from natural to artificial," *Advanced Materials*, vol. 14, no. 24, pp. 1857–1860, 2002.
- [4] A. Lafuma and D. Quere, "Superhydrophobic states," *Nature Materials*, vol. 2, no. 7, pp. 457–460, 2003.
- [5] R. Blossey, "Self-cleaning surfaces—Virtual realities," *Nature Materials*, vol. 2, no. 5, pp. 301–306, 2003.
- [6] H. Y. Erbil, A. L. Demirel, Y. Avci, and O. Mert, "Transformation of a simple plastic into a superhydrophobic surface," *Science*, vol. 299, no. 5611, pp. 1377–1380, 2003.
- [7] D. Quééré, "Rough ideas on wetting," *Physica A*, vol. 313, no. 1-2, pp. 32–46, 2002.
- [8] M. Kang, R. Jung, H. S. Kim, and H. J. Jin, "Preparation of superhydrophobic polystyrene membranes by electrospinning," *Colloids and Surfaces A*, vol. 313-314, pp. 411–414, 2008.
- [9] J. T. Han, X. Xu, and K. Cho, "Diverse access to artificial superhydrophobic surfaces using block copolymers," *Langmuir*, vol. 21, no. 15, pp. 6662–6665, 2005.
- [10] M. Li, J. Zhai, H. Liu, Y. Song, L. Jiang, and D. Zhu, "Electrochemical deposition of conductive superhydrophobic zinc oxide thin films," *Journal of Physical Chemistry B*, vol. 107, no. 37, pp. 9954–9957, 2003.
- [11] H. Liu, L. Feng, J. Zhai, L. Jiang, and D. Zhu, "Reversible wettability of a chemical vapor deposition prepared ZnO film between superhydrophobicity and superhydrophilicity," *Langmuir*, vol. 20, no. 14, pp. 5659–5661, 2004.
- [12] T. Onda, S. Shibuichi, N. Satoh, and K. Tsujii, "Super-water-repellent fractal surfaces," *Langmuir*, vol. 12, no. 9, p. 2125, 1996.
- [13] T. J. McCarthy and D. Oner, "Ultrasuperhydrophobic surfaces. Effects of topography length scales on wettability," *Langmuir*, vol. 16, no. 20, pp. 7777–7782, 2000.
- [14] F. Shi, Z. Wang, and X. Zhang, "Combining a layer-by-layer assembling technique with electrochemical deposition of gold aggregates to mimic the legs of water striders," *Advanced Materials*, vol. 17, no. 8, pp. 1005–1009, 2005.
- [15] K. Tadanaga, J. Morinaga, A. Matsuda, and T. Minami, "Superhydrophobic—Superhydrophilic micropatterning on flower-like alumina coating film by the sol—Gel method," *Chemistry of Materials*, vol. 12, no. 3, pp. 590–592, 2000.
- [16] S. Wang, L. Feng, and L. Jiang, "One-step solution-immersion process for the fabrication of stable bionic superhydrophobic surfaces," *Advanced Materials*, vol. 18, no. 6, pp. 767–770, 2006.
- [17] T. Sun, G. Wang, H. Liu, L. Feng, L. Jiang, and D. Zhu, "Control over the wettability of an aligned carbon nanotube film," *Journal of the American Chemical Society*, vol. 125, no. 49, pp. 14996–14997, 2003.
- [18] L. Feng, Y. Song, J. Zhai et al., "Creation of a superhydrophobic surface from an amphiphilic polymer," *Angewandte Chemie*, vol. 42, no. 7, pp. 800–802, 2003.
- [19] L. Jiang, Y. Zhao, and J. Zhai, "A lotus-leaf-like superhydrophobic surface: a porous microsphere/nanofiber composite film prepared by electrohydrodynamics," *Angewandte Chemie*, vol. 43, no. 33, pp. 4338–4341, 2004.
- [20] M. Ma, R. M. Hill, J. L. Lowery, S. V. Fridrikh, and G. C. Rutledge, "Electrospun poly(styrene-block-dimethylsiloxane) block copolymer fibers exhibiting superhydrophobicity," *Langmuir*, vol. 21, no. 12, pp. 5549–5554, 2005.
- [21] X. Lu, J. Zhou, Y. Zhao, Y. Qiu, and J. Li, "Room temperature ionic liquid based polystyrene nanofibers with superhydrophobicity and conductivity produced by electrospinning," *Chemistry of Materials*, vol. 20, no. 10, pp. 3420–3424, 2008.
- [22] Y. I. Yoon, H. S. Moon, W. S. Lyoo, T. S. Lee, and W. H. Park, "Superhydrophobicity of cellulose triacetate fibrous mats produced by electrospinning and plasma treatment," *Carbohydrate Polymers*, vol. 75, no. 2, pp. 246–250, 2009.
- [23] Y. I. Yoon, H. S. Moon, W. S. Lyoo, T. S. Lee, and W. H. Park, "Superhydrophobicity of PHBV fibrous surface with bead-on-string structure," *Journal of Colloid and Interface Science*, vol. 320, no. 1, pp. 91–95, 2008.
- [24] H. M. Ji, H. W. Lee, M. R. Karim et al., "Electrospinning and characterization of medium-molecular-weight poly(vinyl alcohol)/high-molecular-weight poly(vinyl alcohol)/montmorillonite nanofibers," *Colloid and Polymer Science*, vol. 287, no. 7, pp. 751–758, 2009.
- [25] H. J. Jin, J. Chen, V. Karageorgiou, G. H. Altman, and D. L. Kaplan, "Human bone marrow stromal cell responses on electrospun silk fibroin mats," *Biomaterials*, vol. 25, no. 6, pp. 1039–1047, 2004.
- [26] C. J. Israilides, A. Smith, J. E. Harthill, C. Barnett, G. Bambalov, and B. Scanlon, "Pullulan content of the ethanol precipitate from fermented agro-industrial wastes," *Applied Microbiology and Biotechnology*, vol. 49, no. 5, pp. 613–617, 1998.
- [27] T. D. Leathers, "Biotechnological production and applications of pullulan," *Applied Microbiology and Biotechnology*, vol. 62, no. 5-6, pp. 468–473, 2003.
- [28] R. Schuster, E. Wenzig, and A. Mersmann, "Production of the fungal exopolysaccharide pullulan by batch-wise and continuous fermentation," *Applied Microbiology and Biotechnology*, vol. 39, no. 2, pp. 155–158, 1993.
- [29] M. R. Karim, H. W. Lee, R. Kim et al., "Preparation and characterization of electrospun pullulan/montmorillonite nanofiber mats in aqueous solution," *Carbohydrate Polymers*, vol. 78, no. 2, pp. 336–342, 2009.

- [30] G. Ren, X. Xu, Q. Liu et al., "Electrospun poly(vinyl alcohol)/glucose oxidase biocomposite membranes for biosensor applications," *Reactive and Functional Polymers*, vol. 66, no. 12, pp. 1559–1564, 2006.
- [31] C. Shao, H.-Y. Kim, J. Gong, B. Ding, D.-R. Lee, and S.-J. Park, "Fiber mats of poly(vinyl alcohol)/silica composite via electrospinning," *Materials Letters*, vol. 57, no. 9-10, pp. 1579–1584, 2003.
- [32] K. H. Hong, J. L. Park, I. N. Hwan Sul, J. H. Youk, and T. J. Kang, "Preparation of antimicrobial poly(vinyl alcohol) nanofibers containing silver nanoparticles," *Journal of Polymer Science B*, vol. 44, no. 17, pp. 2468–2474, 2006.
- [33] N. Ristolainen, P. Heikkilä, A. Harlin, and J. Seppälä, "Poly(vinyl alcohol) and polyamide-66 nanocomposites prepared by electrospinning," *Macromolecular Materials and Engineering*, vol. 291, no. 2, pp. 114–122, 2006.
- [34] J. H. Park, M. R. Karim, I. K. Kim et al., "Electrospinning fabrication and characterization of poly(vinyl alcohol)/montmorillonite/silver hybrid nanofibers for antibacterial applications," *Colloid and Polymer Science*, vol. 288, no. 1, pp. 115–121, 2010.
- [35] B. Duan, L. Wu, X. Li et al., "Degradation of electrospun PLGA-chitosan/PVA membranes and their cytocompatibility in vitro," *Journal of Biomaterials Science*, vol. 18, no. 1, pp. 95–115, 2007.
- [36] H. W. Lee, M. R. Karim, H. M. Ji et al., "Electrospinning fabrication and characterization of Poly(vinyl alcohol)/montmorillonite nanofiber mats," *Journal of Applied Polymer Science*, vol. 113, no. 3, pp. 1860–1867, 2009.
- [37] S. Krause, D. R. Paul, and S. Newman, *Polymer-Polymer Compatibility, in Polymer Blends*, Academic Press, New York, NY, USA, 1978.
- [38] D. F. Varnell and M. M. Coleman, "FT i.r. studies of polymer blends: V. Further observations on polyester-poly(vinyl chloride) blends," *Polymer*, vol. 22, no. 10, pp. 1324–1328, 1981.
- [39] D. F. Varnell, J. P. Runt, and M. M. Coleman, "FT i.r. and thermal analysis studies of blends of poly(ϵ -caprolactone) with homo- and copolymers of poly(vinylidene chloride)," *Polymer*, vol. 24, no. 1, pp. 37–42, 1983.
- [40] E. M. Woo, J. W. Barlow, and D. R. Paul, "Phase behavior of blends of aliphatic polyesters with a vinylidene chloride/vinyl chloride copolymer," *Journal of Applied Polymer Science*, vol. 32, no. 3, pp. 3889–3897, 1986.
- [41] M. S. Islam, N. Akter, and M. R. Karim, "Preparation of superhydrophobic membranes by electrospinning of fluorinated silane functionalized pullulan," *Colloids and Surfaces A*, vol. 362, no. 1–3, pp. 117–120, 2010.
- [42] J. S. Lee, K. H. Choi, H. D. Ghim et al., "Role of molecular weight of atactic poly(vinyl alcohol) (PVA) in the structure and properties of PVA nanofabric prepared by electrospinning," *Journal of Applied Polymer Science*, vol. 93, no. 4, pp. 1638–1646, 2004.
- [43] H. P. Seo, C. W. Son, C. H. Chung et al., "Production of high molecular weight pullulan by *Aureobasidium pullulans* HP-2001 with soybean pomace as a nitrogen source," *Bioresource Technology*, vol. 95, no. 3, pp. 293–299, 2004.
- [44] R. F. T. Stepto, *Polymer Networks*, John Wiley & Sons, Chichester, UK, 1998.
- [45] Y. M. Shin, M. M. Hohman, M. P. Brenner, and G. C. Rutledge, "Electrospinning: a whipping fluid jet generates submicron polymer fibers," *Applied Physics Letters*, vol. 78, no. 8, pp. 1149–1151, 2001.

Research Article

New Resistive Switching and Self-Regulating Heating in Foliated Graphite/Nickel Polyvinyl Chloride Nanocomposites

Omar A. Al-Hartomy,^{1,2} Falleh Al-Salamy,³ A. A. Al-Ghamdi,² Attieh A. Al-Ghamdi,⁴
A. M. Abdel Daiem,^{2,5} and Farid El-Tantawy⁶

¹ Department of Physics, Faculty of Science, University of Tabuk, Tabuk 71491, Saudi Arabia

² Department of Physics, Faculty of Science, King Abdulaziz University, Jeddah, P.O. Box 80203, Jeddah 21569, Saudi Arabia

³ Department of Mathematics, Faculty of Science, University of Tabuk, Tabuk 71491, Saudi Arabia

⁴ Electronics, Communications, and Photonics Program, King Abdulaziz City for Science and Technology, Riyadh, Saudi Arabia

⁵ Department of Physics, Faculty of Science, Zagazig University, Zagazig 44519, Egypt

⁶ Department of Physics, Faculty of Science, Suez Canal University, Ismailia 41522, Egypt

Correspondence should be addressed to Farid El-Tantawy, faridtantawy@yahoo.com

Received 18 May 2011; Revised 26 June 2011; Accepted 18 July 2011

Academic Editor: Sadhan C. Jana

Copyright © 2011 Omar A. Al-Hartomy et al. This is an open access article distributed under the Creative Commons Attribution License, which permits unrestricted use, distribution, and reproduction in any medium, provided the original work is properly cited.

Polyvinyl chloride- (PVC-) based nanocomposites containing nanosized graphite and nickel nanoparticles (GN) as conductive fillers to achieve positive temperature coefficient of resistance (PTCR) thermistors and self-regulating heater function have been successfully fabricated. The microstructure of the foliated graphite and nanocomposites was examined by scanning electron microscopy (SEM). The effect of GN content on the static electrical conductivity, carrier's mobility, and number of charge carriers of the nanocomposites was studied. The applicability of nanocomposites as PTCR thermistors was examined by monitoring the conductivity as a function of temperature. It is found that the conduction mechanism in PVC/GN nanocomposites is governed by tunneling mechanism. Also, the applied voltage versus current and temperature were studied to check the applicability of composites as self-regulating heater. The results show that the PVC/GN nanocomposites might have potential applications in PTCR devices, self-regulating heater, and temperature sensors.

1. Introduction

The design and applications of electroactive conductive polymer nanocomposites in the electrical and electronic fields have significantly affected the modern technology and added a new dimension to scientific interest [1–3]. The most economical route for fabrication of electro active conducting polymer composites is the inclusion of a conductive filler such as carbon black, carbon nanotubes, graphite, metal powders, ceramic oxides, polyaniline, and others in an insulating polymer matrix and subsequent compaction by compression molding [4–8]. These electro active nanocomposites attracted great interests due to their potential applications in various hi-tech aspects, for example, positive and/or negative temperature coefficient of resistance (PTCR/NTCR) thermistors [9], electrochemical displays

[10], sensors [11, 12], catalysis [13], redox capacitors [14], electromagnetic shielding [15, 16], radar evasion [17], rechargeable batteries [18, 19], conductive inks and antistatic textiles [20, 21], and aero space [3, 12] as well as in secondary battery and bipolar plates in the polymer electrolyte membrane fuel cell, and so forth [20]. A PTCR composite is a grain-boundary resistive effect which is characterized by an increase in resistivity with increasing temperature [14–16]. The traditionally thermistor materials irrespective of its applications can be broadly divided into three categories, namely, metals (such as titanium and platinum), semiconductors (such as Si, Ge, and SiC), and ceramic oxide semiconductors (like single- and multicomponent oxides) [17, 18]. The use of traditional thermistors has been confined because of the low room temperature conductivity and the oxidation of the metallic particles that severely limits

the current flow [11, 19]. Furthermore, when particulate fillers such as carbon black and metal are added to polymeric systems, a huge increase in the melt viscosity is observed which makes the melt processing of the composites more difficult and disrupts the mechanical properties restricting their application of thermistors [21]. Recently, the demand of PTCR composites with high room temperature conductivity is rising in markets, in a wide range of applications especially in automobiles that need PTCR materials with large current carrying capacity [14], self-regulating heater [18], protection circuits [19], temperature sensors [8, 15], infrared radiation detector sensors, flow meters [5], current limiters [7], temperature controlled heater [10], ambient thermal state indicators [11], and so on. To our best knowledge, there have been no reported investigation of the PTCR thermistors and self-regulating heater from dispersed dual conducting phases foliated graphite and nickel nanoparticles (GN) into polyvinyl chloride (PVC) matrix. In the current study, our investigations are focused on the fabrication and development of newly electrically conducting PVC-based composites, containing multicomponent fillers (i.e., GN) and on the possibilities for their potential application in PTCR thermistors devices and self-regulating heater.

2. Experimental Details

2.1. Materials. Natural flake graphite purchased from Shandong Qingdao Graphite Company (Qingdao, China) with an average diameter of 500 μm is used for preparing the expanded graphite (exfoliated). Commercially concentrated sulfuric and nitric acids obtained from Egyptian Chemical Company, Cairo, Egypt, were used as chemical intercalate and oxidizer to prepare exfoliated graphite. 95% (v/v) alcohol and distilled water were used as solvents for preparation of foliated (nanosheets) graphite. Polyvinyl chloride (PVC) with an average molar mass number being 2000 was supplied from Tokyo Chemical Industry Co., Ltd., Tokyo, Japan. Nickel powder was supplied by Wako Chemical Company with particle size of 10 micrometers.

2.2. Preparation of Exfoliated Graphite. Natural flake graphite was first dried in a vacuum oven for 24 h at 120°C. Then, a mixture of concentrated sulfuric and nitric acids (ratio 3 : 1, v/v) was slowly added to a glass flask containing graphite flakes with vigorous stirring. After 36 h of reaction, the acid-treated graphite flake was filtered and washed with deionized water until the pH level of the solution reached 6.6. After being dried at 100°C for 72 h, the resulting graphite intercalation compound was subjected to a thermal shock at 1050°C for 30 seconds in a muffle furnace to form exfoliated (expanded) graphite.

2.3. Preparation of Graphite Nanosheets. 1 g of exfoliated graphite was mixed and saturated with 400 mL alcohol solution consisting of alcohol and distilled water with a ratio of 68 : 32 for 24 h. The mixture was then subjected to ultrasonic irradiation with a power of 400 watt for 24 h. After 24 h of sonication, exfoliated graphite particles were

effectively fragmented into foliated (nanosheets) graphite. The foliated graphite dispersion was then filtered and dried at 100°C to remove residual solvents. The as-prepared foliated graphite powder will be called graphite nanosheets (G) throughout the paper.

2.4. Preparation of Nickel Nanoparticles. The starting material for ball milling is Ni powder (250 mesh) with purity above 99.9%. The Ni powder was placed in a stainless steel vial with stainless steel balls of 10 mm diameter. The ball-to-powder ratio 20 : 1 was used in the planetary mill (Marconi MA 350 ball mill) at 400 rpm under argon atmosphere for 6 h to obtain nickel nanoparticles (N).

2.5. Preparation of Conducting PVC-Based Nanocomposites. The conducting fillers are composed of graphite nanosheets (thickness: 30–50 nm) with an average thickness of about 40 nm (the number of sheets in the platelets is 100) and Ni with an average particles size of 12 nm. First, the as-prepared graphite nanosheets and nickel nanoparticles 80/20 wt% were mixed together in a kitchen machine Philips mixer for 1 h. Second the as-received conducting mixture was added to the PVC matrix and mixed for 30 min. Then the mixtures were transferred to a hot press and tested samples were prepared at pressure of 40 KN/m² and temperature of 180°C for 30 min. Several batches of PVC/GN weight ratios were considered: 97 : 03, 96 : 07, 91 : 09, and 88 : 12, respectively, and abbreviated as GN3, GN6, GN9, and GN12, respectively.

2.6. Characterization and Tests. Scanning Electron Microscopy (SEM) micrographs and energy dispersive X-ray analysis (EDX) spectra were obtained with a JEOL JSM 6400 scanning electron microscope equipped with a Link analytical system. The electron energy used was 15 keV. The specimens were coated with carbon using a vacuum evaporator (JEOL, GEE 500). The specific electrical conductivity temperature dependence was performed for the composites by dc two-probe method using a computer-aided system in the temperature range from 22°C to 150°C in air. The current was measured through the sheet sample under a steady constant voltage using a digital Keithley 642 electrometer. The two sides of the samples were bended with Cu rod during curing process to reduce the contact resistance. Hall effect measurement was used to determine the carrier type, concentration, and mobility. The measurements were performed using the van der Pauw configuration under direct current ranging from 2×10^{-3} to 4×10^{-4} A, and the applied magnetic field was 0.33 T. The equipment used for this purpose was a Keithley source meter (model 231). The current-voltage ($I - V$) characteristic curves were measured with a precision semiconductor parameter analyser (Keithley 442 source measure unit). Silver paste was used to ensure a good contact of the sample surface with copper electrodes. The temperature for each applied voltage on the sample was measured by thermocouple embedded inside the samples during compression molding. The dielectric constant of the composite specimen was obtained from the capacitance of the specimen, the area of Ag electrode, and the thickness

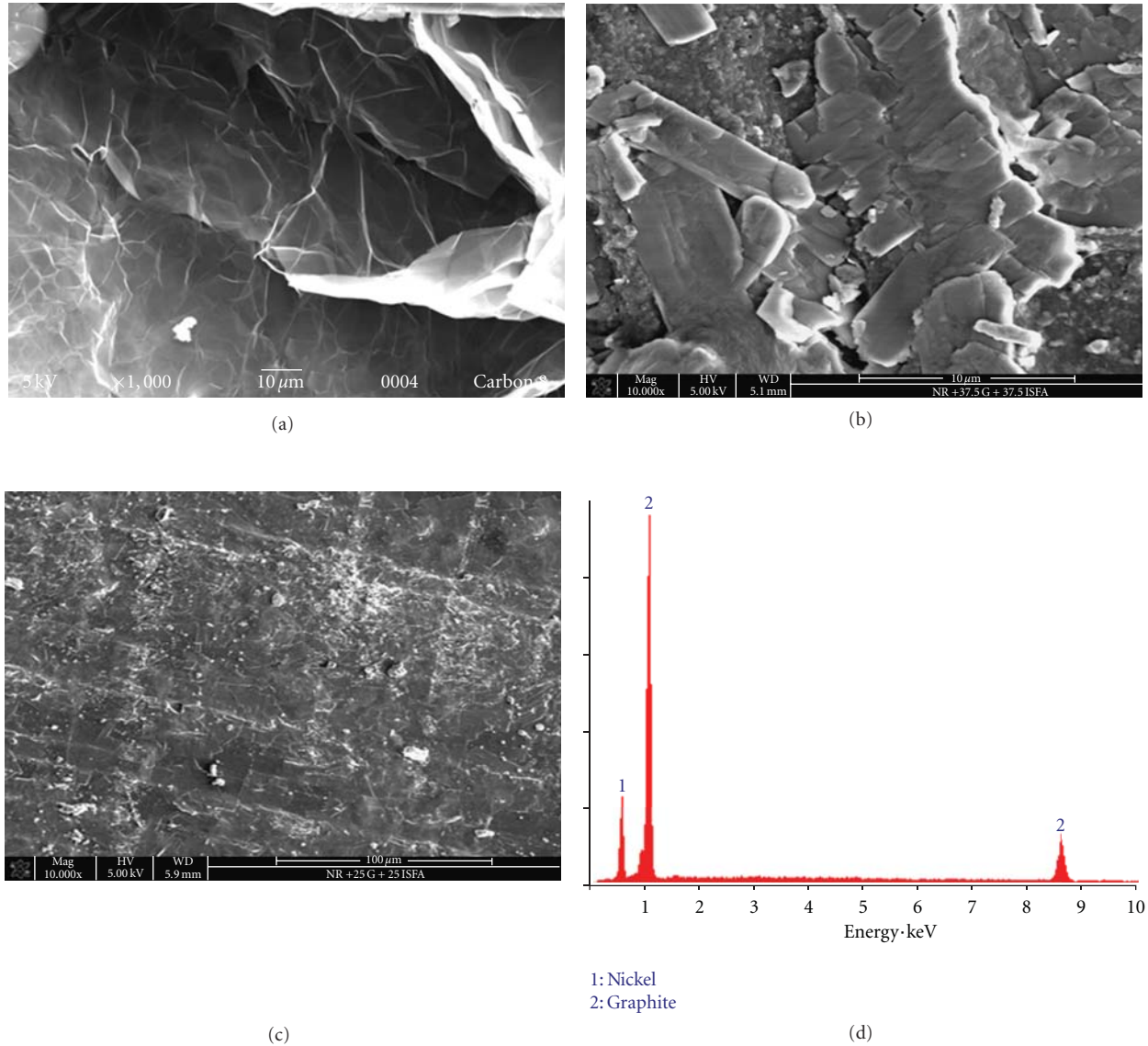


FIGURE 1: (a) SEM images of graphite nanosheets prepared after 24 h ultrasonic treatment and (b) SEM image of GN12 sample magnification with 10 x 0000. (c) SEM image of GN12 sample magnification with 1000 and (d) EDX pattern recorded for GN nanoparticles.

of the composite specimen. Circular-shaped samples with 20 mm diameter and ca. 1.3 mm thickness were prepared for dielectric measurement. Silver paste was used to coat the two sides of the specimen as electrodes. The capacitance of the specimen was measured with a network analyzer (E38362B) at frequency of 100 Hz. The specific heat capacity (C_p) of the samples was calculated using differential scanning calorimeter measurements (Perkin-Elmer DSC-2; Perkin Elmer Cetus Instruments, Norwalk, CT) using sapphire as the reference material.

3. Results and Discussion

3.1. Network Structure Observation of Nanocomposites. SEM observations from cross-sections of foliated graphite were performed to understand the microstructure occurrence

during intercalation. Figure 1(a) shows the SEM image of foliated graphite nanosheets prepared based on 24 h ultrasonic irradiation. It is clearly apparent that the exfoliated graphite worms have been completely torn into foliated, named graphite nanosheets. The powder has an apparent density of about 0.015 g/cm^3 , much lower than the mass density of the original natural flake graphite which is 2.2 g/cm^3 [1, 7].

Generally, the entire concept of electrical properties like percolation and PTCR behavior in nanocomposite thermistors is mainly dependent on microstructure and filler aspect ratio [5, 21]. The surface morphology of foliated graphite and the composites was examined by scanning electron microscopy. Typical SEM micrograph of GN12 with different magnification is depicted in Figures 1(b) and 1(c). As can be seen, the GN nanoparticles have good affinity and

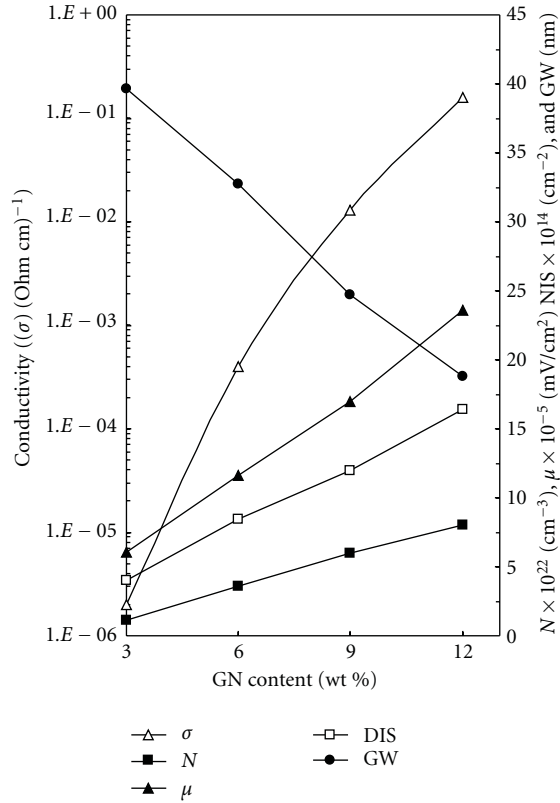


FIGURE 2: Electrical conductivity (σ), carriers mobility (μ), and number of charge carriers (N) versus GN content in the PVC/GN nanocomposites.

entanglements to PVC matrix. The PVC matrix is absorbed and/or coated into the galleries of GN, and the presence of GN in the interfacial regimes between PVC particles shows the nanocomposites without distinguishing individual phases and forming a network of conductive paths. On the other hand, in continuous phase of composites, GN is bonded and entangled well among particles, and bonded particles show uniform layered structure. The uniformity in the continuous phase of composites yield a higher electrical conductivity as confirmed later in this paper.

Figure 1(d) shows the EDX pattern recorded for GN nanoparticles. The strong peaks for graphite and nickel were noted in the spectrum. No other impurities such as sulfur and nitrogen were detected confirming the high purity of graphite nanosheets. The elemental analysis for graphite and nickel was shown to have an average atomic percentages for G : Ni as 80 : 20, consistent with the elemental stoichiometric ratio of starting materials.

3.2. Static Electrical Properties. Electrical conductivity is the most sensitive method to monitor the continuity of the conductive filler phase in the entire host polymer matrix [20, 21]. Static electrical conductivity of green PVC and PVC/GN nanocomposites at room temperature of about 25°C is depicted in Figure 2. Green PVC is electrically nonconductive with a volume conductivity of less than 10^{-16} S/cm in dry state at room temperature [2, 3]. It is observed that

the electrical conductivity increases with increasing GN concentration into composites. Higher content of PVC insulating matrix can block the electrically conductive path. The increase in the conductivity of the composite is attributed to the formation of graphite-nickel clusters [1, 2]. With increasing the GN content in composite, electrical conductivity increases continuously, this depends upon the conductive path or contact distance between conductive particles [1, 2]. At higher content of GN, every GN particle is connected to neighboring GN particle that forms surface-to-surface interaction. Therefore, GN in the composite forms a full conductive network because GN particles have ability to tangle with each other owing to their porous structure [4, 7].

It is interesting to note that the low percolation threshold in the PVC nanocomposites indicates that the GN nanoparticles have maintained their large aspect ratios during processing and form an electrically conductive network throughout the PVC matrix as confirmed by SEM images in Figures 1(b) and 1(c). The percolation threshold of PVC/GN nanocomposites is 1 wt%. The percolation threshold for the electrical conductivity strongly depends on the geometry and high aspect ratio of the conducting fillers [8]. Fillers with elongated geometry such as fibers or sheets can be used to achieve very low percolation threshold value, due to the fact that fibers or sheets with higher aspect ratios have great advantage over spherical or elliptical fillers in forming conducting networks in polymer matrices [7, 8]. This advantage in forming conducting network can be explained by excluded volume theory. The excluded volume of an object is defined as a volume around an object into which the center of another similar object is not allowed if overlapping of the two objects is to be avoided. The more extreme the geometry of the filler particle, the larger its excluded volume [11–14]. The larger the excluded volume, the lower the percolation threshold. These high-aspect-ratio sheets possess great advantages in forming conducting network in polymer matrix, leading to a lower percolation threshold and linear increasing conductivity.

Again, to confirm the above facts on the effect of GN on conductivity, we measured the carriers mobility (μ) and number of charge carriers per unit volume (N) as shown in Figure 2. It is clearly seen that both μ and N increase with increasing GN concentration into composites. The increase of both μ and N is due to the combined effect of an increase in the dimension density of conductive phases and a decrease in the interparticle gaps among conductive sites. This is strong clue that the GN nanoparticles act as carrier's reservoir into PVC matrix, and improving the conductive pathway entire composites. This result leads to the facilities of charge carriers diffusion within PVC matrix, and thus the electrical conductivity increases.

In order to confirm the above facts, we estimated the density of interface states (DIS) at the grain boundary determined by using the following [15]:

$$\text{DIS} = \left(\frac{2\epsilon N E_a}{q} \right)^{1/2}. \quad (1)$$

Once the concentration of charge carriers (N) and activation energy (E_a) are known, the gap width (GW) among conductive sites was determined by the following:

$$GW = \frac{N}{DIS}. \quad (2)$$

The computed values of DIS and GW as a function of GN content is depicted in Figure 2. It is clear that DIS increases while GW decreases with increasing GN content into composites. This is ascribed to the fact that the inclusion of GN content into composites enhances the number of elastically effective chains and interfacial bonding among filler and matrix.

However, the relation between composite conductivity and conducting filler contents in the vicinity of the percolation threshold can be described by a simple power law [6, 8]:

$$\sigma_c = \sigma_f (\phi_f - \phi_c)^\beta, \quad (3)$$

where σ_c is the composite conductivity, σ_f is the conductivity of conductive filler, ϕ_f is the volume fraction of conductive filler, ϕ_c is the percolation threshold, and β is the critical exponent. For lattice in three dimensions, β usually lies between 1.65 and 2.0, accepted as a universal value [5, 9].

The computed value of the critical exponent (β) for PVC/GN nanocomposites is 3.12, and this value is much higher than the universal one, indicating the nonuniversal transport behavior of the PVC/GN nanocomposites [15–18]. It has been demonstrated that very high values of critical exponents tend to occur when the conducting particles have extreme geometries [5, 6]. Presence of tunneling conduction can also lead to nonuniversal critical exponent [10, 11]. The graphite nanosheets used here possess an average aspect ratio of as high as about 400. Such an extreme geometry might be a factor contributable to the high critical exponent. Thus, tunneling through the insulating PVC barriers is expected leading to nonuniversal transport properties of the conducting nanocomposites [7, 8].

3.3. PTCR Thermistors and Transport Mechanism. The temperature dependence of conductivity was examined, as a tool for understanding the mechanism of charge carrier's transport in the PVC/GN nanocomposites and to get a possibility of the application of PVC/GN nanocomposites as PTCR thermistors devices. The temperature dependence of electrical conductivity of PVC/GN nanocomposites is depicted in Figure 3. It is seen that a transition temperature of PTCR curves systematically moved to higher temperatures as the GN content was increased. With increasing GN content, the transition temperature shifted higher. This behavior indicates that more volume expansion of the polymer, allowed for by the increased temperature, was required to pull the conducting particles apart [21]. Increasing the GN content well tended to further decrease the room temperature resistivity and the magnitude in the PTC effect. This strong clue indicates that the inclusion of GN content enhances the thermal stability and skeleton

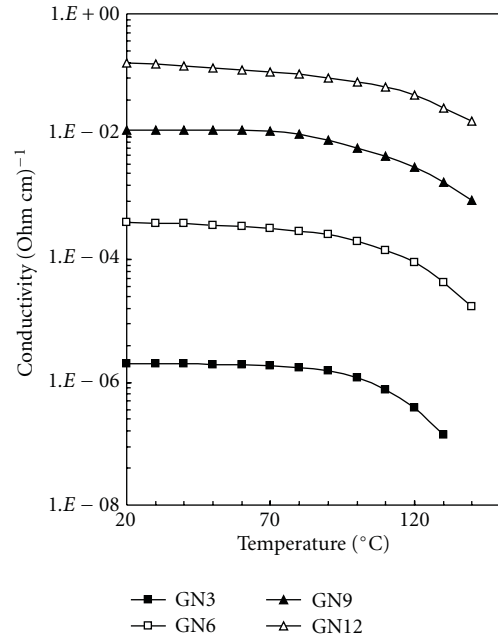


FIGURE 3: Electrical conductivity temperature dependence of PVC/GN nanocomposites.

molecular structure of nanocomposites. Clearly, at relatively low temperature, the conductivity slightly decreases up to certain temperature (i.e., so-called critical or percolation temperature) after which the conductivity quickly increases depending on GN content into composites. There are two main reasons evoked for these phenomena. First, as potential barrier increases proportionally with temperature, electrical resistivity increases very quickly as it depends exponentially on potential barrier. Second, at high temperature, the thermal expansion of polymer increases and the intermolecular distance among conductive segments increases, which leads to the scattering of charge carriers and thereof the conductivity decreases (i.e., resistivity increases).

The electrical conductivity (σ) is related to the activation energy (E_a) by [17, 18]

$$\sigma = A \exp\left(-\frac{E_a}{K_B T}\right), \quad (4)$$

where A is a constant, K_B is the Boltzmann constant, and T is the Kelvin temperature.

The activation energy of the nanocomposites was calculated from the slope of $\ln \sigma$ versus $1/T$ curve, and the data is depicted in Figure 4. It is observed that the activation energy decreases with an increase of GN amount into the nanocomposites. This could occur due to the increased charge carrier concentration, which leads to an increase of the localized state density in the band gap [1, 16].

Mott's Variable-Range-Hopping (VRH) model is extensively used to analyze the temperature dependence of dc conductivity in conducting polymer composites and for

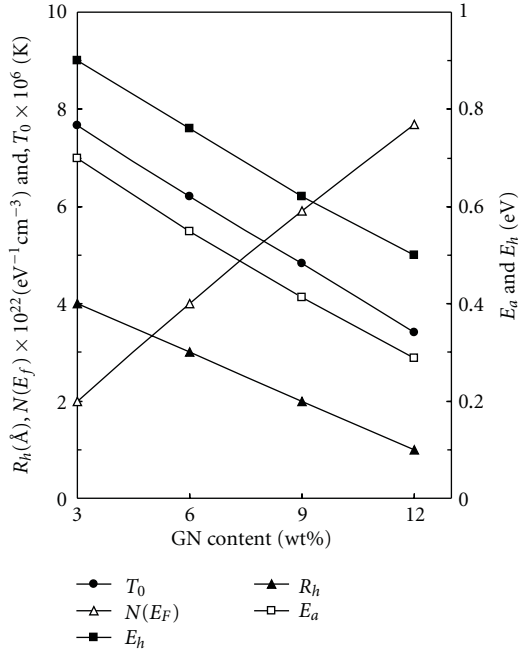


FIGURE 4: Computed values of R_h , $N(E_f)$, T_0 , E_a , and E_h for PVC/GN nanocomposites.

the three-dimensional hopping mechanism, which is expressed as [19, 20]

$$\sigma = \sigma_0 \exp\left(-\frac{T_0}{T}\right)^{1/4}, \quad (5)$$

$$T_0 = \frac{16}{K_B N(E_f) \gamma^3},$$

where $N(E_f)$ is the density of states at the Fermi level, T_0 is the Mott's temperature, and γ is the localization length and is taken to be 3\AA [7, 8].

The average hopping distance (R_h) between two localized states and the hopping energy (E_h) is given by the following [3, 13]:

$$R_h = \left(\frac{3}{8}\right) \left(\frac{T_0}{T}\right)^{1/4}, \quad (6)$$

$$E_h = \left(\frac{1}{4}\right) K_B T \left(\frac{T_0}{T}\right)^{1/4}.$$

The computed value of T_0 , $N(E_f)$, R_h , and E_h as a function of GN content into composites is depicted in Figure 4. It is evident that T_0 , $N(E_f)$, R_h , and E_h decrease as the GN content increases into composites. The observed values of T_0 , $N(E_f)$, R_h , and E_h point to an effective energy separation between the localized states [16, 19]. It is worth mentioning that the conductivity values and estimated Mott parameters indicate a good interaction between PVC polymer matrix and GN nanoparticles. The interaction among PVC and GN fillers could be explained by the strong molecular interaction between fillers and matrix. Finally, in Figure 4, it is interesting to note that the value of E_a is different from

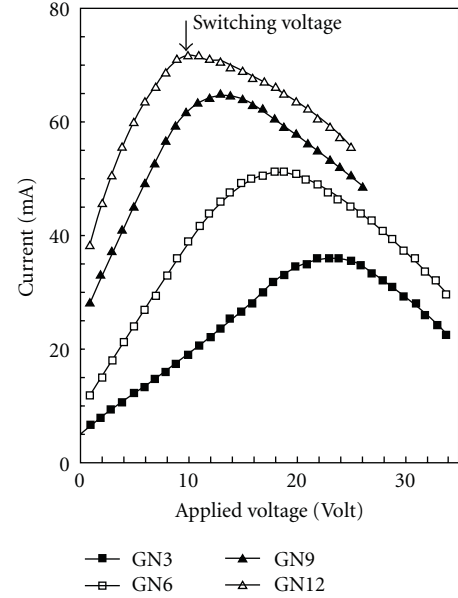


FIGURE 5: Current-voltage dependence of PVC/GN nanocomposites.

the value of E_h . This is strong evidence that the conduction mechanism of PVC/GN nanocomposite is governed by tunneling mechanism as confirmed above [9, 16].

3.4. Voltage-Current Relationship and Self-Heating Behavior.

The variation of current (I) with applied voltage (V) for PVC/GN nanocomposites is depicted in Figure 5. The increase of GN content shifted the $V - I$ curves toward a low electric field and a high current. This indicates that migration of curves will cause a lower nonlinearity [11]. Clearly the $I - V$ characteristics are linear at low applied voltage without any remarkable change of the sample temperature, indicating the tunneling of electrons on the application of voltage [2, 14]. Increasing the electric field above, a certain value depends on GN contents, leading to an increase in the Joule heating effect and consequently an increase in the bulk sample temperature. Therefore, $I - V$ characteristics deviate from linear (Ohmic) to nonlinear (non-Ohmic) behavior. By increasing the electric field to a certain value (i.e., switching voltage, see Figure 5), which depends on GN contents, the current decreases showing negative resistance (i.e., switching effect). The negative resistance is attributed to two reasons. First, at high applied voltage the Joule heating takes place and the temperature of the bulk composites increases. This results in an increase in the interparticle distance among conductive sites and the transport of charge carriers decreases. Second, the decrease of current is clearly generated by a repulsive force among positive and negative charges at high applied potential in the PVC matrix [4].

The dependence of surface temperature (T) on applied voltage for PVC/GN nanocomposites is depicted in Figure 6. It is seen that at low voltage the surface temperature slightly increased. With increasing applied voltage, the surface temperature increases; this is due to the Joule or self-heating effect. It is worthily to note that the temperature

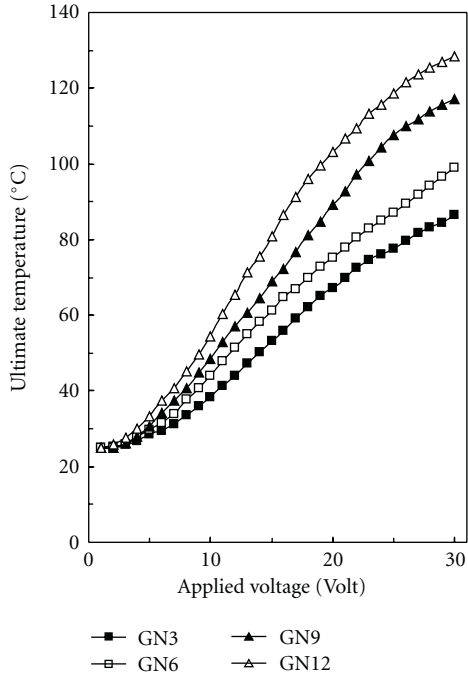


FIGURE 6: Dependence of ultimate temperature on applied voltage of PVC/GN nanocomposites.

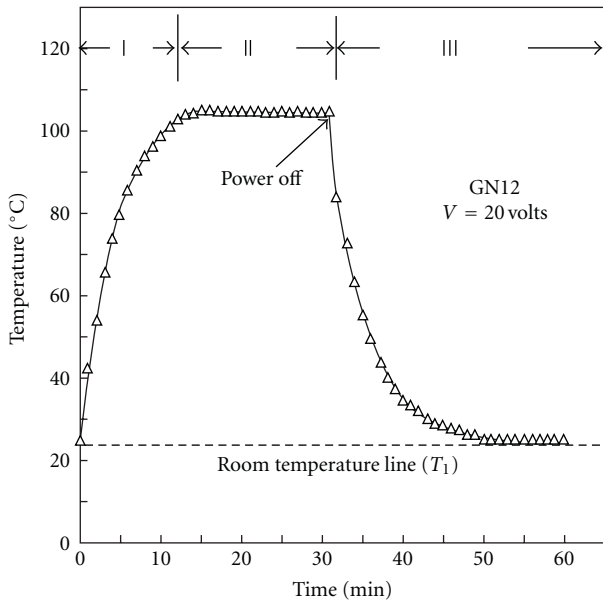


FIGURE 7: Temperature-time dependence of GN12 sample under applied voltage on and off.

increases with increasing GN content in the nanocomposites. Another argument indicates that the thermal stability of the nanocomposites is enhanced by increasing GN loading level into PVC matrix.

The ultimate surface temperature (T) of GN12 sample as a function of time (t) at constant applied power on (22 volts) and off is depicted in Figure 7. In Figure 7, the ($T - t$) curve can be divided into three regimes.

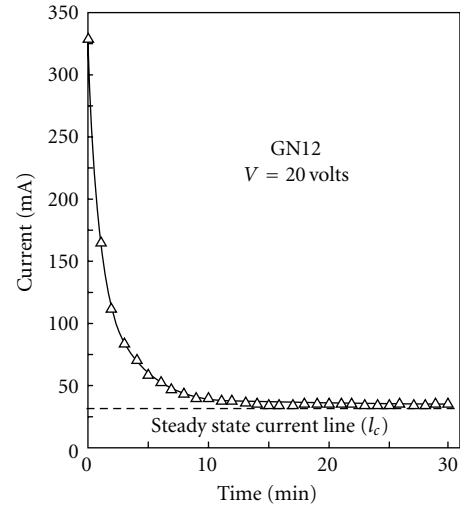


FIGURE 8: Current-time dependence of GN12 sample under applied voltage 20 volts.

Regime I. The applied power on and the temperature increases exponentially with time. In this regime the ($T - t$) curve can be described by the exponential growth function as follows:

$$T(t) - T_1 = (T_2 - T_1) \left[1 - \exp\left(-\frac{t}{\tau_g}\right) \right], \quad (7)$$

where T_1 and T_2 are the ambient and maximum temperature, respectively, and τ_g is the growth time constant, calculated at $t = \tau_g$.

Regime II. The temperature level off to a steady state value (i.e., equilibrium regime) and based on energy balance law the heat gain by applied working power is equal to heat loss by radiation and convection per area per degree per second (h_r) is given by

$$h_r = \frac{VI_c}{T_2 - T_1}, \quad (8)$$

where V is the applied potential and I_c is the steady state current after applied potential.

The variation of current with time for GN12 sample after applied potential is depicted in Figure 8. In Figure 8, it is seen that the current decreases with time and then levels off to a steady value and ($I - t$) curve can be described by the following:

$$I(t) - I_0 = (I_c - I_0) \exp\left(-\frac{t}{\tau_i}\right), \quad (9)$$

where I_0 and I_c are the initial and steady state current, respectively, and τ_i is a decay time constant describing the decay rates of current.

Regime III. In the power off region the ($T - t$) curve can be described by the exponential decay equation:

$$T(t) - T_1 = (T_2 - T_1) \exp\left(-\frac{t}{\tau_d}\right), \quad (10)$$

where τ_d is the decay time constant and is related to the heat transfer from the sample to the surrounding which depends on the GN content in composite.

In this regime (i.e., power off), if the thermistor has a uniform temperature during cooling, the following equation is valid for the cooling, of thermistor in the time interval dt and according to the Newton's law of cooling [4, 5]:

$$C_{p(\text{Newton's})} = \frac{h_r(T_2 - T_1)dt}{m dT}. \quad (11)$$

The solution of this equation for any value of time (t) is given by (8). From (8) and (9) we obtain $C_{p(\text{Newton's})}$ in the form [4, 5]

$$C_{p(\text{Newton's})} = \left(\frac{h_r \tau_d}{m}\right) \left(1 - \exp\left(-\frac{t}{\tau_d}\right)\right). \quad (12)$$

For the sake of using these nanocomposites in industrial applications, it is useful to define the whole amount of heat transfer from the composites using the conservation law of energy. We consider that for an applied voltage (V) on composites at time $t = 0$. The self-heating effect causes the sample temperature to increase from $T(t)$ to $T(t + dt)$ at a time interval from t to $t + dt$, which produce an electrical energy (i.e., Joule heat energy). According to the energy conservation approach one has the following [20, 21]:

$$\int_{t=0}^{t=t_m} VI(t)dt = mC_{p(\text{cons})} \int_{t=0}^{t=t_m} \frac{\partial T_s(t)}{\partial t} dt + Ah_r \int_{t=0}^{t=t_m} ((T(t) - T_1)) dT, \quad (13)$$

where m is the mass of the specimen, A is the area of the specimen, and $C_{p(\text{cons})}$ is the specific heat capacity of the composite.

Taking (7)–(12) into (13) and integrating the resultant equation will obtain the following:

$$\begin{aligned} VI_c t + V(I_0 - I_c)\tau_i \left[1 - \exp\left(-\frac{t}{\tau_i}\right)\right] \\ = mC_{p(\text{cons})}(T_2 - T_1) \left[1 - \exp\left(-\frac{t}{\tau_g}\right)\right] \\ + h_{rc}A(T_2 - T_1)t - h_{rc}A(T_2 - T_1)\tau_g \\ \times \left[1 - \exp\left(-\frac{t}{\tau_g}\right)\right]. \end{aligned} \quad (14)$$

By integrating (10) we get C_{pc} in the form:

$$\begin{aligned} C_{pc} = & \left(\frac{1}{m(T_2 - T_1)}\right) [V_a t_m (T_2 - T_1)] \\ & + \ln\left(\frac{t_m + t_0}{t_0}\right) + V_a I_m t_m \\ & - Ah_r (T_2 - T_1) \left(t_m - \exp\left(-\frac{t}{\tau_g}\right)\right). \end{aligned} \quad (15)$$

The computed values of τ_g , τ_d , τ_i , h_r , $C_{p(\text{Newton's})}$, and $C_{p(\text{conservation})}$, as a function of GN content are recorded in

TABLE 1: Some physical properties of PVC/GN nanocomposites.

Physical parameter	GN3	GN6	GN9	GN12
C_p (measured) (J Kg ⁻¹ K ⁻¹)	680	683	688	693
C_p (Newton's) (J Kg ⁻¹ K ⁻¹)	682	685	689	695
C_p (conservation) (J Kg ⁻¹ K ⁻¹)	681	684	690	694
τ_g (min)	12.34	11.01	8.45	4.65
τ_d (min)	13.43	10.21	7.78	4.23
τ_i (min)	11.98	7.48	6.37	3.98
h_r (J m ⁻² s ⁻¹ °C ⁻¹)	81	74	66	54

Table 1. By a close look at Table 1, it is seen that τ_g , τ_d , and τ_i decrease with increasing GN content into composites. This is referred to where the increase of the number of elastically effective chains density increases with increasing GN content into composites. This is strong clue that the inclusion of GN nanoparticles enhances the skeleton internal structure of the PVC matrix, thus rendering it more thermodynamically stable. Also, it is observed that the h_r decreases as GN content increases indicating the lower efficiency of heat transfer by radiation and convection into composites. This reflects that the inclusion of GN improves the inner architecture structure and crosslinking density of nanocomposites.

Finally, the measured and computed values of specific heat capacity increase with increasing GN content into nanocomposites. It is interesting to note that the measured and estimated values of specific heat capacity by conservation law of energy and Newton's law of cooling are quite close. This is evidenced in that the inclusion of GN improves the thermal stability and thermal conductivity of the nanocomposite. Monitoring dynamic resistivity (i.e., isothermal resistance relaxation with time) provided additional information about the stability of composites. The isothermal resistance changes with time at constant temperature of 110°C for PVC/GN nanocomposites as is depicted in Figure 9. It is clear that the resistance undergoes a sudden increase followed by a decrease in resistance, after which it levels off depending on the GN content into composites. The sudden increase of resistance at the beginning is attributed to a rapid increase of volume expansion of the polymer matrix. It is clear that the time for the resistance to reach the maximum is shorter as the GN content increases in composites. This can be explained where, at low content of GN, the slow diffusion of GN nanoparticles occurs from one grain site to another leading to change the charge distribution which in turn will change the effective carrier density and hence the composite resistivity. In light of the above discussion, we propose that the interfacial bonding and entanglements among PVC moieties increase with the increase of GN contents.

4. Conclusions

In this study a new family of electro active polymer nanocomposites thermistors and self-heating based on poly-vinyl chloride- (PVC-) reinforced foliated graphite and Ni nanoparticles (GN) have been successfully fabricated.

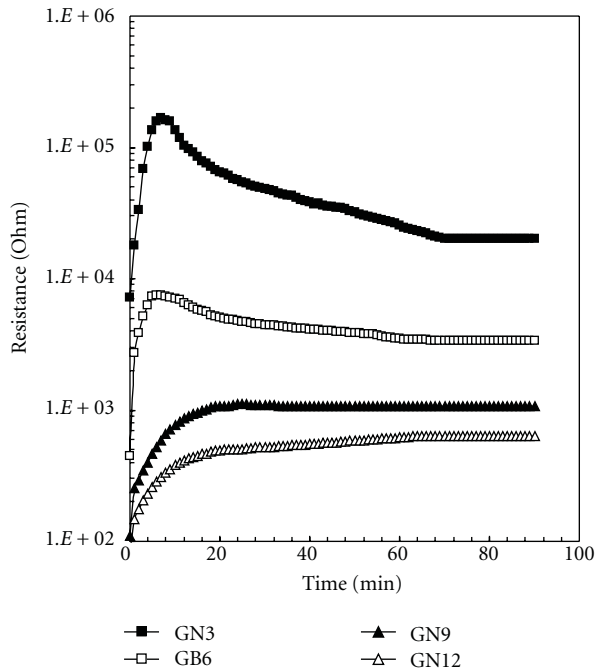


FIGURE 9: Isothermal resistance changes with time at constant temperature of 110°C for PVC/GN nanocomposites.

The effect of GN filler loading on the microstructure and electrical properties was studied. Based on the experimental data, the following conclusions can be made.

- (1) Scanning electron microscope showed that the inclusion of GN nanoparticles improves the skeleton internal structure of PVC/GN composites.
- (2) The electrical conductivity of the PVC/GN nanocomposites showed a transition from an insulator to a semiconductor. The transition could be described by classical percolation theory with a critical exponent of about 3.12. The PVC/GN nanocomposites exhibited the lowest percolation threshold of about 0.7 wt%. This may be attributed to the increased filler form factor in PVC/GN nanocomposites.
- (3) The applicability of nanocomposites obtained as PTCR thermistors was examined by monitoring the conductivity as a function on temperature.
- (4) The applicability of nanocomposites for self-regulating heater and temperature sensor was tested by displaying the change of current and temperature with applied voltage.
- (5) The specific heat capacity and amount of heat transfer by radiation and convection as a function of GN content were estimated by proposed theoretical modeling based on conservation law of energy and Newton's law of cooling.
- (6) Finally, we believe that the PVC/GN nanocomposites open a new direction for future application in electronics devices such as PTCR thermistors, self-regulating heater, and temperature sensors.

Acknowledgment

The authors would like to thank the University of Tabuk, Saudi Arabia, for the financial support of this research.

References

- [1] N. A. Aal, F. El-Tantawy, A. Al-Hajry, and M. Bououdina, "New antistatic charge and electromagnetic shielding effectiveness from conductive epoxy resin/plasticized carbon black composites," *Polymer Composites*, vol. 29, no. 2, pp. 125–132, 2008.
- [2] O. A. Al-Hartomy, F. Al-Solamy, A. A. Al-Ghamdi, M. A. Ibrahim, N. Dishovsky, and F. El-Tantawy, "Pressure sensors based on polyvinyl chloride/graphite/nickel nanocomposites," *Journal of Elastomers and Plastics*, vol. 43, no. 2, pp. 137–153, 2011.
- [3] A. A. Al-Ghamdi, F. El-Tantawy, N. Abdel Aal, E. H. El-Mossalamy, and W. E. Mahmoud, "Stability of new electrostatic discharge protection and electromagnetic wave shielding effectiveness from poly(vinyl chloride)/graphite/nickel nanoconducting composites," *Polymer Degradation and Stability*, vol. 94, no. 6, pp. 980–986, 2009.
- [4] F. El-Tantawy and N. Dishovsky, "Novel V-shaped negative temperature coefficient of conductivity thermistors and electromagnetic interference shielding effectiveness from butyl rubber-loaded boron carbide ceramic composites," *Journal of Applied Polymer Science*, vol. 91, no. 5, pp. 2756–2770, 2004.
- [5] G. Chen, W. Weng, D. Wu, and C. Wu, "PMMA/graphite nanosheets composite and its conducting properties," *European Polymer Journal*, vol. 39, no. 12, pp. 2329–2335, 2003.
- [6] J. Lu, X. Chen, W. Lu, and G. Chen, "The piezoresistive behaviors of polyethylene/foiliated graphite nanocomposites," *European Polymer Journal*, vol. 42, no. 5, pp. 1015–1021, 2006.
- [7] F. El-Tantawy, "Plasticized/graphite reinforced phenolic resin composites and their application potential," *Journal of Applied Polymer Science*, vol. 104, no. 2, pp. 697–709, 2007.
- [8] Z. Todorova, N. Dishovsky, R. Dimitrov, and F. El-Tantawy, "Investigation of electrical properties of elastomer composites filled with TiB₂," *Journal of Elastomers and Plastics*, vol. 39, no. 1, pp. 69–80, 2007.
- [9] G. Chen, W. Weng, D. Wu et al., "Preparation and characterization of graphite nanosheets from ultrasonic powdering technique," *Carbon*, vol. 42, no. 4, pp. 753–759, 2004.
- [10] N. C. Das, D. Khastgir, T. K. Chaki, and A. Chakraborty, "Electromagnetic interference shielding effectiveness of carbon black and carbon fibre filled EVA and NR based composites," *Composites Part A*, vol. 31, no. 10, pp. 1069–1081, 2000.
- [11] X. S. Du, M. Xiao, and Y. Z. Meng, "Facile synthesis of highly conductive polyaniline/graphite nanocomposites," *European Polymer Journal*, vol. 40, no. 7, pp. 1489–1493, 2004.
- [12] S. E. Bourdo and T. Viswanathan, "Graphite/Polyaniline (GP) composites: synthesis and characterization," *Carbon*, vol. 43, no. 14, pp. 2983–2988, 2005.
- [13] S. Shekhar, V. Prasad, and S. V. Subramanyam, "Transport properties of conducting amorphous carbon-poly(vinyl chloride) composite," *Carbon*, vol. 44, no. 2, pp. 334–340, 2006.
- [14] W. Luheng, D. Tianhuai, and W. Peng, "Effects of conductive phase content on critical pressure of carbon black filled silicone rubber composite," *Sensors and Actuators, A*, vol. 135, no. 2, pp. 587–592, 2007.

- [15] W. Lu, H. Lin, D. Wu, and G. Chen, "Unsaturated polyester resin/graphite nanosheet conducting composites with a low percolation threshold," *Polymer*, vol. 47, no. 12, pp. 4440–4444, 2006.
- [16] M. N. Kalasad, M. A. Gadyal, R. K. Hiremath et al., "Synthesis and characterization of polyaniline rubber composites," *Composites Science and Technology*, vol. 68, no. 7-8, pp. 1787–1793, 2008.
- [17] S. Qu and S. C. Wong, "Piezoresistive behavior of polymer reinforced by expanded graphite," *Composites Science and Technology*, vol. 67, no. 2, pp. 231–237, 2007.
- [18] W. Weng, G. Chen, and D. Wu, "Transport properties of electrically conducting nylon 6/foiled graphite nanocomposites," *Polymer*, vol. 46, no. 16, pp. 6250–6257, 2005.
- [19] G. M. Gouda and C. L. Nagendra, "Structural and electrical properties of mixed oxides of manganese and vanadium: a new semiconductor oxide thermistor material," *Sensors and Actuators, A*, vol. 155, no. 2, pp. 263–271, 2009.
- [20] S. Isaji, Y. Bin, and M. Matsuo, "Electrical conductivity and self-temperature-control heating properties of carbon nanotubes filled polyethylene films," *Polymer*, vol. 50, no. 4, pp. 1046–1053, 2009.
- [21] Y. Song and Q. Zheng, "Electric self-heating behavior of acetylene carbon black filled high-density polyethylene composites," *Polymer International*, vol. 53, no. 10, pp. 1517–1522, 2004.

Research Article

Influence of Silanization Treatment on Thermomechanical Properties of Multiwalled Carbon Nanotubes: Poly(methylmethacrylate) Nanocomposites

Carlos Velasco-Santos,^{1,2,3} Ana Laura Martinez-Hernandez,^{1,2,3} Witold Brostow,³ and Victor M. Castaño²

¹División de Posgrado e Investigación, Instituto Tecnológico de Querétaro, Avenue Tecnológico s/n esquina gral. Mariano Escobedo, Colonia Centro Histórico, 76000 Querétaro, QRO, Mexico

²Centro de Física Aplicada y Tecnología Avanzada, Universidad Nacional Autónoma de México, A.P. 1-1010, Santiago de Querétaro, 76000 Querétaro, QRO, Mexico

³Laboratory of Advanced Polymers & Optimized Materials (LAPOM), Department of Materials Science and Engineering, University of North Texas, Denton, TX 76203-5310, USA

Correspondence should be addressed to Carlos Velasco-Santos, carlosv@fata.unam.mx

Received 3 May 2011; Revised 26 July 2011; Accepted 30 July 2011

Academic Editor: Gaurav Mago

Copyright © 2011 Carlos Velasco-Santos et al. This is an open access article distributed under the Creative Commons Attribution License, which permits unrestricted use, distribution, and reproduction in any medium, provided the original work is properly cited.

Unfunctionalized and silanized multiwalled carbon nanotubes (MWNTs) were incorporated in poly(methylmethacrylate) matrices using *in situ* polymerization. Polymer-compatible functional groups on carbon nanotube (CNT) surfaces were characterized by infrared spectroscopy. These chemical moieties improve interaction at interfaces, allowing transfer of mechanical load between the matrix and the dispersed phase as reflected in the resulting improved mechanical and thermophysical properties. The composites were characterized by Raman spectroscopy to evaluate molecular level interactions and dynamical mechanical analysis. Composites with silanized CNTs have higher storage modulus (E') than polymer reinforced with unfunctionalized nanotubes. Considering the average of the samples, only 1 wt.% of silanized nanotubes provides an increase in E' of 165% at room temperature with respect to polymer matrix, and the increments reached are by a factor of 6.8 and 13.6 over the polymer matrix at 80°C and 90°C, respectively. 1 wt% of silanized CNTs increases the glass transition temperature of polymer matrix around 30°C. Microscratch testing results of composites show that unfunctionalized CNTs cause deeper penetration of the indenter than polymer matrix at the same force; however, the composites developed with silanized CNTs present more regular behavior than polymer reinforced with unfunctionalized CNTs.

1. Introduction

The outstanding properties of carbon nanotubes offer possibilities for developing new strong multifunctional composite materials [1–4]. Several studies have demonstrated the relevant high Young's modulus, stiffness, flexibility, high electrical conductivity, and thermal stability that CNTs possess [5–8]. Research focus to produce polymer composites is directed to taking advantage of these features in maximum level [9–13].

Different reports provide evidence of progress in this area. Depending on the polymer and the processing method

used, there are positive effects in the creation of polymeric nanocomposites based on CNTs for mechanical [11–16], electrical [13, 17–20], damping [21], and electroactive properties and artificial muscles [22, 23]. However, to reach the combination of different properties in one material involves diverse challenges. As discussed by Dzenis [4], uniform distribution of CNTs in the matrix is needed. Moreover, the attention has been paid to mechanical properties than to tribological ones. However, the analysis of tribological properties is needed because the ongoing process in several industries of replacement of metal components by polymeric ones requires polymer-based materials (PBMs)

with better tribological properties [24]. Recently studies show that the use of CNTs to improve tribology of PBMs turned out to be a two-edged sword; because, while the penetration depths decrease with increasing concentration of CNTs, the residual depths increase at the same time [16]. Thus, clearly more work also along these lines is needed.

A way to provide uniformity on the distribution of CNTs in a polymeric matrix is functionalization [25–27]. In this paper is presented new evidence related with the efficiency of functionalization to improve compatibility and enhance dispersion and the load transfer of CNTs in polymer nanocomposites. Chemical modification applied to nanotubes is supported in the silanization process, which has been proved as successful method to produce different surface behavior in CNTs. Here we report results for functionalized as well as unfunctionalized carbon nanotube polymer composites. Poly(methyl methacrylate) (PMMA) has been chosen as the matrix because of its wide use.

2. Experimental

Methyl methacrylate monomer (MMA) and 3-(trimethoxysilyl)-propyl methacrylate 98% (3-MAT) were supplied by Aldrich. 2,2'-azoisobutironitrile (AIBN) was donated by GIRSA Company, and arc-discharge MWNTs (ground core materials) were provided by MER Corporation. The core material has around 40 wt% MWNTs. The product is over 99% carbon and is produced without catalysts. MWNTs have 8–30 graphene layers and are 6–20 nm in diameter and 1–5 microns in length.

MWNTs previously purified and oxidized were silanized. Oxidation was achieved with KMnO_4 in H_2SO_4 medium; this kind of purification is much recognized and produces a high yield and high purity CNTs. Nanotubes obtained by this process have been analyzed by transmission electron microscopy (TEM) and Raman spectroscopy in an earlier paper [28]. Silanization was realized in alcoholic solution; silane was added 1 : 1 in weight with respect to the oxidized CNTs. The mix was refluxed for 3 h, maintaining the temperature around 65–70°C and under constant stirring. More details of the reactive concentrations and the procedure to oxidize and silanize CNTs were described in previous publication [28]. Polymer samples and carbon nanotube composites were produced by *in situ* polymerization using AIBN as the initiator. The AIBN quantity, reaction time, and temperature were controlled in order to achieve narrow molecular weight distributions. The reaction to produce each composite was carried out in a flask using MMA and AIBN in a reflux system. In each type of the samples, unmodified CNTs (uCNTs) and previously silanized CNTs (sCNTs) were added after 30 minutes since the reaction beginning; then sample was maintained at 70°C for 2 hours under stirring. The resulting mixture was placed in a glass mold with a latex frame in order to control shrinkage. Finally, the system was controlled at 70°C in an oven for 24 hours to achieve complete polymerization. The materials obtained have the thickness of ≈ 1.8 mm. The samples are identified as follows:



FIGURE 1: Carbon nanotubes dissolved in acetone: untreated (uCNTs), oxidized (oCNTs), and silanized (sCNTs).

neat PMMA (PMMA), a composite with 1 wt.% of uCNTs, and a composite with 1 wt.% of sCNTs.

Two extra samples for each material (PMMA, uCNT composite, and sCNT composite) were prepared to corroborate the nanocomposites and the PMMA behaviour in dynamical mechanical analysis (DMA). The procedure to synthesize the materials was the same described previously.

Infrared analysis was performed using a Vector 33 Bruker spectrophotometer, at 100 scans, with resolution of 1 cm^{-1} . Samples were prepared using KBr tablets.

For dynamical mechanical analysis, the samples were cut to 6 mm width and 25 mm length and tested in a Perkin-Elmer DMA-7 apparatus, using 3-point bending module at the 1.0 Hz frequency. Samples were running three times for each material developed.

Raman's spectra of PMMA and composites were obtained in a Micro-Raman Dilor; a 632 nm laser was used, providing a spectral resolution of 3 cm^{-1} .

Microscratch testing was performed in a machine from CSM, Neuchatel, Switzerland, with their Version 2.3 software. Scratches of 5.00 mm length were performed using a diamond tip with a $200\text{ }\mu\text{m}$ diameter. Samples were tested seven times in different parts of the composite at variable loads from 3.0 N up to 20.0 N.

3. Results and Discussion

3.1. Dispersion in Solvent. Silanization was performed using 3-mercaptopropyl-trimethoxysilane (3-MPT) and 3-(trimethoxysilyl)-propyl methacrylate (3-MAT). CNTs were then dissolved in acetone for 5 minutes using an ultrasonic bath for dispersion and left for further 1 hour without ultrasound. As expected, the dispersion is different, higher for 3-MAT than for 3-MTP. Photographs of suspensions obtained using 3-MAT are displayed in Figure 1.

In this figure, it is possible to observe that the darkest suspension corresponds to the system containing sCNTs. These CNTs stay a longer time (several hours) in suspension, while, in the other two systems, precipitation occurs sooner. Even when the acetone is evaporated and sCNTs are washed once more with hot water and acetone in order to eliminate possible remainders of unattached organosilanes, the nanotubes do not lose their dispersion in the solvent. This effect is produced due to the organosilane's R group attached to carbon nanotube surfaces. Organosilanes can be represented as

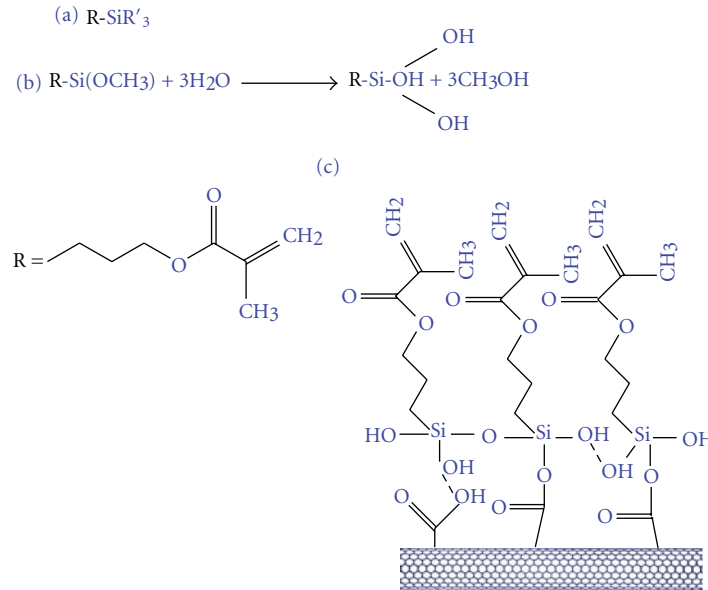


FIGURE 2: Silanization reactions on carbon nanotube surfaces: (a) a general chemical formula of organosilanes, (b) silanization reaction, (c) schematic representation of carbon nanotubes modified with 3-mercaptopropyl-trimethoxysilane.

$R-SiR'_3$, where R is an organofunctional group. The R group can be selected to be reactive or compatible depending on the organic matrix being used. The R' group is typically trimethoxy 3(OCH₃); silicon-oxygen bonds are formed followed by an easy hydrolysis to trisilanol.

Figure 2 shows a schematic representation of silanization with 3-MAT on carbon nanotube surfaces. The dispersion of sCNTs in the suspension depends on the R group. Our 3-MAT silanization produces good dispersion of CNTs in organic solvents such as acetone or ethanol. The R moiety, in this case the methacrylate chain, changes the behavior of MWNTs when attached to the carbon nanotube surface. When 3-MPT is attached to sCNTs, the thiol group produces lower dispersion in acetone.

3.2. Infrared Spectroscopy. Figure 3 shows the infrared spectra for CNTs, oxidized carbon nanotubes (oCNTs), and sCNTs modified with 3-MAT. Spectrum 3(a) shows two bands in the zone of A_{2u} and E_{1u} IR phonon modes at 850 cm⁻¹ and 1576 cm⁻¹, which are typical signals of CNTs [29]. In the oCNTs spectrum 3(b) new peaks are seen. Characteristic bands due to oxidation appear; the signals at 1200 cm⁻¹ and 1346 cm⁻¹ are due to $\nu(C-O)$ and $\delta(O-H)$ in plane, respectively; small bands between 1680 cm⁻¹ and 1740 cm⁻¹ correspond to $\nu(C=O)$ [30].

In the spectrum of oCNT, carboxylate groups prevail, and only few carboxyl groups are produced. This is seen in low intensities of the bands around 1740 cm⁻¹ and 3320 cm⁻¹ which correspond to $\nu(C=O)$ and $\nu(O-H)$, typical signals of carboxyl moieties. Other evidence of carboxyl group is a slight increase in 1346 cm⁻¹ $\delta(O-H)$ and 960 cm⁻¹ $\delta(O-H)$ related with in-plane and out-of-plane vibrations, respectively [30]. By contrast, a higher intensity is seen in the band around 1495 cm⁻¹, and in the peaks between 1600 cm⁻¹ and

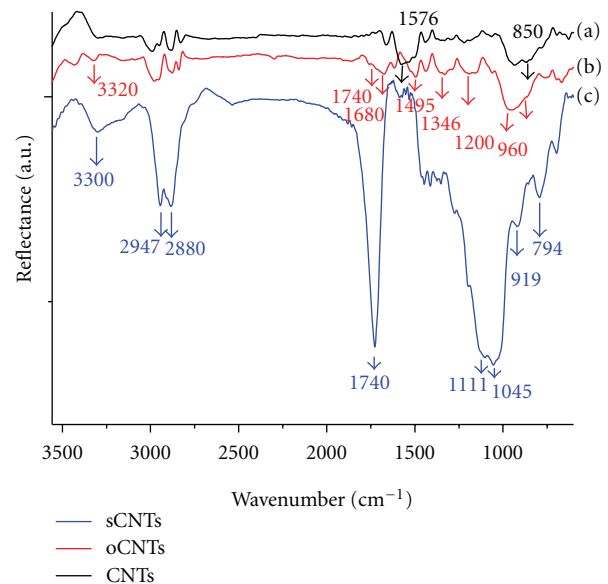


FIGURE 3: Infrared spectroscopy of CNTs, oCNTs, and sCNTs.

1680 cm⁻¹ in comparison with the zone above 1700 cm⁻¹, these corroborate that quinone and carboxylate groups exist in these oxidized nanotubes [30–33]. The peak at 1576 cm⁻¹, assigned to $\nu(C=C)$ in spectrum (a), is notably weaker than that in spectrum (b); this indicates changes in CNT surface due to oxidation [31]; it is known that some damage is produced in CNT walls. In Figure 3(c) we find results of successful silanization process; the bands at 794 cm⁻¹ and 919 cm⁻¹ are typical for $\nu(Si-OH)$ and $\delta(OH)$ out of plane. These bands appear when trimethoxy groups are broken in order to form silanol groups. The silanol groups provide

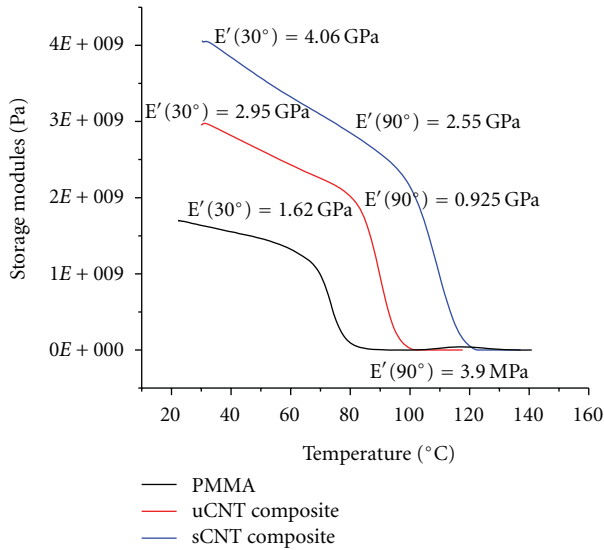


FIGURE 4: Storage modulus E' as a function of temperature for neat PMMA, PMMA with 1.0 wt.% of unfunctionalized CNTs (uCNTs), and 1.0 wt.% of CNTs (sCNTs).

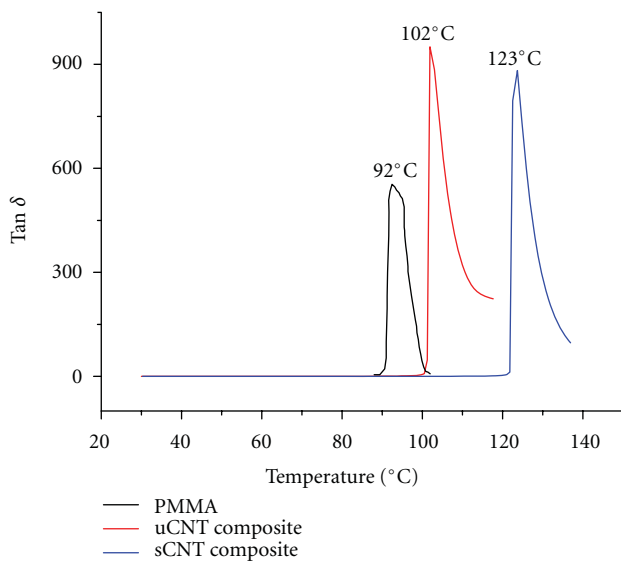


FIGURE 5: $\tan \delta$ for neat PMMA, PMMA with 1.0 wt.% of unfunctionalized CNTs (uCNTs), and 1.0 wt.% of CNTs (sCNTs).

interactions between oxygen of carboxylates and hydroxyl moieties of the oxidized nanotubes and the organosilane. In addition spectrum 3(c) does not show bands between 815 cm^{-1} and 845 cm^{-1} , characteristic signals of nonreacted SiOR groups in organosilane compound [28, 34]. Also the typical band of methoxy group, around 2850 cm^{-1} , does not appear in this spectrum. The peaks at 1045 cm^{-1} and 1111 cm^{-1} are due to Si-O-Si and Si-O-C vibrations [30, 34] and correspond to siloxane units formed during silanization process. The high intensity band at 1740 cm^{-1} becomes stronger due to the ester group $\nu(\text{C}=\text{O})$ vibration which corresponds to methacrylate moiety. Additionally, in the spectrum appear the peaks at 2880 cm^{-1} and 2947 cm^{-1} ,

$\nu(\text{C-H})$ and $\nu_a(\text{C-H})$, respectively [30], these bands are typical for aliphatic groups and correspond to the propyl chain in this case. Both methacrylate and propyl groups belong to the organosilane compound. The band at 3300 cm^{-1} typical of $\nu(\text{O-H})$ is strong in spectrum 3(c) and corresponds to OH vibration of silanol group. This band is often above 3700 cm^{-1} [28, 34]; however, the peak has been located at lower wavenumbers when silanization was performed [33, 34]. It has been suggested that this effect is due to either strong interactions between neighboring silanol groups or between silanol groups and the methacrylate ester moiety of the coupling agent via inter- or intrahydrogen bonding [34]. In our case, the first explanation seems to apply; the strong bands at 1045 cm^{-1} and 1111 cm^{-1} shown in Figure 2 corroborate the Si-O-Si interactions. Moreover, no shifts of ester peak typical position (C=O) are observed in spectrum 3(c). Thus, we infer that Si-O-Si interactions occur during silanization.

3.3. Dynamical Mechanical Analysis Results. Figure 4 shows the close average behavior of the storage modulus (E') as a function of temperature. It is possible to observe in this figure the different behavior of the materials. At 30°C neat PMMA shows a value of $E' = 1.62 \text{ GPa}$; PMMA with 1.0 wt.% of uCNTs shows $E' = 2.95 \text{ GPa}$, while in the composite with sCNT E' is presented at 4.06 GPa. However, at 90°C the respective values are 3.90 MPa, 0.92 GPa, and 2.55 GPa. These results show a relevant rise in the composites with sCNTs and represent an increment in elastic modulus of 82% for the composite with untreated CNTs and 150% for the composite with sCNTs at 30°C, with respect to polymer matrix (PMMA). At 90°C, the average behavior in the composites with uCNTs and sCNTs, E' is higher more than 7.4- and 13.6-fold, respectively, with respect to PMMA. In addition in the sample with sCNTs, $E'(30^\circ\text{C})$ is higher in 34% and $E'(90^\circ\text{C})$ in 1.8-fold with respect to composite which contains unfunctionalized nanotubes.

Three different samples of PMMA and composites reinforced with functionalized and unfunctionalized nanotubes were probed. The materials were synthesized in order to corroborate the behavior of the composites. Polymers reinforced with sCNTs present the same tendency, in as much as $E'(30^\circ\text{C})$ is superior in all composites which contain functionalized nanotubes. Also, uCNTs composites present a storage modulus $E'(30^\circ\text{C})$ higher than PMMA. Thus, even though the storage modulus curves are not uniform in all materials, the tendency is the same and corroborates the efficiency of the functionalization in composite properties. Thus, it is verified that few loads of carbon nanotubes, and even more sCNTs, have important effect in the elastic behavior of these polymer nanocomposites. Table 1 shows storage modulus of the three materials at different temperatures. It is evident that the interaction (analyzed previously by spectroscopy) produced at the interface level by functionalization plays an important role in mechanical properties of these materials.

DMA also provide information about determination of glass transition temperatures T_g [35]. Figure 5 shows

TABLE 1: Results of dynamical mechanical analysis for three different samples of neat PMMA, PMMA with 1.0 wt.% of unfunctionalized CNTs (u-CNTs) and 1.0 wt.% of silanized carbon nanotubes, sCNTs.

Sample	E' (30°C) (GPa)	E' (90°C) (GPa)	T_g °C (Tan delta maximum)
Pmma1	1.24	3.9 MPa	92
Pmma2	1.49	26 MPa	100
Pmma3	1.65	0.519	101
Pmma (average)	1.46	0.183	97
uCNT composite1	2.41	1.25	105
uCNT composite 2	2.95	0.925	102
uCNT composite 3	3.30	1.94	110
uCNT (average)	2.88	1.37	105
sCNT composite 1	3.60	2.06	117
sCNT composite 2	4.06	2.55	123
sCNT composite 3	4.50	2.90	126
sCNT (average)	3.87	2.50	122

$\tan \delta = E''/E'$ as a function of temperature, where E'' is the loss modulus. Taking the T_g at the maximum of $\tan \delta$ peak and PMMA as the reference, addition of untreated CNTs increases the T_g by 10°C, while addition of sCNTs results in a 31°C increment. Since only 1 wt.% of CNTs was added, there are clear evidence of strong interactions between PMMA and sCNTs. Figure shows the tangent delta curves closer to the average behavior in all samples; further results pertaining to the thermal behavior of PMMA and composites are shown in Table 1.

3.4. Raman Spectroscopy. Figures 6(a), 6(b) and 6(c) show Raman spectra in the region from 600 cm^{-1} to 1500 cm^{-1} , 1650 cm^{-1} to 1800 cm^{-1} , and from 2500 cm^{-1} to 3500 cm^{-1} , for neat PMMA, and the composites which contain uCNTs and sCNTs modified with 3-MAT.

The bands situated at 2953 cm^{-1} $\nu(\text{C-H})$ in Figure 6(c), 1462 cm^{-1} $\delta(\text{C-H})$, 1330 cm^{-1} $\delta(\text{C-H})$ and 982 cm^{-1} $\nu(\text{C-C})$ in Figure 6(a), and the little shoulders located near of these bands [30, 36, 37] correspond to vibrations of C-C and C-H bonds in PMMA. The spectrum for the composite with sCNTs shows larger peaks, apparently due to interactions between end moieties in organosilane and the PMMA matrix. The links achieved after polymerization could be C-C and C-H interactions. It is important to indicate that the mentioned bands increase also in the composite with unfunctionalized CNTs with respect to PMMA. Thus, It is corroborated the interactions between open π bonds broken in the polymerization and C-H— π interactions. Both phenomena have been found in PMMA with unfunctionalized carbon nanotubes in a previous study by our group [26] and other research realized by Baskaran et al. [38]. However, the bands are stronger when CNTs are functionalized. This shows that more interactions are achieved between carbon polymer chains with carbon nanotubes when these are functionalized.

Two bands related with C-O vibrations also are found in the IR spectra: in Figure 6(b), the peak at 1737 cm^{-1} $\nu(\text{C=O})$ and in the Figure 6(a) the band localized at 820 cm^{-1} (combination of C-H and C-O-C deformation [26, 36]). Both

peaks correspond to C-O vibrations in PMMA; these signals also are stronger for sCNTs system. Thus, moieties in PMMA which contain carbon and oxygen participate in polymer-nanotube interactions, more so after functionalization.

The last suggestion is corroborated in the Figure 7; the image show a zoomed view of the Figure 6(a). Here the Raman spectra show the region between 1080 cm^{-1} and 1500 cm^{-1} . Peaks at 1139 cm^{-1} and 1200 cm^{-1} which correspond to C-O-C vibrations [26, 38] are seen in PMMA and in the composite with unfunctionalized CNTs. These bands are shifted to 1128 cm^{-1} and 1183 cm^{-1} , respectively in the spectrum of composite with sCNTs; this shift is not seen in the band at 1462 cm^{-1} used as reference in the spectra. Thus, it is inferred that PMMA's ester groups interact with organosilane's ester groups on the CNT surface, producing C=O...OCH₃ and C=O...H interactions that shift the peaks position. Changes in the bands at 1330 cm^{-1} and 1390 cm^{-1} are also evident. The former appears only in the composite spectra and is stronger in the sCNT system. A small shoulder at 1390 cm^{-1} appears only in the PMMA spectrum. Both bands in the overlap region are attributed to C-H deformation; the first peak corresponds to $\delta(\text{C-H methyne})$, and the second is attributed to deformation of C-H (CH₃ or CH₂) in the polymer. In addition, the signal at 1330 cm^{-1} is found in the neighborhood of the D band region which corresponds to CNTs and is related to sp³ hybridization. This suggests that C-C and C-H moieties are produced between C=C methacrylate organosilane groups and the C=C of the monomer in the polymerization. The results are changes in polymer group vibrations due to the formed links when CNTs, particularly functionalized ones, are incorporated. Also some contribution of D band could have some effect in the peak at 1330 cm^{-1} in the nanocomposites.

Returning to Figure 6(c), a peak appears from 2600 cm^{-1} to 2700 cm^{-1} in the sCNT system spectrum and is associated with Si-H bonds found in silanes [34, 39]. It is possible that some Si...H links are created between the organosilane and aliphatic polymer groups. We recall here similarity between C and Si.

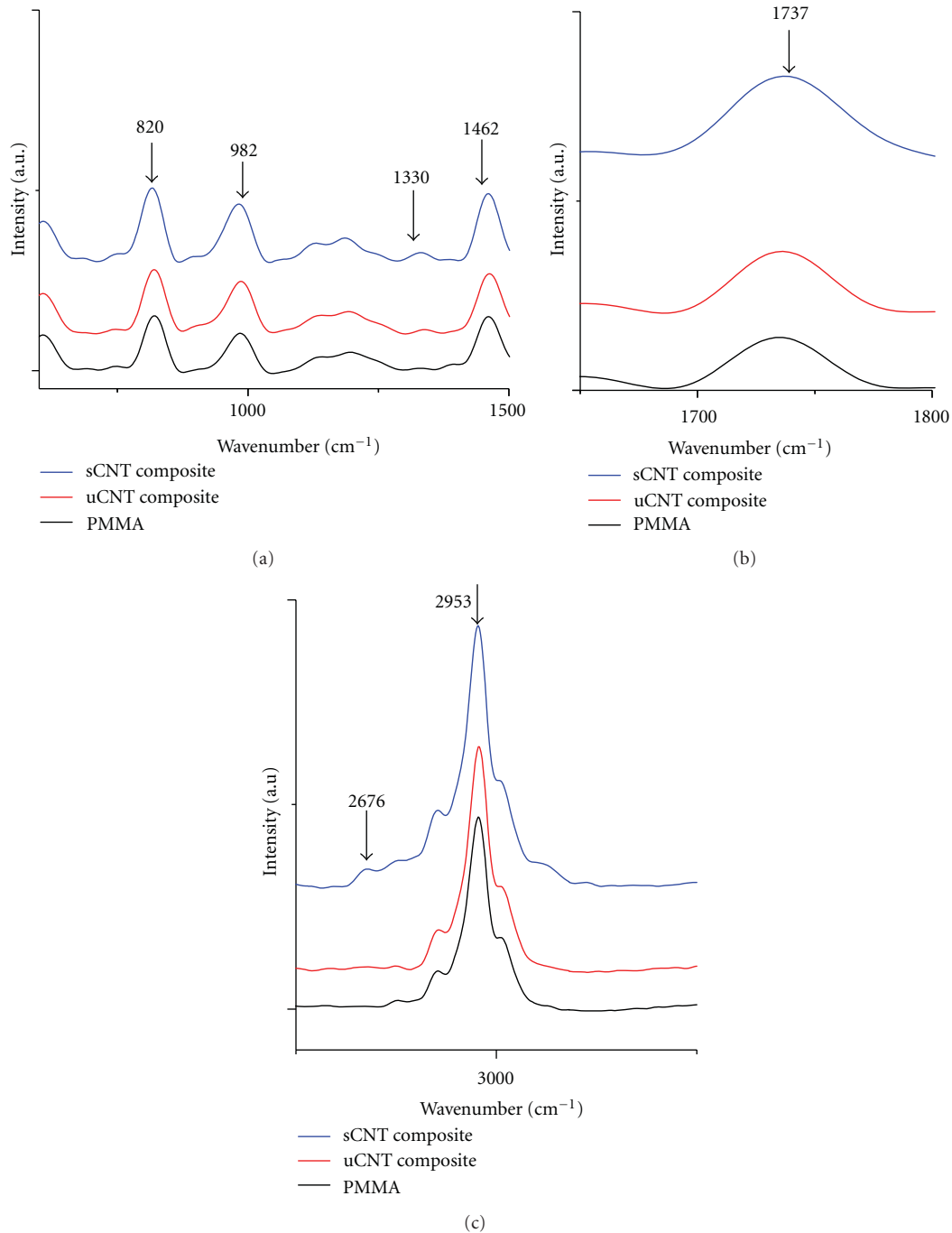


FIGURE 6: Raman spectra of PMMA and carbon nanotube polymer nanocomposites (a) from 600 cm^{-1} to 1500 cm^{-1} , (b) 1650 cm^{-1} to 1800 cm^{-1} , and (c) from 2500 cm^{-1} to 3500 cm^{-1} .

3.5. Scratching Behavior. Figure 8 shows penetration depths as a function applied force achieved in PMMA and nanocomposites. Several tests for each kind of material are shown. PMMA samples show regular behavior which is independent of the material section; inasmuch as, the seven analyses present similar penetration depth at the same loads. Thus, PMMA presents homogenous behavior that indicates similar features in any point of its surface. sCNT composite present two zones; in the region from 7.5 N to 9 N,

the majority of the determinations in sCNT composite present better resistance to be penetrated with respect to PMMA; however, in the zone above 9 N, the majority of these samples show lower resistance to the penetration than PMMA. Nevertheless, the largest part of the analysis realized in sCNT composite presents better tribological properties than uCNT composite. Therefore, although a small quantity of sCNTs is incorporated in polymer; better wear resistance is presented at low load with respect to polymer matrix.

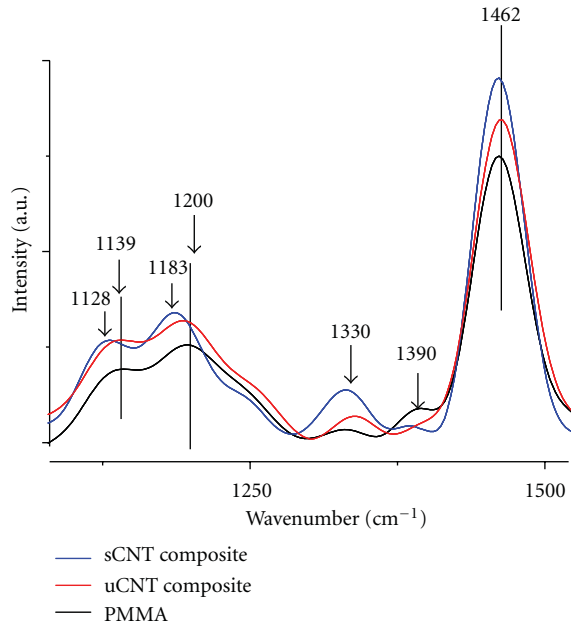


FIGURE 7: Raman spectra of PMMA and carbon nanotube polymer nanocomposites from 1080 cm^{-1} to 1500 cm^{-1} .

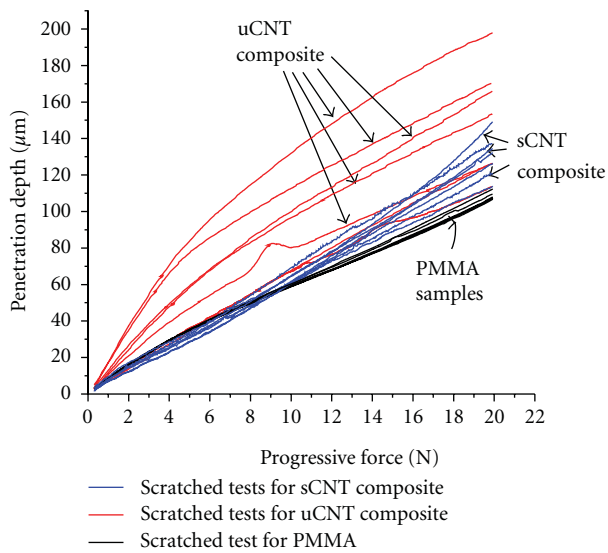


FIGURE 8: Microscratch testing results represented by penetration depth. Black line: Poly(methyl methacrylate) (PMMA), red line: 1 wt% unfunctionalized carbon nanotube polymer nanocomposite (uCNTs composite), blue line: 1 wt% functionalized silanized carbon nanotube polymer nanocomposite (sCNT composite).

Thus, neat PMMA has better scratch resistance than CNT's reinforced materials except for the composite with sCNTs at low forces. In addition, curves show that the behavior of the composite with sCNTs is more uniform than the composite with uCNTs. The fact related with the variety of curves, relatively far apart from each other, can be explained by formation of CNT bundles for uCNT composite. Thus, also in our systems, uniform distribution of CNTs in the

matrix apparently achieved for sCNTs is important. It is supposed that good distribution of silanized carbon nanotubes (sCNTs) results in efficient tribological properties only at low loads as sCNTs could support the mechanical behavior. However, it is possible that the interaction produced between sCNTs and polymer chains could produce shorter chains than those produced in uCNT composites or PMMA. Thus, shorter chains at high loads could produce easy penetration in the material. As discussed by Dzenis [4], CNTs can produce improvement as well as worsening of the properties of matrices. This depends on diverse factors involved in the modification and synthesis of the nanocomposites.

3.6. General Discussion. Successful silanization of carbon nanotubes is useful for changing their surface behavior and, therefore, their dispersion in organic solvents. Substituents in the organosilane, here, play an important role.

When using 3-MAT, sCNT surfaces seem to have a variety of interactions with the PMMA matrix: $C-C$, $C=C \cdots \pi$, $C=O \cdots O$, $C=O \cdots H$ and $Si \cdots H$. The majority of these interactions begin in the polymerization.

The links produced in nanocomposites play an important role to improve thermomechanical properties in these materials, in as much as, storage modulus (E') at different temperatures increase notably in the composites with sCNTs with respect to the composite with uCNTs and PMMA. In addition, the glass transition temperature is increased around 31°C in the composite with sCNTs with respect to polymer matrix, in comparison with uCNT system where T_g only increase by 10°C .

In other works moderate increments in mechanical properties have been achieved in PMMA matrix or copolymers using MMA when uCNTs have been incorporated, for instance with very low loads (0.01 wt%) of SWMTs, and MWNTs have improved tensile modulus of polymer matrix [9], and storage modulus E' has been enhanced with 1 wt% of MWNTs using dissolving processing [13]. In addition other processing methods which involve uCNTs with other polymer matrices have reached good increments in storage modulus when uCNTs are aligned [9]. Nevertheless when CNTs are modified by oxidation [26], cover by polymers [27], or functionalized using other molecules [25, 27], better results have been reached in mechanical and thermal properties.

Recently, silanization have been an important route to modify CNTs, and the results agree with the thermomechanical properties reported here. Important increments in tensile strength in Poly(propylene) (PP) and polyimide (PI) matrices [40, 41] and thermal stability in epoxy matrix [42] have been gotten at 1 wt% of sCNTs (PP and PI) and 0.5 wt% (in the case of epoxy matrix). The silanes used in these researches were 3-methacryloxypropyltrimethoxysilane, vinyltriethoxysilane, and 3-Glycidoxypropyltrimethoxysilane, respectively. Also in recent times interesting dielectric properties have been reported in polyethylene reinforced with carbon nanofibers modified with silanes [43]. Thus, it is corroborated that silane functionalization in CNTs is useful to improve interface and thermomechanical

properties in different polymer matrices including PMMA studied in this paper.

Also, functionalization effect is reflected in tribological properties; however, other factors such as the polymer chain sizes and the low concentration of sCNTs could influence the different behavior in tribological properties at low and high force. Nevertheless, the clear differences in the tribological behavior between sCNT and uCNT composites give evidence that silanization takes part in this property; the evidence of that influence is the low quantity used as reinforcement of sCNTs and the notable effect. The curves of penetration depth and progressive force are more consistent in the composite which contains more sCNTs than that in the composite with uCNTs. This allows concluding that functionalization, furthermore, assists the dispersion of carbon nanotubes in polymer composite.

Thus, this research gives evidence that the synergic effects produced in polymer composites are reached by interactions between organosilane chemical groups of modified nanotubes and polymer matrix. The incorporation of a small quantity of sCNTs is enough to produce significant changes at polymer matrix; even uCNTs provide considerable changes in polymer, taking into account the CNT quantity that is added; as well functionalization provides to the composites extra qualities, because of not only improving storage modulus and T_g , also uniform behavior is observed in any point of the sample when tribological properties are analyzed. These characteristics confer to this kind of nanocomposites' additional functional properties and the possibility to be incorporated in promising uses such as transportation industry, commercial aircraft, sports industry, and textile smart polymer fibers among others possible applications. Research using different concentrations of CNTs and other organosilanes with other R group related to the features of the polymer matrices is in current study.

Acknowledgments

The authors are grateful to Dr. G. Hernández-Padron for her assistance in the IR analysis and to CINVESTAV Querétaro, particularly Dr. S. Jimenez and Mr. F. Rodríguez for their assistance in Raman measurements. Financial support has been provided by the American Chemical Society, Washington, DC, the Mexican National Academy of Sciences (AMC), Mexico City, the DGEST under project DGEST 2006 333.06, and the Consejo Nacional de Ciencia y Tecnología (CONACyT), Mexico City under project JI-58232.

References

- [1] M. Zhang, K. R. Atkinson, and R. H. Baughman, "Multi-functional carbon nanotube yarns by downsizing an ancient technology," *Science*, vol. 306, no. 5700, pp. 1358–1361, 2004.
- [2] C. Velasco-Santos, A. L. Martínez-Hernández, and V. M. Castaño, "Carbon nanotube-polymer nanocomposites: the role of interfaces," *Composite Interfaces*, vol. 11, no. 8-9, pp. 567–586, 2005.
- [3] C. Velasco-Santos, A. L. Martínez-Hernández, and V. M. Castaño, "Carbon nanotube-polymer nanocomposites: principles and applications," in *Focus on Nanotube Research*, D. A. Martin, Ed., vol. 1, pp. 97–126, Nova Science Publishers, Huntington, NY, USA, 2006.
- [4] Y. Dzenis, "Materials science: structural nanocomposites," *Science*, vol. 319, no. 5862, pp. 419–420, 2008.
- [5] M. M. Treacy, T. W. Ebbesen, and J. M. Gibson, "Exceptionally high Young's modulus observed for individual carbon nanotubes," *Nature*, vol. 381, no. 6584, pp. 678–680, 1996.
- [6] J. Hone, M. Whitney, C. Piskoti, and A. Zettl, "Thermal conductivity of single-walled carbon nanotubes," *Physical Review B: Condensed Matter & Materials Physics*, vol. 59, no. 4, pp. R2514–R2516, 1999.
- [7] T. W. Ebbesen, H. J. Lezec, H. Hiura, J. W. Bennett, H. F. Ghaemi, and T. Thio, "Electrical conductivity of individual carbon nanotubes," *Nature*, vol. 382, no. 6586, pp. 54–56, 1996.
- [8] J.-P. Salvetat, J.-M. Bonard, N. H. Thomson et al., "Mechanical properties of carbon nanotubes," *Applied Physics A: Materials Science and Processing*, vol. 69, no. 3, pp. 255–260, 1999.
- [9] C. A. Cooper, D. Ravich, D. Lips, J. Mayer, and H. D. Wagner, "Distribution and alignment of carbon nanotubes and nanofibrils in a polymer matrix," *Composites Science and Technology*, vol. 62, no. 7-8, pp. 1105–1112, 2002.
- [10] C. Velasco-Santos, A. L. Martínez-Hernández, and V. M. Castaño, "Nanocomposites," in *Proceedings of the NanoTech Conference Technical Proceedings (NSTI '05)*, vol. 2, p. 139, Anaheim, Calif, USA, 2005.
- [11] L. Valentini, J. Biagiotti, J. M. Kenny, and M. A. López Manchado, "Physical and mechanical behavior of single-walled carbon nanotube/polypropylene/ethylene-propylenediene rubber nanocomposites," *Journal of Applied Polymer Science*, vol. 89, no. 10, pp. 2657–2663, 2003.
- [12] H. Zhang and Z. Zhang, "Impact behaviour of polypropylene filled with multi-walled carbon nanotubes," *European Polymer Journal*, vol. 43, no. 8, pp. 3197–3207, 2007.
- [13] C. Velasco-Santos, A. L. Martínez-Hernández, F. Fisher, R. S. Ruoff, and V. M. Castaño, "Dynamicalmechanical and thermal analysis of carbon nanotube-methylethyl methacrylate nanocomposites," *Journal of Physics D: Applied Physics*, vol. 36, no. 12, pp. 1423–1428, 2003.
- [14] H. Xia and M. Song, "Preparation and characterization of polyurethane-carbon nanotube composites," *Soft Matter*, vol. 1, no. 5, pp. 386–394, 2005.
- [15] Y.-K. Choi, Y. Gotoh, K. Sugimoto, S.-M. Song, T. Yanagisawa, and M. Endo, "Processing and characterization of epoxy nanocomposites reinforced by cup-stacked carbon nanotubes," *Polymer*, vol. 46, no. 25, pp. 11489–11498, 2005.
- [16] L. F. Giraldo, W. Brostow, E. Devaux, B. L. López, and L. D. Pérez, "Scratch and wear resistance of polyamide 6 reinforced with multiwall carbon nanotubes," *Journal of Nanoscience and Nanotechnology*, vol. 8, no. 6, pp. 3173–3183, 2008.
- [17] A. Allaoui, H. Bai, M. Cheng, and J. B. Bai, "Mechanical and electrical properties of a MWNT/epoxy composite," *Composites Science and Technology*, vol. 62, no. 15, pp. 1993–1998, 2002.
- [18] J. Sandler, M. S. P. Shaffer, T. Prasse, W. Bauhofer, K. Schulte, and A. H. Windle, "Development of a dispersion process for carbon nanotubes in an epoxy matrix and the resulting electrical properties," *Polymer*, vol. 40, no. 21, pp. 5967–5971, 1999.
- [19] J. K. W. Sandler, J. E. Kirk, I. A. Kinloch, M. S. P. Shaffer, and A. H. Windle, "Ultra-low electrical percolation threshold in

- carbon-nanotube-epoxy composites," *Polymer*, vol. 44, no. 19, pp. 5893–5899, 2003.
- [20] Y. J. Kim, T. S. Shin, H. D. Choi, J. H. Kwon, Y.-C. Chung, and H. G. Yoon, "Electrical conductivity of chemically modified multiwalled carbon nanotube/epoxy composites," *Carbon*, vol. 43, no. 1, pp. 23–30, 2005.
- [21] J. Suhr, N. Koratkar, P. Koblinski, and P. Ajayan, "Viscoelasticity in carbon nanotube composites," *Nature Materials*, vol. 4, no. 2, pp. 134–137, 2005.
- [22] J. W. Cho, J. W. Kim, Y. C. Jung, and N. S. Goo, "Electroactive shape-memory polyurethane composites incorporating carbon nanotubes," *Macromolecular Rapid Communications*, vol. 26, no. 5, pp. 412–416, 2005.
- [23] J. D. W. Madden, N. A. Vandesteeg, P. A. Anquetil et al., "Artificial muscle technology: physical principles and naval prospects," *IEEE Journal of Oceanic Engineering*, vol. 29, no. 3, pp. 706–728, 2004.
- [24] W. Brostow, J.-L. Deborde, M. Jaklewicz, and P. Olszynski, "Tribology with emphasis on polymers: friction, scratch resistance and wear," *Journal of Materials Education*, vol. 25, pp. 119–126, 2003.
- [25] M. C. Paiva, B. Zhou, K. A. S. Fernando et al., "Physical and mechanical characterization of nanocomposites with carbon nanotubes functionalized with the matrix polymer," *Composite Interfaces*, vol. 12, no. 8-9, pp. 757–768, 2005.
- [26] C. Velasco-Santos, A. L. Martínez-Hernández, F. T. Fisher, R. Ruoff, and V. M. Castaño, "Improvement of thermal and mechanical properties of carbon nanotube composites through chemical functionalization," *Chemistry of Materials*, vol. 15, no. 23, pp. 4470–4475, 2003.
- [27] M. Wang, K. P. Pramoda, and S. H. Goh, "Enhancement of the mechanical properties of poly(styrene-co-acrylonitrile) with poly(methyl methacrylate)-grafted multiwalled carbon nanotubes," *Polymer*, vol. 46, no. 25, pp. 11510–11516, 2005.
- [28] C. Velasco-Santos, A. L. Martínez-Hernández, M. Lozada-Cassou, A. Alvarez-Castillo, and V. M. Castaño, "Chemical functionalization of carbon nanotubes through an organosilane," *Nanotechnology*, vol. 13, no. 4, pp. 495–498, 2002.
- [29] J. Kastner, T. Pichler, H. Kuzmany et al., "Resonance Raman and infrared spectroscopy of carbon nanotubes," *Chemical Physics Letters*, vol. 221, no. 1-2, pp. 53–58, 1994.
- [30] J. Coates, "Interpretation of infrared spectra, a practical approach," in *Encyclopedia of Analytical Chemistry*, R. A. Meyers, Ed., pp. 10815–10837, John Wiley & Sons, Chichester, UK, 2000.
- [31] J. Zhang, H. Zou, Q. Qing et al., "Effect of chemical oxidation on the structure of single-walled carbon nanotubes," *Journal of Physical Chemistry B*, vol. 107, no. 16, pp. 3712–3718, 2003.
- [32] J. Chen, A. M. Rao, S. Lyuksyutov et al., "Dissolution of full-length single-walled carbon nanotubes," *Journal of Physical Chemistry B*, vol. 105, no. 13, pp. 2525–2528, 2001.
- [33] P. C. Ma, J.-K. Kim, and B. Z. Tang, "Functionalization of carbon nanotubes using a silane coupling agent," *Carbon*, vol. 44, no. 15, pp. 3232–3238, 2006.
- [34] E. Bourgeat-Lami, I. Tissot, and F. Lefebvre, "Synthesis and characterization of SiOH-functionalized polymer latexes using methacryloxy propyl trimethoxysilane in emulsion polymerization," *Macromolecules*, vol. 35, no. 16, pp. 6185–6191, 2002.
- [35] E. F. Lucas, B. G. Soares, and E. Monteiro, *Caracterização de Polímeros, Determinação de peso Molecular e Análise Térmica, E-Papers*, Rio de Janeiro, Brazil, 2001.
- [36] A. L. Martínez-Hernández, C. Velasco-Santos, M. de Lcaza, and V. M. Castaño, "Grafting of methyl methacrylate onto natural keratin," *e-Polymers*, no. 016, pp. 1–11, 2003.
- [37] A. Matsushita, Y. Ren, K. Matsukawa et al., "Two-dimensional Fourier-transform Raman and near-infrared correlation spectroscopy studies of poly(methyl methacrylate) blends. 1. Immiscible blends of poly(methyl methacrylate) and atactic polystyrene," *Vibrational Spectroscopy*, vol. 24, no. 2, pp. 171–180, 2000.
- [38] D. Baskaran, J. W. Mays, and M. S. Bratcher, "Noncovalent and nonspecific molecular interactions of polymers with multiwalled carbon nanotubes," *Chemistry of Materials*, vol. 17, no. 13, pp. 3389–3397, 2005.
- [39] R. W. Hannah and D. W. Mayo, "Introduction in courses notes in the interpretation of infrared and raman spectra," in *Infrared Spectra of Polymers*, D. Mayo, F. Miller, and R. Hannah, Eds., p. 261, John Wiley & Sons, Chichester, UK, 2003.
- [40] Z. Zhou, S. Wang, L. Lu, Y. Zhang, and Y. Zhang, "Functionalization of multi-wall carbon nanotubes with silane and its reinforcement on polypropylene composites," *Composites Science and Technology*, vol. 68, no. 7-8, pp. 1727–1733, 2008.
- [41] S.-M. Yuen, C.-C. M. Ma, C. L. Chiang, C.-C. Teng, and Y.-H. Yu, "Poly(vinyltriethoxysilane) modified MWCNT/polyimide nanocomposites—preparation, morphological, mechanical, and electrical properties," *Journal of Polymer Science, Part A*, vol. 46, no. 3, pp. 803–816, 2008.
- [42] P. Cheng, J.-K. Kim, and B.-Z. Tang, "Effects of silane functionalization on the properties of carbon nanotube/epoxy nanocomposites," *Composites Science and Technology*, vol. 67, no. 14, pp. 2965–2972, 2007.
- [43] T. Liu, W. Wood, and W.-H. Zhong, "Sensitivity of Dielectric Properties to Wear Process on Carbon Nanofiber/High-Density Polyethylene Composites," *Nanoscale Research Letters*, vol. 6, no. 1, pp. 1–9, 2011.

Research Article

Nanofibrous Resonant Membrane for Acoustic Applications

K. Kalinová

Department of Nonwovens, Faculty of Textile Engineering, Technical University of Liberec, Studentská 2, 46117 Liberec, Czech Republic

Correspondence should be addressed to K. Kalinová, klara.kalinova@tul.cz

Received 16 May 2011; Accepted 22 July 2011

Academic Editor: Sadhan C. Jana

Copyright © 2011 K. Kalinová. This is an open access article distributed under the Creative Commons Attribution License, which permits unrestricted use, distribution, and reproduction in any medium, provided the original work is properly cited.

Because the absorption of lower-frequency sound is problematic with fibrous material made up of coarser fibers, highly efficient sound absorption materials must be developed. The focus of this paper is on the development of a new material with high acoustic absorption characteristics. For low-frequency absorption, structures based upon the resonance principle of nanofibrous layers are employed in which the resonance of some elements allows acoustic energy to be converted into thermal energy. A nanofibrous membrane was produced by an electrostatic spinning process from an aqueous solution of polyvinyl alcohol and the acoustic characteristics of the material measured. The resonant frequency prediction for the nanofibrous membrane is based on research into its production parameters. The distance between electrodes during the electrostatic spinning process determines the average diameter of the nanofibers, and the outlet velocity of the material determines its area density. The average diameter of nanofibers was measured using the Lucia software package directly from an electron microscope image. The resonant frequency of nanofibrous membranes was determined from the sound absorption coefficient and transmission loss measurement.

1. Introduction

This paper deals with the acoustic behavior of a nanofibrous resonant membrane. A nanofibrous layer was produced by an electrical spinning process from an aqueous solution of polyvinyl alcohol and the resonance effect created by the nanofibrous layer then studied. Acoustic waves cause vibration in the resonant nanofibrous system with acoustic energy at the resonance frequency partially converted to kinetic energy, the remainder being acoustic energy at other frequencies. These frequencies are damped so that the majority of the acoustic energy, accumulated in the resonator, may be converted into heat.

This theoretical study of sound absorption characteristics [1] focuses on a membrane-type sound absorber. To analyze the absorption mechanism, the solution is rearranged in a form which points out the contribution from each element in the membrane-type sound absorber. The effects of the parameters of the sound absorption system are discussed in the light of the calculated results. In addition, the method used for predicting peak frequency and the peak value of the oblique-incident absorption coefficient of the membrane-type sound absorber is presented. This method satisfactorily

explains the relationship between the absorption characteristics and the parameters.

A sound-absorbing structure using thin film is described in a patent [2]. When a soundwave makes contact with the sound-absorbing structure of the invention, the thin films vibrate and contacts between the overlapping portions rub against each other. The energy contained in the soundwave dissipates as a result, and a high sound absorption coefficient over a broad frequency band is obtained. The sound absorption effect is intensified by the addition of the damping effect as the soundwave passes through the interstices.

Because the absorption of lower-frequency sound is problematic with fibrous material made up of coarser fibers, highly efficient sound absorption materials must be developed. The focus of this paper is therefore on the development of a new material with high acoustic absorption characteristics.

Previous work [3, 4] has shown this nanofibrous material to be a highly efficient sound absorber. For low-frequency absorption, structures based upon the resonance principle are employed in which the resonance of some elements allows acoustic energy to be converted into thermal energy. Earlier work [3] has demonstrated that the nanofibrous

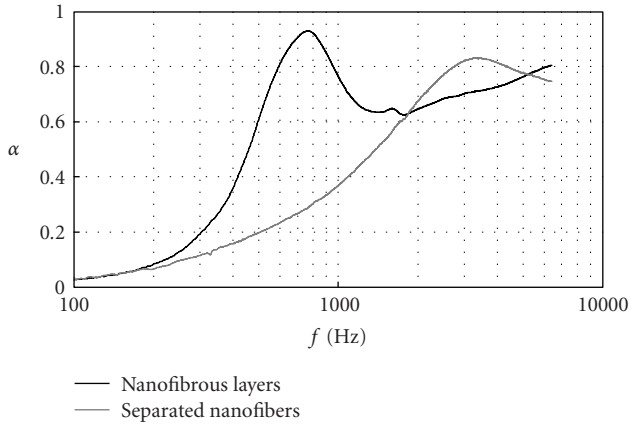


FIGURE 1: Frequency dependence of sound absorption coefficient α . Nanofibers creating a layer (black curve) and nanofibers distributed separately in the sample (grey curve). The final thickness of both materials is 30 mm, with a bulk density of 21 kg/m^{-3} .

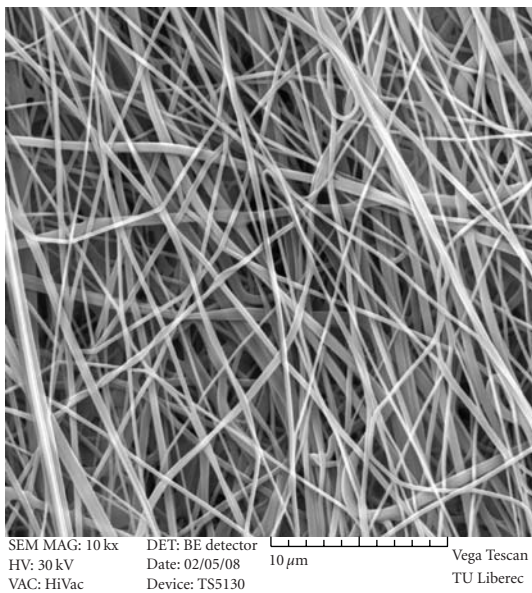


FIGURE 2: Snapshot of the nanofibrous structure.

layer has a resonant effect on sound absorption when the nanofibers are arranged with respect to the layer. Then the tops of sound absorption coefficient are displaced to the lower frequencies than those of sample with nanofibers distributed separately (see Figure 1).

The sound absorption peaks of longitudinally laid samples occur at frequencies lower than those of samples laid perpendicularly [4].

This is attributable to motion in the nanofibrous layer. When the longitudinal soundwave propagates perpendicularly to the alignment of the membrane, the nanolayer is able to move and changes in acoustic energy may occur. The second effect is due to the viscosity of the surrounding air, where acoustic energy is consumed by the drag between

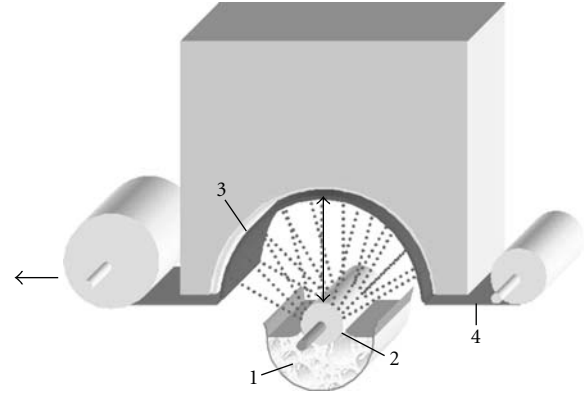


FIGURE 3: A device for the production of nanofibers from a polymer solution. The polymer solution (1) wets the cylindrical electrode (2). This electrode is matched with a counter electrode (3) whose potential differs. By rotating electrode (2), the polymer solution is drawn from the container into the counter electrode. The nanofibers form in the electrical field and are deposited on the support material (4). The electrode distance during electrostatic spinning and the outlet velocity of the material, which controls its area, may be altered.

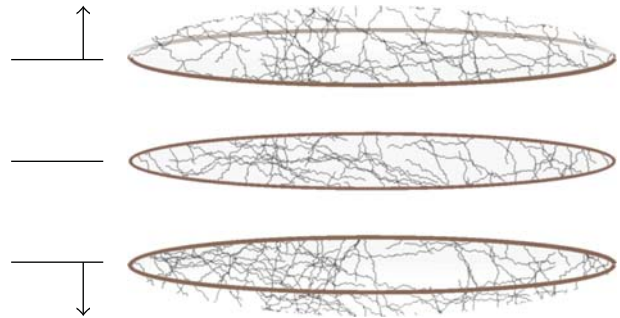


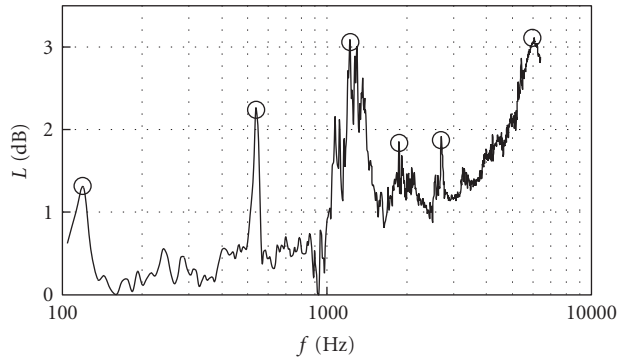
FIGURE 4: Nanofibrous membrane vibration at the first resonant frequency.

vibrating air particles and the pore surface, converting the acoustic energy into thermal energy. These two nanofibrous layer phenomena together constitute the innovation of this acoustic product compared to current materials used for sound absorption such as foil and fibrous board.

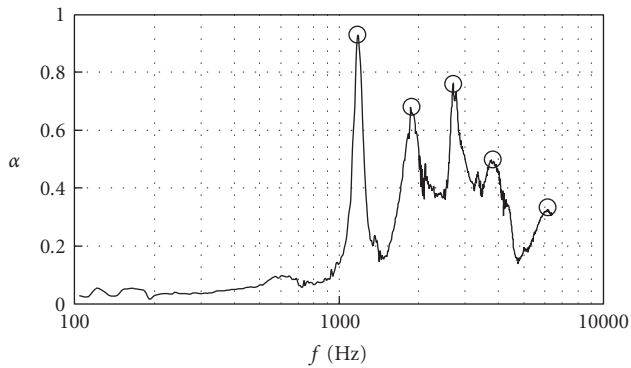
2. Experimental

The nanofibrous membrane was produced by an electrostatic spinning process from an aqueous solution of polyvinyl alcohol (see Figure 2), and two acoustic characteristics of the material, the sound absorption coefficient and the transmission loss, were measured. In this case, the nanofibrous membrane was created without any support materials from an aqueous solution, but a nonsoluble solution may also be used to produce a nanofibrous membrane possessing the same parameters and physical characteristics.

Two production parameters, the electrode distance during the electrostatic spinning process and the outlet velocity

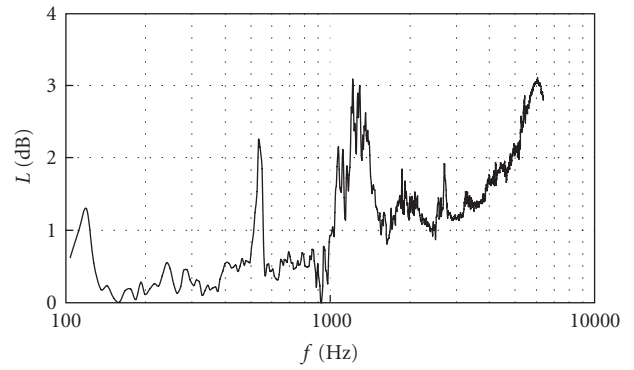


(a)

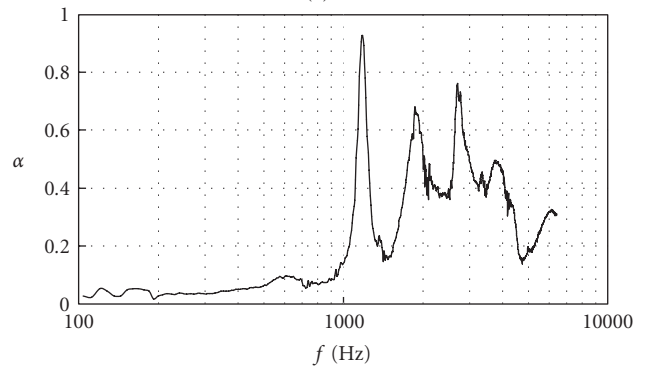


(b)

FIGURE 5: Frequency dependence of transmission loss L (dB) with denoted resonant peaks (a) and frequency dependence of sound absorption coefficient α with denoted resonant peaks (b).

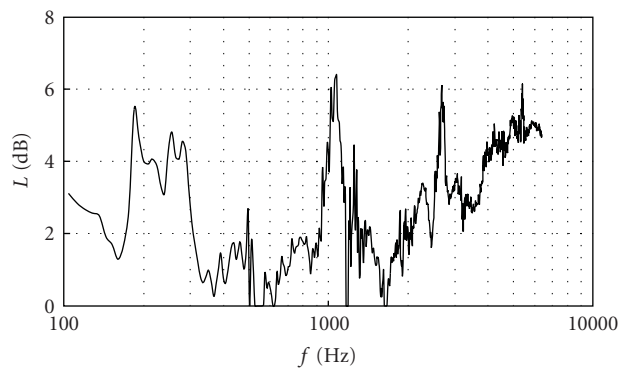


(a)

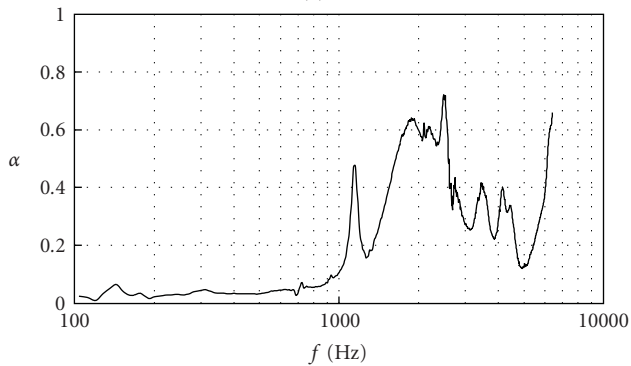


(b)

FIGURE 7: Measured frequency dependence of transmission loss L (dB) (a) and sound absorption coefficient α (b). The area density of the nanofibrous layer is $17.2 \text{ g}\cdot\text{m}^{-2}$.

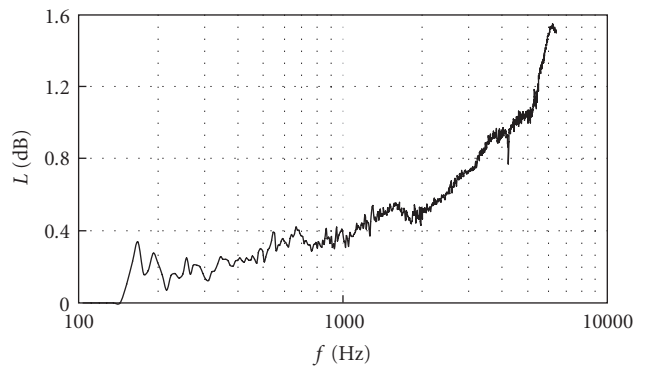


(a)

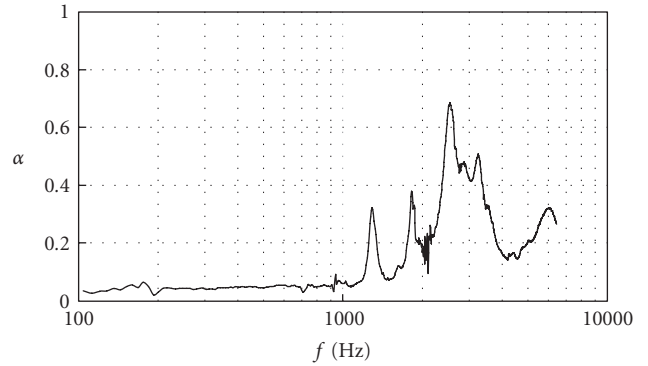


(b)

FIGURE 6: Measured frequency dependence of transmission loss L (dB) (a) and sound absorption coefficient α (b). The area density of the nanofibrous layer is $28.8 \text{ g}\cdot\text{m}^{-2}$.



(a)



(b)

FIGURE 8: Measured frequency dependence of transmission loss L (dB) (a) and sound absorption coefficient α (b). The area density of the nanofibrous layer is $6.3 \text{ g}\cdot\text{m}^{-2}$.

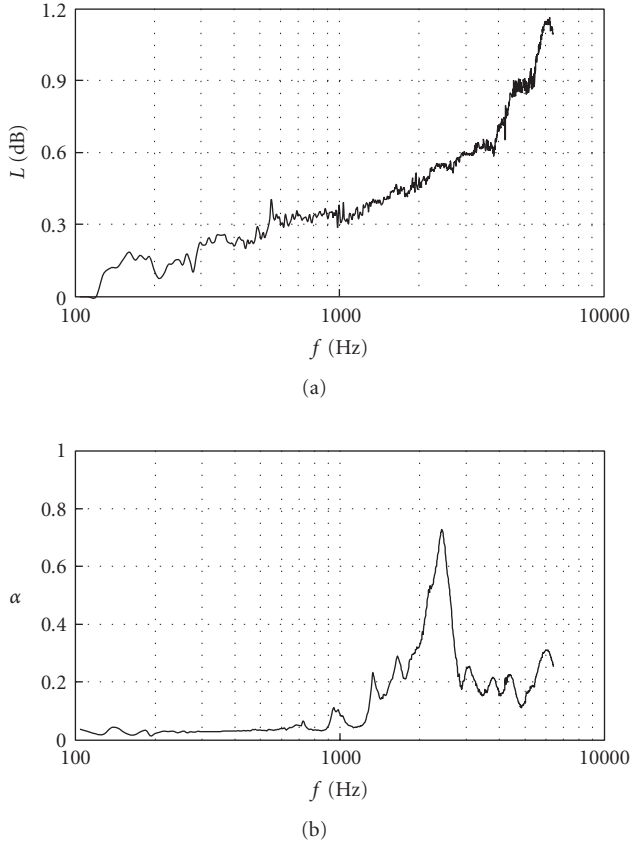


FIGURE 9: Measured frequency dependence of transmission loss L (dB) (a) and sound absorption coefficient α (b). The area density of the nanofibrous layer is $4.8 \text{ g}\cdot\text{m}^{-2}$.

of the material, which controls its area density, were altered (see Figure 3). Changes in the nanofibrous layer structure in terms of specific anisotropy and the diameter of the nanofibers are the result of the electrode distance setting.

A Type 4206 Impedance Measurement Tube featuring dual microphones was used to measure the sound absorption coefficient and transmission loss in the 50 Hz–6.4 kHz range.

In this experimental section, the resonant frequencies from the sound absorption coefficient and transmission loss measurement are compared. The maximum value of the sound absorption coefficient and transmission loss occurs along the resonant frequency of the thin membrane. Soundwaves vibrate the resonant nanofibrous system, with acoustic energy at the resonant frequency (see Figure 4) then partially converted to kinetic energy, the remainder being acoustic energy at other frequencies. These frequencies are damped so that the majority of the acoustic energy, accumulated in the resonator, may be converted to heat.

Resonant frequencies are labeled with circles in Figure 5.

The resonant frequency of nanofibrous membranes was determined from the sound absorption coefficient and transmission loss measurement. Two dependency relationships were studied to determine the resonant frequency.

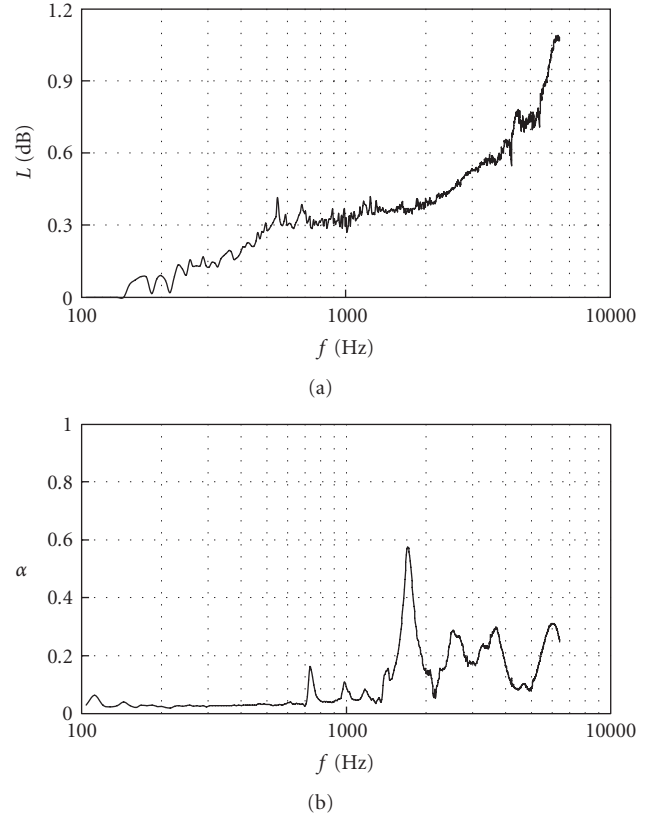


FIGURE 10: Measured frequency dependence of transmission loss L (dB) (a) and sound absorption coefficient α (b). The area density of the nanofibrous layer is $3.3 \text{ g}\cdot\text{m}^{-2}$.

TABLE 1: Production parameter during electrostatic spinning. Outlet velocity of material determining its area density.

Outlet velocity of nanofibrous material during electrostatic spinning ($\text{m}\cdot\text{min}^{-1}$)	Area density of the nanofibrous layer ($\text{g}\cdot\text{m}^{-2}$)
0.0171	28.8
0.0342	17.2
0.0855	6.3
0.1197	4.8
0.171	3.3

3. Results

In this section, the results measured for the frequency dependence of sound absorption coefficient α and transmission loss L (dB) are compared. The outlet velocity of the material determines its area density (see Table 1) and the distance between electrodes during the electrostatic spinning process determines the average diameter of the nanofibers (see Table 2).

3.1. Electrode Distance Constant (50 mm) with Changing Area Density of the Nanofibrous Membrane. From Figures 6, 7, 8, 9, and 10 (a), it is evident that the maximum value for transmission loss L (dB) decreases with decreasing

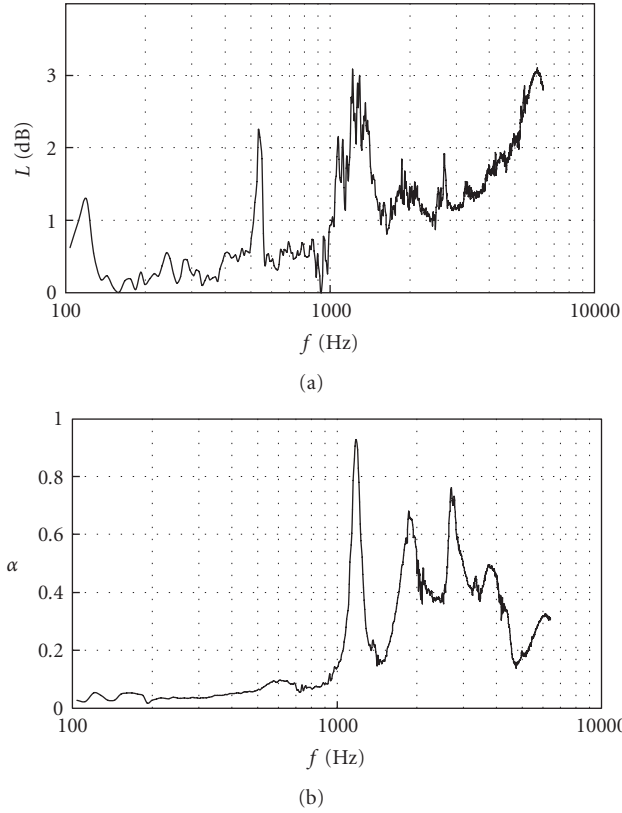


FIGURE 11: Measured frequency dependence of transmission loss L (dB) (a) and sound absorption coefficient α (b). The electrode distance is 50 mm.

TABLE 2: Production parameter during electrostatic spinning. Distance of electrodes during electrostatic spinning which determines the average diameter of nanofibers.

Distance of electrodes during electrostatic spinning (mm)	Average diameter of nanofibers (nm)
50	79.9
70	77.6
90	76.3
110	73.3
130	68.6

area density of the nanofibrous membrane. The resonant frequencies of the lower area density of the membrane (see Figures 8–10 (a)) are not uniquely determined.

Figures 6–10 (b) show that the first significant peak in the sound absorption coefficient α has been displaced in the direction of lower frequencies with increasing area density of the material, when the average nanofiber diameter (the electrode distance during electrostatic spinning) is held constant. The resonant frequency of the nanofibrous membrane thus decreases with the area density of the nanofibrous membrane.

Comparing results from the examination of both acoustic characteristics (see Figures 6–10, with transmission loss

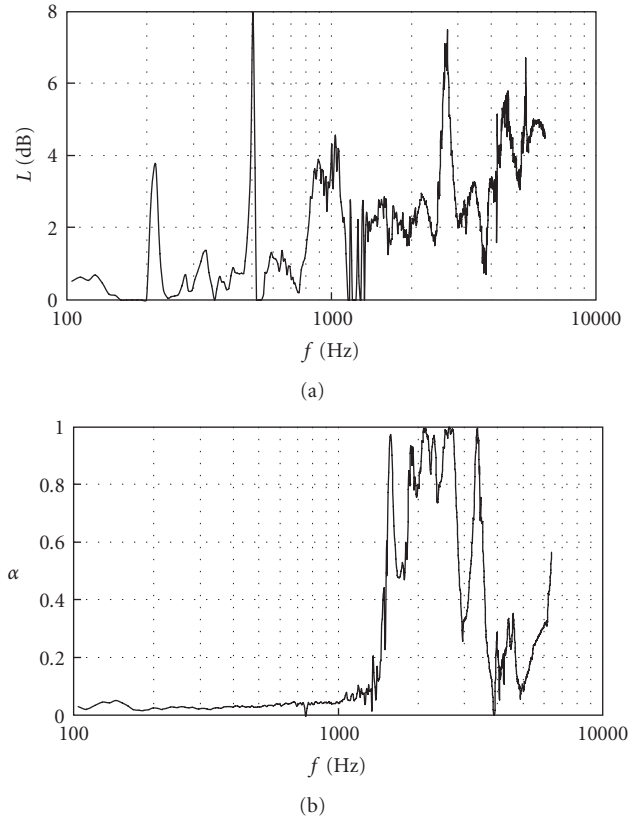


FIGURE 12: Measured frequency dependence of transmission loss L (dB) (a) and sound absorption coefficient α (b). The electrode distance is 90 mm.

L (dB) (a) and the sound absorption coefficient α (b)) shows that the resonant frequencies are not in agreement. The peaks occurring under each measurement are formed at different frequencies.

3.2. Area Density of the Nanofibrous Membrane is Constant ($17.2 \text{ g}\cdot\text{m}^{-2}$) with Changing Electrode Distance. Figures 11, 12, 13, and 14 (b) show that the first significant peak in the sound absorption coefficient α has been displaced in the direction of higher frequencies with decreasing average nanofiber diameter (increasing electrode distance during electrostatic spinning) when the area density of the material is held constant. The resonant frequency of the nanofibrous membrane thus increases with decreasing average nanofiber diameter.

Comparing results from the examination of both acoustic characteristics (see Figures 11–14, with transmission loss L (dB) (a) and the sound absorption coefficient α (b)) shows that the resonant frequencies are not in agreement. The peaks occurring under each measurement are formed at different frequencies.

The measurement of transmission loss shows two peaks, one at 530 Hz and one at 2700 Hz, for all measurements using constant area density (see Figures 11–14 (a)). 530 Hz and 2700 Hz would thus be resonant frequencies of the measuring apparatus during transmission loss measurement.

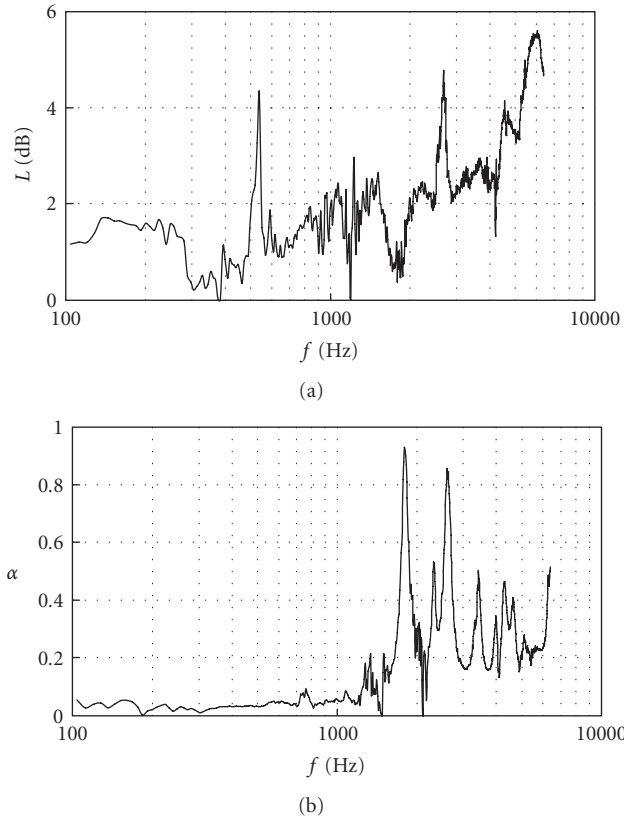


FIGURE 13: Measured frequency dependence of transmission loss L (dB) (a) and sound absorption coefficient α (b). The electrode distance is 110 mm.

One peak is constant for all measurements using both dependencies and both acoustic characteristics measured (see Figures 6, 7, and 11–14). The resonant frequency of the measuring apparatus while measuring both acoustic characteristics is around 2700 Hz.

4. Conclusions

These two phenomena, the vibration of the nanolayer and air friction inside the nanopores, constitute the innovation of this acoustic product compared to current materials used for sound absorption such as foil and fibrous board.

Sound absorption coefficient measurements show that the resonant frequency of the nanofibrous membrane decreases with increasing area density of the membrane and increases with decreasing average diameter of the nanofibers.

Comparing results from the examination of both acoustic characteristics (transmission loss L (dB) and the sound absorption coefficient α) shows that the resonant frequencies are not in agreement. The peaks occurring under each measurement are formed at different frequencies.

The transmission loss measurement shows that 530 Hz and 2700 Hz would be the resonant frequencies of the measuring apparatus during transmission loss measurement.

One peak is constant for all measurements using both dependencies and both acoustic characteristics measured.

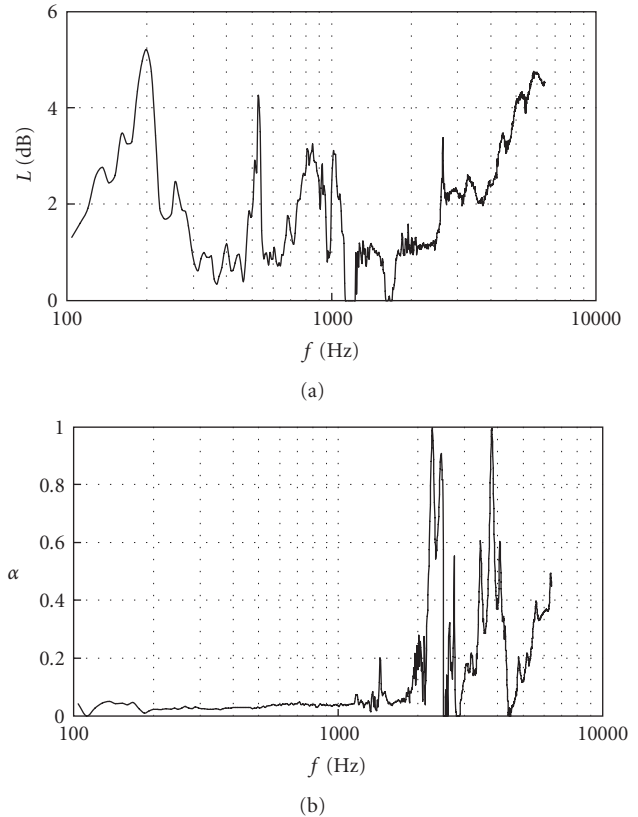


FIGURE 14: Measured frequency dependence of transmission loss L (dB) (a) and sound absorption coefficient α (b). The electrode distance is 130 mm.

The resonant frequency of the measuring apparatus while measuring both acoustic characteristics is around 2700 Hz.

Acknowledgement

The contribution was sponsored by the postdoctoral project of the Czech Science Foundation (GAČR), 106/07/P044 Transport and Absorption of Sound in Nanofibres Assemblies.

References

- [1] K. Sakagami, M. Kiyama, M. Morimoto, and D. Takahashi, "Sound absorption of a cavity-backed membrane: a step towards design method for membrane-type absorbers," *Applied Acoustics*, vol. 49, no. 3, pp. 237–247, 1996.
- [2] Z. Yamaguchi et al., "A sound-absorbing structure using thin film," EP1598808, 2005-11-23.
- [3] K. Kalinová and O. Jirsák, "Resonance effect of nanofibrous layer," in *Proceedings of the 5th Autex World Textile Conference*, Portorož, Slovenia, 2005.
- [4] K. Kalinová, "Influence of nanofibrous membrane configuration on the sound absorption coefficient and resonant frequency," in *Proceedings of the 6th Autex World Textile Conference*, Raleigh, NC, USA, 2006.

Research Article

Electrical Properties of Zn-Phthalocyanine and Poly (3-hexylthiophene) Doped Nematic Liquid Crystal

Y. Karakuş,¹ M. Okutan,² A. Kösemen,³ S. E. San,⁴ Z. Alpaslan,⁴ and A. Demir⁴

¹Department of Physics, Sakarya University, Esentepe Campus, 54187 Sakarya, Turkey

²Department of Physics, Yıldız Technical University, Davutpaşa, 34210 Istanbul, Turkey

³Department of Physics, Muş Alparslan University, 49100 Muş, Turkey

⁴Department of Physics, Gebze Institute of Technology, Gebze, 41400 Kocaeli, Turkey

Correspondence should be addressed to M. Okutan, mokutan@gmail.com

Received 19 April 2011; Revised 24 June 2011; Accepted 10 July 2011

Academic Editor: Gaurav Mago

Copyright © 2011 Y. Karakuş et al. This is an open access article distributed under the Creative Commons Attribution License, which permits unrestricted use, distribution, and reproduction in any medium, provided the original work is properly cited.

An E7 coded nematic liquid crystal was doped with zinc phthalocyanine and poly (3-hexylthiophene). A variety of properties including relaxation time, absorption coefficient, and critical frequency of this doped system were investigated using impedance spectroscopy. The doped systems displayed increased absorption coefficients in the range 0.22–0.55 and relaxation times from 5.05×10^{-7} s to 3.59×10^{-6} s with a decrease in the critical frequency from 3.54 MHz to 2.048 MHz.

1. Introduction

Liquid crystals (LCs) are molecules that have high nonlinearity and are sensitive to low optical fields. These materials are partially thermally stable in regular phases. Doped LCs have attracted the attention of so many researchers. Because of these characteristics LCs have been used in technological applications intensively [1, 2]. Poly (3-hexylthiophene) (P3HT) is also a well-known conductive polymer in which holes are dominant charge carriers. This polymer has a high absorption coefficient in almost all along the visible range. Because of this unique property it has been used as an organic-based solar cell [3, 4]. With the mobility of $0.1 \text{ cm}^2/\text{V}\cdot\text{s}$ (which is quite high for a polymer), P3HT has been used in organic field effect transistors as well (OFET) [5, 6].

Phthalocyanines (Pc) are also important materials for chemical applications. These thermally stable molecules have high absorption coefficient in the visible range. Pcs which are n-type materials have been used as gas sensors [7], as OFETs [8], and as solar cells [9]. Dielectric properties of Pcs have been investigated in different ways. The dielectric properties of certain Zn-Pc molecules are studied by evaporating a thin film of this material on a gold electrode [10]. Dielectric properties of Ni-Pcs are investigated by doping them in a

liquid crystal [11]. The complex expression of the dielectric constant can be written as $\epsilon^* = \epsilon' + i\epsilon''$ in terms of ϵ' and ϵ'' , which are the real and imaginary parts of dielectric constant, respectively. The frequency-dependent Cole-Cole form of this equation is [12]

$$\epsilon^* = \epsilon_\infty + \frac{(\epsilon_s - \epsilon_\infty)}{1 + (i\omega\tau)^{1-\alpha}} \quad (1)$$

Here ϵ_s is the value of the low frequency dielectric constant, and ϵ_∞ is the value of the high frequency dielectric constant in the measured frequency range, ω is the angular frequency, τ is the relaxation time, and α is the absorption coefficient.

To understand the electrical properties of the material with different structures, the dielectric spectroscopy (DS) technique is used. Mentioned real part of the dielectric constant ϵ' can also be deduced from the following equation:

$$C = \epsilon_o \epsilon' \frac{A}{d} \quad (2)$$

Here C is capacitance, ϵ_o is the dielectric constant of the free space, A is the surface area, and d is the thickness of the cell. Actually imaginary part of the dielectric constant

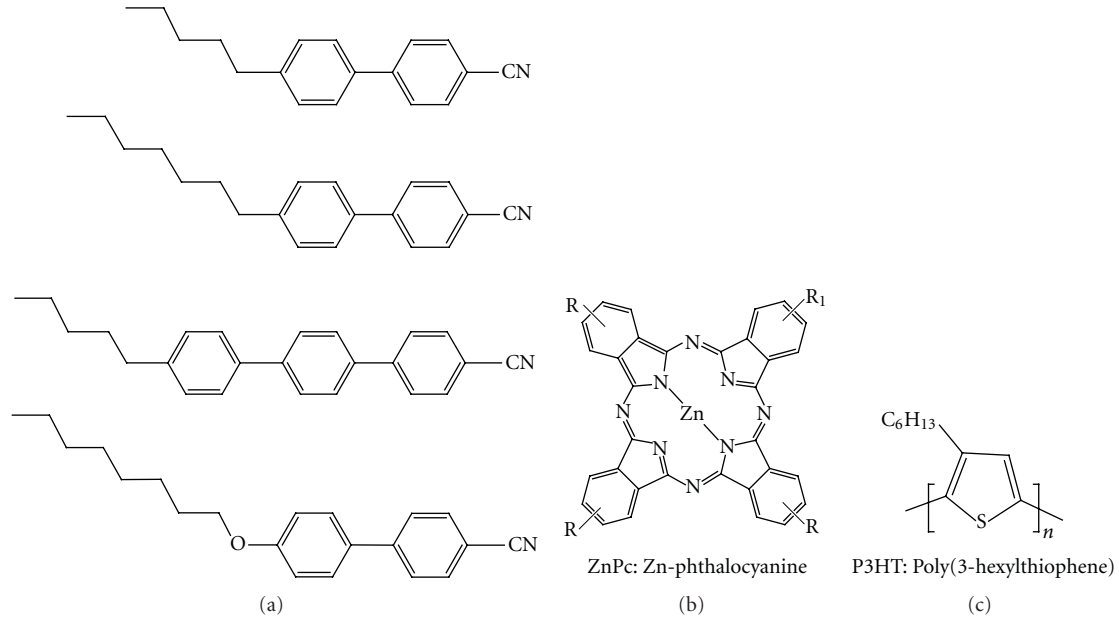


FIGURE 1: Chemical structures of: (a) nematic host, E7, (b) Zn-phthalocyanine, (c) Poly(3-hexylthiophene).

ϵ'' is known as the dielectric loss. The dielectric loss ϵ'' is calculated from the following equation:

$$\epsilon'' = \epsilon' \tan \delta, \quad (3)$$

where $\delta = 90 - \varphi$ and φ is the phase angle. In the scope of this work, relaxation times, absorption coefficient, and critical frequency are measured by DS technique. The ac conductivity and the impedance of these materials, which depend on the frequency, are studied by using the impedance spectroscopy. In fact, impedance spectroscopy is a strong tool which could be applied to overview important parameters of LCs as mentioned in [13, 14].

It is also well known that the complex impedance for the LC is expressed as

$$Z^* = Z' + Z'', \quad (4)$$

where Z' and Z'' are the real and the imaginary parts of the complex impedance, respectively, and the real part of the complex impedance is expressed as [15]

$$Z' = R_s + \frac{R_p}{1 + (\omega/\omega_0)^2}, \quad (5)$$

where R_s is the serial resistance, ω is the angular frequency of the applied field, and ω_0 is the characteristic (or natural) angular frequency of the system, $\omega_0 = 1/(R_p C_p)$. R_p is the parallel resistance, and C_p is the parallel capacitance.

2. Experimental

The measurement cells are made of two glass slides separated by Mylar sheets having a thickness of about 10 μm . Before the construction of the cells, Indium tin oxide (ITO) covered glass substrates were spin coated with Polyvinyl alcohol

(PVA) at 2000 rpm and were cured at 50°C for 2 hours. The thickness of the coating is about 100 nm. In order to obtain preliminary molecular orientation, these coating layers were exposed to surface treatment of unidirectional rubbing with velvet. This is indeed the so-called planar reorientation, where the LC molecules will be parallel to the ITO walls whatever agent is doped in small amounts. Zn-Pc (Zn-Phthalocyanine) and P3HT (poly(3-hexylthiophene)) were dissolved in LC under the reinforcement of ultrasonic effect. The structural formula of Zn-Pc, P3HT, and the nematic LC (E7) are shown in Figure 1. P3HT was purchased from Sigma-Aldrich Inc. and the Liquid Crystal was attained from Merck.

In this study four different samples were prepared: Undoped E7, a 2% w/w Zn-Pc, a 2% w/w P3HT, and a mixture of 2% w/w Zn-Pc and 2% w/w P3HT, all doped into an E7 host.

Dependency of the impedance on the frequency and the dielectric properties were investigated by making several measurements. Dielectric constant was also calculated from the parallel capacitance technique (see results and discussion). HP 4194A Impedance Analyzer was utilized for these measurements. Complex dielectric response was considered between 1 kHz to 15 MHz. RMS amplitude of this device is ~ 495 mV.

3. Results and Discussion

Figure 2 shows the real part of the complex impedance for different LC cells. As can be seen in Figure 2, at low frequencies the real part of the impedance for Pc-Zn and P3HT doped LC samples indicates a plateau region. After the plateau region, the impedance decreases drastically with the increasing frequency. At high frequencies, the impedance is

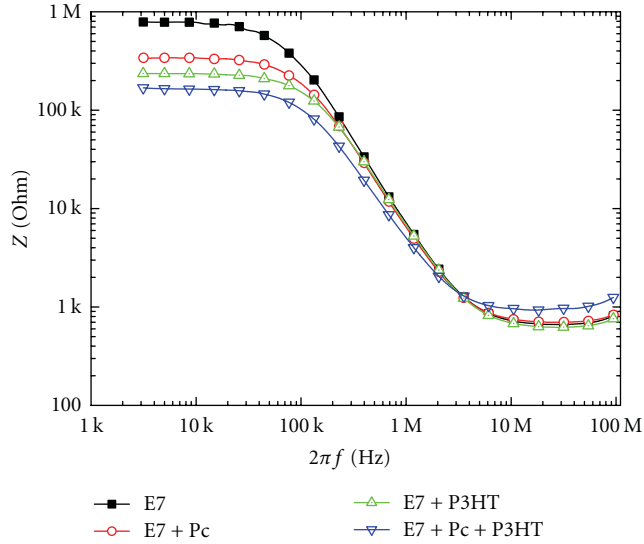


FIGURE 2: Variation of the impedance with the frequency.

stable with the increasing frequency. Compared to those of Zn-Pc and P3HT doped samples, the impedance values of Zn-Pc + P3HT doped LC samples are higher.

In the LC dielectric materials, ϵ' decreases as the frequency increases. This decrease is mainly due to the polarisability of the molecules, ionic conductivity, and interfacial orientation. Figure 3 shows this decrease of ϵ' with the frequency. The ϵ' initially decreases rapidly with the increase in the frequency, and as the frequency increases ϵ' attains a constant value.

The dielectric strength is the difference between the dielectric values at minimum and at maximum frequencies. In the impedance spectroscopy technique the dielectric strength $\Delta\epsilon$ is expressed as

$$\Delta\epsilon = \epsilon_s - \epsilon_\infty, \quad (6)$$

where ϵ_s and ϵ_∞ are the minimum and maximum components of the dielectric constant. Figure 3 shows clearly that the doping of Zn-Pc increases the dielectric strength of the sample and that the doping of P3HT increases it further. In fact, values of the dielectric strength $\Delta\epsilon$ deduced from Figure 3 are given in Table 1. With the doping, $\Delta\epsilon$ values increased from 6.75 to 10.29. This shows that when the sample is doped with the mixture of both these doping materials, then dielectric strength increased further. Overall uncertainty in dielectric measurements was 0.02 at ($k = 2$) [16].

If the dielectric medium in the measurement cell is subject to an electric field, dielectric constant is supposed to decrease as shown in (1) [12]. Also one can say that ϵ_∞ value is tending to zero at high frequencies while ϵ_s can take various values at low frequencies for different LC samples.

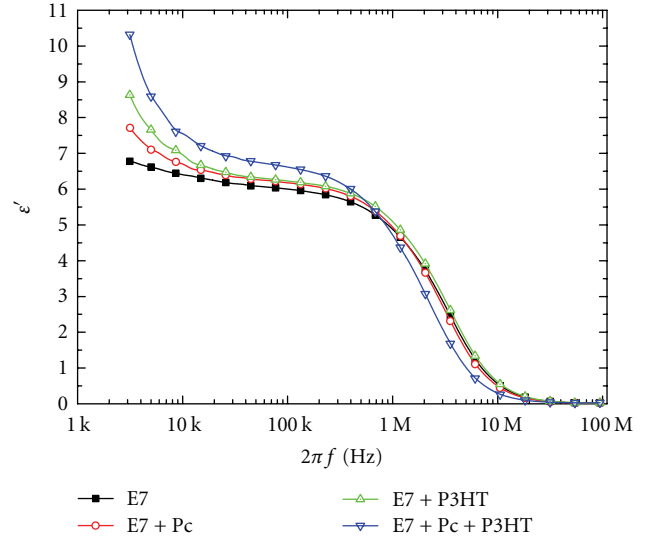


FIGURE 3: Dependency of the real dielectric constant on the frequency.

When the real part of the dielectric constant in (1) is written in the Cole-Cole equation form [12] it becomes

$$\epsilon'(\omega) = \epsilon_\infty + (\epsilon_0 - \epsilon_\infty) \frac{1 + (\omega\tau)^{1-\alpha} \sin(1/2)\alpha\pi}{1 + 2(\omega\tau)^{1-\alpha} \sin(1/2)\alpha\pi + (\omega\tau)^{2(1-\alpha)}}, \quad (7)$$

where τ is the relaxation time, and α is the absorption coefficient. The change of the dielectric constant in Figure 3 is extrapolated according to (7). Values of τ and α are calculated from this extrapolation and are shown in Table 1. While the value of the relaxation time of undoped E7 is about 5.08×10^{-7} s, in Zn-Pc doped E7, it becomes 8.29×10^{-7} s, and in P3HT doped E7 it reaches the value of 1.41×10^{-6} s. When both of these materials are doped into E7, the relaxation time increases again and reaches the value of 3.59×10^{-6} s. The absorption coefficient α is also increased with doping (See Table 1).

Imaginary dielectric constant is indeed the measure of the dissipation factor ($\tan(\delta)$). In Figure 4, it is observed that the doping increases these dissipation factors at low frequencies. A decrease in the value of the critical frequency is also observed. The critical frequencies, which correspond to the maximum imaginary part of the dielectric constant, were acquired from Figure 4 and are shown in Table 1. While the value of the critical frequency for undoped E7 is 3.54 MHz, it becomes 3.26 MHz in Zn-Pc doped E7, it decreases to 2.88 MHz in P3HT doped E7, and it decreases further to 2.04 MHz when E7 is doped with Zn-Pc + P3HT.

Dissipation factor is the rate of the real impedance over the imaginary one. When the values of the real and imaginary impedance are close, the dissipation factor becomes smaller. This change in the dissipation factor can be seen in Figure 5. Decrease in the critical frequency with doping could be observed in Figure 5 as well. At low frequencies, dissipation factor is small, but it gets higher at high frequencies with the increasing real impedance.

TABLE 1: The dielectric strength $\Delta\epsilon$, the relaxation time τ , the absorption coefficient α , and the critical frequency f_c of the samples.

Sample	$\Delta\epsilon$	τ (s)	α	f_c (Hz)
E7	6.75	5.08×10^{-7}	0.22	3.54×10^6
E7 + Zn-Pc	7.68	8.26×10^{-7}	0.37	3.2×10^6
E7 + P3HT	8.6	1.41×10^{-6}	0.51	2.88×10^6
E7 + ZnPc + P3HT	10.29	3.59×10^{-6}	0.55	2.04×10^6

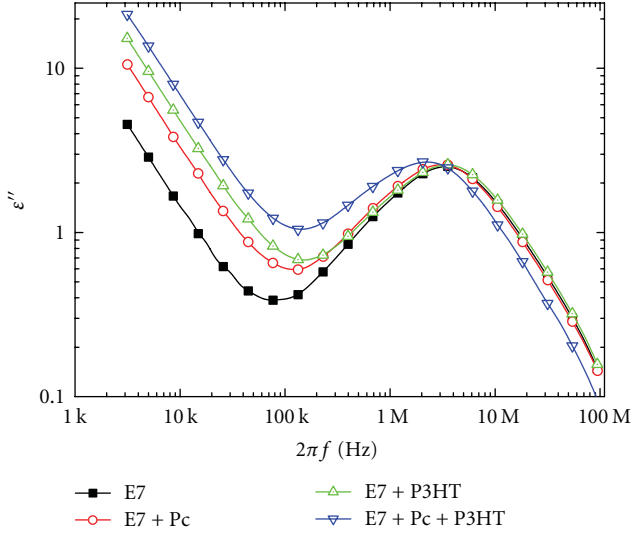


FIGURE 4: Dependency of the imaginary dielectric constant on the frequency.

TABLE 2: The dielectric constants ϵ_o , ϵ_∞ , and ϵ_{max} of the samples.

Specimens	ϵ_o	ϵ_∞	ϵ_{max}
E7	67.81	0.03	2.52
E7 + Pc	77.09	0.03	2.62
E7 + P3HT	86.33	0.03	2.62
E7 + Pc + P3HT	10.32	0.03	2.72

When the value of absorption coefficient (α) is zero, the material shows Debye type relaxation, if the values of α gets bigger than zero, and less than one, the material shows non-Debye type relaxation [12]. Existence of Debye type relaxation can be determined from the Cole-Cole plots. As shown in Figure 6, the centers of the arcs are located below the x -axis for all samples, indicating that non-Debye type relaxation is dominant when there is no bias field applied [15, 16]. From the analysis of the Cole-Cole plots that are shown in Figure 6, one can get information about the dielectric constants at minimum and maximum frequencies.

The value of the dielectric constant at the maximum point of the semicircles ϵ_{max} can also be obtained from these plots for the different doping materials. All the dielectric constants deduced from Cole-Cole plots are shown in Table 2.

Cole-Cole plots can give information about the equivalent circuit structures. Our LC cells show properties of a parallel RC equivalent circuit in series to a resistance.

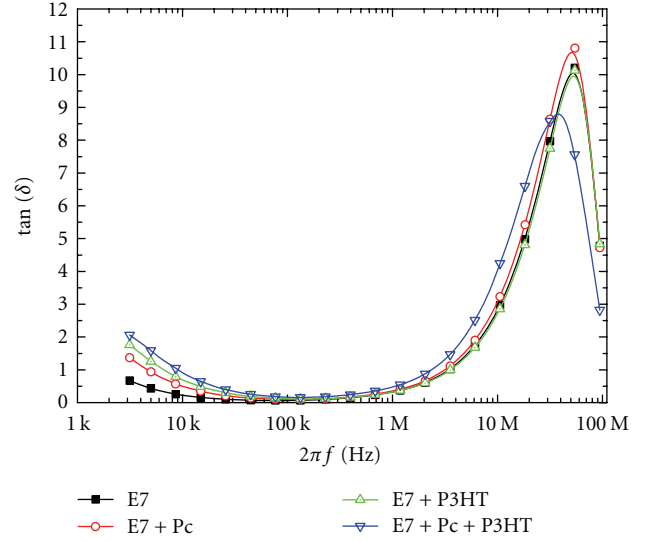


FIGURE 5: Variation of the dissipation factor with the frequency.

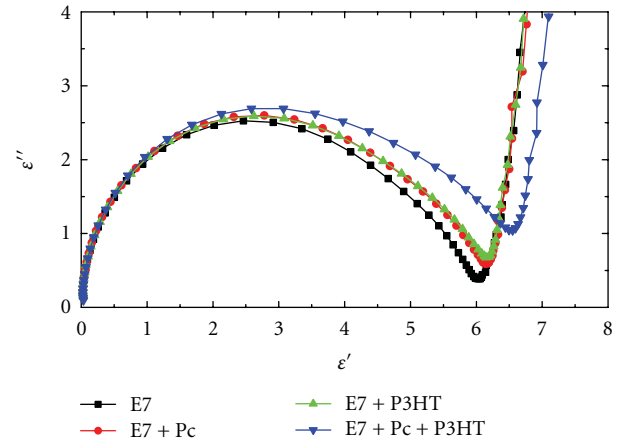


FIGURE 6: Cole-Cole plots of the pure and the doped samples.

Critical frequency decreases exponentially with the absorption coefficient α with the addition of different doping materials (Figure 7(a)), and the relaxation time increases exponentially with the increase of the absorption coefficient α (Figure 7(b)).

4. Conclusions

In this study, the doping of Zn-Pc and P3HT into E7 decreased the impedance. From this study we concluded that P3HT is a better conductor than Zn-Pc, and when the sample is doped with both of these materials in the same proportion, then the impedance is decreased further. A study of the critical frequency, relaxation time, and absorption coefficients using DS is also carried out. As a result, we have noticed that the doping decreased the critical frequency and increased the conductivity. It also increased the relaxation time. Increase in the values of absorption coefficient by doping implies the non-Debye type relaxation behaviors in

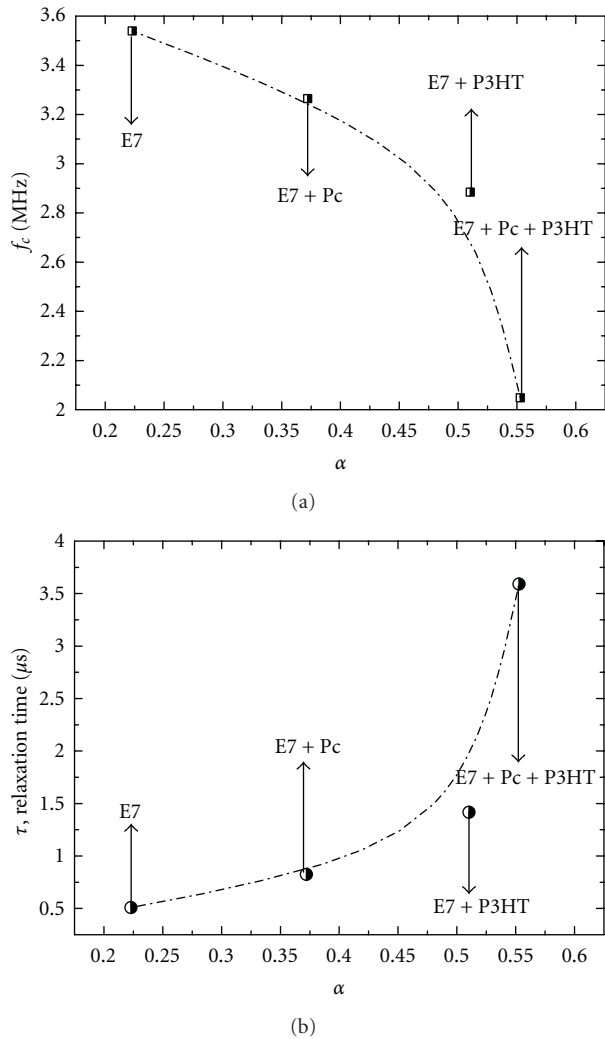


FIGURE 7: (a) Variation of the critical frequency with α . (b) Variation of the relaxation time with α .

the proposed LC sample, which is a novel configuration caused by the doping of P3HT and Zn-Pc.

Acknowledgment

Special thanks are due to Dr. Burak Esat from Fatih University for providing the authors with Zn-phthalocyanine.

References

- [1] F. Simoni and O. Francescangeli, "Effects of light on molecular orientation of liquid crystals," *Journal of Physics Condensed Matter*, vol. 11, no. 41, p. R439, 1999.
- [2] Y. J. Wang and G. O. Carlisle, "Optical properties of dispersed-1-doped nematic liquid crystal," *Journal of Materials Science: Materials in Electronics*, vol. 13, no. 3, pp. 173–178, 2002.
- [3] Y. Y. Kim, S. Cook, S. M. Tuladhar et al., "A strong regio-regularity effect in self-organizing conjugated polymer films

and high-efficiency polythiophene: fullerene solar cells," *Nature Materials*, vol. 5, no. 3, pp. 197–203, 2006.

- [4] M. C. Scharber, D. Mühlbacher, M. Koppe et al., "Design rules for donors in bulk-heterojunction solar cells—towards 10% energy-conversion efficiency," *Advanced Materials*, vol. 18, no. 6, pp. 789–794, 2006.
- [5] D. H. Kim, Y. D. Park, Y. S. Jang et al., "Enhancement of field-effect mobility due to surface-mediated molecular ordering in regioregular polythiophene thin film transistors," *Advanced Functional Materials*, vol. 15, no. 1, pp. 77–82, 2005.
- [6] Z. Bao, A. Dodabalapur, and A. J. Lovinger, "Soluble and processable regioregular poly (3-hexylthiophene) for thin film field-effect transistor applications with high mobility," *Applied Physics Letters*, vol. 69, no. 26, pp. 4108–4110, 1996.
- [7] R. Zhou, F. Josse, W. Göpel, Z. Z. Öztürk, and Ö. Bekaroglu, "Phthalocyanines as sensitive materials for chemical sensors," *Applied Organometallic Chemistry*, vol. 10, no. 8, pp. 557–577, 1996.
- [8] T. B. Singh, R. Koeppe, N. S. Sariciftci, M. Morana, and C. J. Brabec, "Monitoring the channel formation in organic field-effect transistors via photoinduced charge transfer," *Advanced Functional Materials*, vol. 19, no. 5, pp. 789–795, 2009.
- [9] C. J. Brabec, N. S. Sariciftci, and J. C. Hummelen, "Plastic solar cells," *Advanced Functional Materials*, vol. 11, no. 1, pp. 15–26, 2001.
- [10] H. M. Zeyada and M. M. El-Nahass, "Electrical properties and dielectric relaxation of thermally evaporated zinc phthalocyanine thin films," *Applied Surface Science*, vol. 254, no. 6, pp. 1852–1858, 2008.
- [11] O. Köysal, M. Okutan, M. Durmuş, F. Yakuphanoglu, S. E. San, and V. Ahsen, "Diffraction efficiency and dielectric relaxation properties of nickel phthalocyanine doped nematic liquid crystal," *Synthetic Metals*, vol. 156, no. 1, pp. 58–64, 2006.
- [12] G. G. Raju, *Dielectrics in Electric Fields*, Marcel Dekker, New York, NY, USA, 2003.
- [13] S. E. San, M. Okutan, O. Köysal, and Y. Yerli, "Carbon nanoparticles in nematic liquid crystals," *Chinese Physics Letters*, vol. 25, no. 1, pp. 212–215, 2008.
- [14] M. Okutan, F. Yakuphanoglu, S. E. San, and O. Köysal, "Impedance spectroscopy and dielectric anisotropy-type analysis in dye-doped nematic liquid crystals having different preliminary orientations," *Physica B*, vol. 368, no. 1–4, pp. 308–317, 2005.
- [15] A. Popova, S. Raicheva, E. Sokolova, and M. Christov, "Frequency dispersion of the interfacial impedance at mild steel corrosion in acid media in the presence of benzimidazole derivatives," *Langmuir*, vol. 12, no. 8, pp. 2083–2089, 1996.
- [16] ISO, *Guide to the Expression of Uncertainty of Measurement*, 1st edition, 1993.